DISSERTATION

PHASE CODING AND FREQUENCY DIVERSITY FOR WEATHER RADARS

Submitted by

Mohit Kumar

Department of Electrical and Computer Engineering

In partial fulfillment of the requirements

For the Degree of Doctor of Philosophy

Colorado State University

Fort Collins, Colorado

Fall 2020

Doctoral Committee:

Advisor: V Chandrasekar

Anura Jayasumana
Margaret Cheney
Susan James

Copyright by Mohit Kumar 2020

All Rights Reserved

ABSTRACT

PHASE CODING AND FREQUENCY DIVERSITY FOR WEATHER RADARS

This thesis has developed three main ideas: 1) Polyphase coding to achieve orthogonality between successive pulses leading to second trip suppression abilities, 2) Frequency diversity on a pulse to pulse basis to achieve second trip suppression and retrieval capability in a weather radar, 3) a multiple input, multiple output (MIMO) configuration using the orthogonality features obtained using ideas in 1 and 2. It is shown in this thesis that this configuration for a radar leads to better spatial resolution by the formation of a bigger virtual array. It is also demonstrated that orthogonality is a big requirement to get this improvement from a MIMO configuration. This thesis addresses this issue with a new polyphase code pair and mismatched filter based framework which gives excellent orthogonal features compared to a matched filter processor. The MIMO platform is a long term goal (technologically) and therefore the polyphase codes were used to demonstrate second trip suppression abilities that uses orthogonal features of these codes to reduce range and velocity ambiguity. These are called as Intra-pulse phase coding techniques. The thesis also demonstrates another technique to achieve orthogonality between pulses by coding them on different frequencies. This is termed as Inter-pulse frequency diversity coding. In the beginning, design and implementation of Intra-pulse polyphase codes and algorithms to generate these codes with good correlation properties are discussed. Next, frequency diversity technique is introduced and compared with other inter-pulse techniques. Other Inter-pulse coding schemes like that based on Chu codes are widely used for second trip suppression or cross-polarization isolation. But here, a novel technique is discussed taking advantage of frequency diverse waveforms. The simulations and tests are accomplished on D3R weather radar system. A new method is described to recover velocity and spectral width due to incoherence in samples from change of frequency pulse to pulse. It is shown that this technique can recover the weather radar moments over a much higher dynamic

range of the other trip contamination as compared with the popular systematic phase codes, for second trip suppression and retrieval.

For these new features to be incorporated in the D3R radar, it went through upgrade of the IF sections and digital receivers. The NASA dual-frequency, dual-polarization, Doppler radar (D3R) is an important ground validation tool for the global precipitation measurement (GPM) mission's dual-frequency precipitation radar (DPR). It has undergone extensive field trials starting in 2011 and continues to provide observations that enhance our scientific knowledge. This upgrade would enable more research frontiers to be explored with enhanced performance. In the thesis, this upgrade work is also discussed.

ACKNOWLEDGEMENTS

I would like to thank my family for their patience throughout this work. I am grateful and thankful to my advisor, Prof V. Chandrasekar for his support and guidance throughout this period.

This research was funded by the NASA GPM program. The author acknowledges the support of the NASA GPM - GV team for this research.

DEDICATION

I would like to dedicate this work to my wife Shuchi, daughter Manya, Mom and Dad.

TABLE OF CONTENTS

LIST OF TABLES

LIST OF FIGURES

Chapter 1

Introduction

The techniques that are developed in this thesis are validated and test results are available for NASA D3R radar system. The NASA dual frequency, dual polarization doppler radar (D3R) was developed as a joint collaboration between NASA and Colorado State University. It allows for beam aligned, synchronized operation between Ku band (13.91GHz) and Ka band (13.51GHz) for observation of weather. Both the bands are capable of simultaneous operation with separate channels of transmit and receive for the horizontal and vertical polarization. It is an integral part of the ground validation tools for dual precipitation radar, with analogous bands, for the core satellite in the GPM mission. The Ku band samples volume upto 40 km of range with peak power of 200 Watts from solid-state transmitter [1], and Ka band has peak power of 40 Watts, providing enhanced sensitivity to light rain and snow. The combination of ku and ka band information is vital for dual-frequency measurements, which results in better characterization of snow type. It is very useful to find out different aggregates of snow particles and the presence of graupel. The dual-polarization and dual-frequency measurements are also highly effective in narrowing down the characterization of falling snow [2]. In addition to this, dual-polarimetric variables such as differential reflectivity, differential phase, co-polar correlation also helps in classifying precipitation type like rain, dry snow, wet snow, prestine ice crystals, mixed phase etc [3].

D3R also uses a multi-pulse scheme to mitigate the effects of blind range caused by longer pulses and subsequently using pulse compression to enhance the range resolution and sensitivity.

The use of solid-state transmitters together with receive systems with pulse compression waveforms enables a flexible architecture. And with the recent upgrade of the digital receive and IF electronics, the radar is much more programmable and adaptive sensing can also be incorporated. However, a major source of error for volume target or weather sensing for these pulse compression systems, is usually through the range side-lobes. Mismatched filtering techniques have been proposed earlier to reduce peak side-lobe levels to a certain extent [4]. Hence, large length mismatched filters have been incorporated in new design using high end FPGAs.

D3R has undergone extensive field trials that include Midlatitude Continental Convective Cloud Experiment (MC3E), a field program involving NASA Global Precipitation Measurement Program and ARM investigators, in south-central Oklahoma during the April to May 2011 period. Additionally, the GPM Cold-season Precipitation Experiment (GCPEx) was conducted in cooperation with Environment Canada in Ontario, Canada from January 17th to February 29th, 2012. The goal of GCPEx was to improve the DPR snow retrieval algorithms. Later on, radar underwent IFloodS Experiment along with X-band radars and NEXRAD S-band radars in the area of Cedar river and Iowa river basins, to model the hydrological response of the Iowa region. In a latest research expedition, D3R had its first international deployment in South Korea during the Winter Olympics and Paralympic Games in 2018. It was known as the ICE-POP campaign. For the ICE-POP 2018 campaign, D3R was installed on the rooftop of Daegwallyeong Regional Weather Office (DGW) in the Daegwallyeong-myeon province of South Korea. Figure 1.1 shows the D3R during one of the winter Olympic days. Along with D3R there were a variety of instrumentation at the ICE-POP 2018 ranging from Parsivel disdrometers, wind profilers, Doppler lidar and X-band radars.

The goal of ICE-POP 2018 was to understand the winter precipitation regime with complex terrain, and the associated processes, with the focus of improving the short term forecasting and nowcasting systems. The experiment was supported by Korea Meteorological Administration (KMA) and National Institute of Meteorological Science (NIMS). The D3R, with its simultaneous operation in Ku and Ka band, helped in understanding winter precipitation by focusing on the microphysical aspects of measurement, which is useful in forecasting of orographic snow during the winter Olympics. Also, since the coastline of the ocean was very near, these observations also aided in understanding interactions between ocean and mountain regions and formation of the clouds and snow [8].

The hardware upgrade of the D3R radar system was accomplished before the ICE-POP campaign. And the software based enhancements were done after it. With the upgrade hardware,

Figure 1.1: The NASA D3R deployed at rooftop of Daegwallyeong Regional Weather Office (DGW) in the Daegwallyeong-myeon province of South Korea.

the resolution can be enhanced upto 30m from the current resolution of 150m. With five times more number of independent samples available, the overall sensitivity of the system will improve. Additionally, it has totally coupled waveform generator , digital down-converter and pulse compressor design. Due to which, it can accomplish pulse by pulse change of waveform and filters, synchronously. With these capabilities in mind, new orthogonal waveform set is developed, which will aid in mitigation and retrieval of second trip echoes. Another technique is developed, using frequency change from pulse to pulse, which gives a much higher dynamic range of retrieval of second trips, than other inter-pulse techniques. This was also tested on D3R.

These techniques were developed and tested on D3R as the weather radar platform to fulfill a bigger goal to test orthogonality improvement due to these with second trip suppression as the short term goal but keeping in mind the MIMO configuration for weather radars as the long term goal. The MIMO performance is mainly dictated by the orthogonal nature of the transmitted waveform. Here we are trying to demonstrate this with polyphase code and frequency diversity schemes. To test these schemes on D3R which cannot be operated in MIMO sense because of reflector antenna, we have used second trip suppression as the benchmark application to judge the performance that can be achieved with these new developed schemes. A MIMO configuration has been proposed for weather radars and its ability to improve spatial resolution due to formation of a bigger virtual array than the physical array is shown through simulation. But the assumption is of orthogonal nature of transmission through the quadrants of the physical array.

The thesis has been organized as follows. First of all, we present the salient highlights of the hardware modifications carried out for the upgrade and then next we focus on the design and development of the polyphase coded waveforms, suitable for D3R platform architecture. The next chapter has details about a frequency diversity scheme. Followed by MIMO configuration for weather radars with simulations and theory detailing each aspect of this configuration. Finally summarizing and concluding the whole thesis in the last chapter.

Chapter 2

Fundamentals of Dual-polarized Weather Radar System

A dual-polarized radar transmits horizontal and vertically polarized signals and receive back an echo, which is an amplitude scaled and doppler-shifted version of transmitted wave. Thus a received signal can be written as:

$$V_r(t) = A_r exp(j2\pi f_0(t - \tau)) \tag{2.1}$$

where A_r is the received amplitude, f_0 is the transmitted frequency, the doppler is a small shift in the transmitted frequency, τ is round trip delay from radar to the scatterer and back. Half of this delay, is proportional to the range of scatterer. However, for meteorological targets, which have a wide spread, in temporal and angular dimensions, the echo received, is the sum of backscatter from individual hydrometeors, as shown in figure 2.1. The resultant phasor has an in-phase (I) and a quadrature (Q) components, which makes up the complex voltage, $V_r(t) = I(t) + jQ(t)$. All the scatterers between leading and trailing edge of the transmit pulse, returns a single voltage sample, as shown in figure 2.2 [5].

If the radar transmits a periodic pulse train with PRT T_s, the received voltage at the same range-time (τ) is given as $V_r(t = \tau), V_r(t = \tau + T_s), ..., V_r(t = \tau + mT_s)$, which form a sequence of temporal samples from the same resolution volume, depicted in figure 2.3. Hence it is easy to observe that at a given time-range τ, the sample voltages $V_r(t = \tau + mT_s) = V_r(\tau, t_s = mT_s)$, are the sampled version of the sample-time axis, t_s. Therefore, we can define $V_r(\tau, t_s)$, to be received voltage along t_s, defined by the time-varying properties of particles located at the resolution volume for a fixed τ.

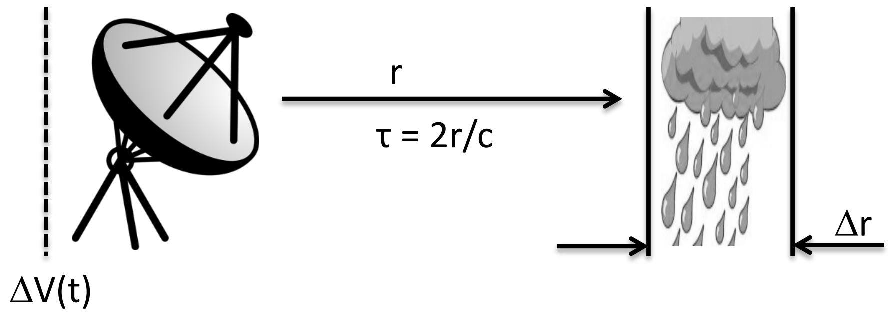

Figure 2.1: The voltage $\varDelta V(t)$ induced at antenna port due to the resolution volume extending in space from r to $r + \varDelta r$.

2.1 Estimation of Covariance Matrix

Let $\mathbf{Z}(n)$ be the vector given by $(V_{hh}[n], V_{vh}[n], V_{hv}[n], V_{vv}[n])^T$ where V_{hh} corresponds to co-polar return (H-pol transmit and sensing receive power on H-pol), V_{hv} corresponds to cross-polar return (V-pol transmit and sensing receive power on H-pol), V_{vh} corresponds to cross-polar return (H-pol transmit and sensing receive power on V-pol) and finally, V_{vv} corresponds to co-polar return (V-pol transmit and sensing receive power on V-pol). $n = 1, 2, 3, ..., N$, are the N time samples of the signal. Then, the covariance of $\mathbf{Z}$ can be written as [5]:

$$E[\mathbf{Z}\mathbf{Z}^{*T}] = E \begin{bmatrix} |V_{hh}|^2 & V_{hh}(V_{vh}^*) & V_{hh}(V_{hv}^*) & V_{hh}(V_{vv}^*) \\ V_{vh}(V_{hh}^*) & |V_{vh}|^2 & V_{vh}(V_{hv}^*) & V_{vh}(V_{vv}^*) \\ V_{hv}(V_{hh}^*) & V_{hv}(V_{vh}^*) & |V_{hv}|^2 & V_{hv}(V_{vv}^*) \\ V_{vv}(V_{hh}^*) & V_{vv}(V_{vh}^*) & V_{vv}(V_{hv}^*) & |V_{vv}|^2 \end{bmatrix} \tag{2.2}$$

As we know that the received signal at a fixed time delay τ corresponds to resolution volume at $c\tau/2$, thus the elements of this covariance matrix are related to the elements of the covariance matrix in that resolution volume. The conjugate symmetry property yields ten independent elements of this matrix. Also, through reciprocity, it can be easily observed that the cross-polar returns V_{vh} and V_{hv} are identical. Finally, only six quantities are essential to estimate covariance matrix. This

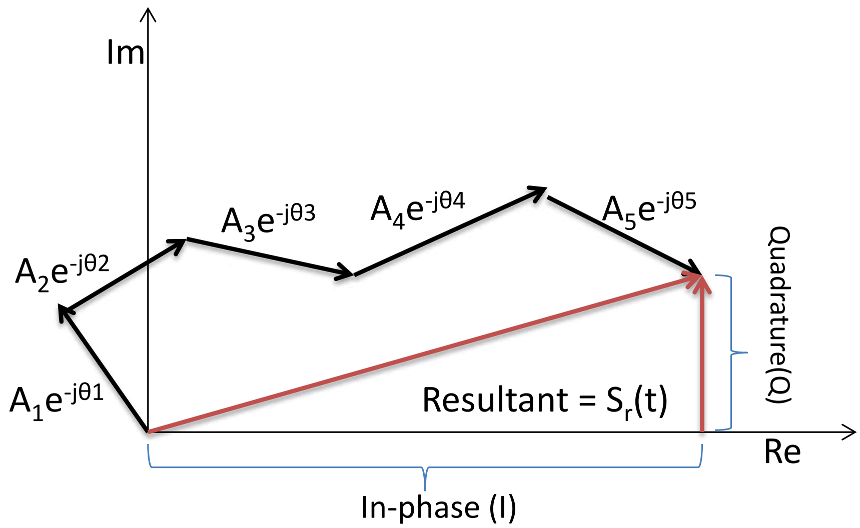

Figure 2.2: Complex plane plot of "instantaneous" sum of phasors of individual scatterers to form $V_r(t)$. The phase angle θ_k is uniformly distributed between $(-\pi, \pi)$.

covariance matrix measurement is equivalent to covariance matrix of scatterers in precipitation medium defined by:

$$\Sigma = \left\langle \begin{bmatrix} |S_{hh}|^2 & \sqrt{2}S_{hh}(S_{hv}^*) & S_{hh}(S_{vv}^*) \\ \sqrt{2}S_{hv}(S_{hh}^*) & 2|S_{hv}|^2 & \sqrt{2}S_{hv}(S_{vv}^*) \\ S_{vv}(S_{hh}^*) & \sqrt{2}S_{vv}(S_{hv}^*) & |S_{hh}|^2 \end{bmatrix} \right\rangle \tag{2.3}$$

where S_{hh}, S_{hv}, S_{vh} and S_{vv} are the elements of the scattering matrix and the angle brackets denote the ensemble averaging. The elements of back-scattering covariance matrix or some combination of them are used to compute the polarimetric moments.

If $\mathbf{K}(l)$ is the auto-correlation matrix of signal vector $\mathbf{Z}(n)$, then,

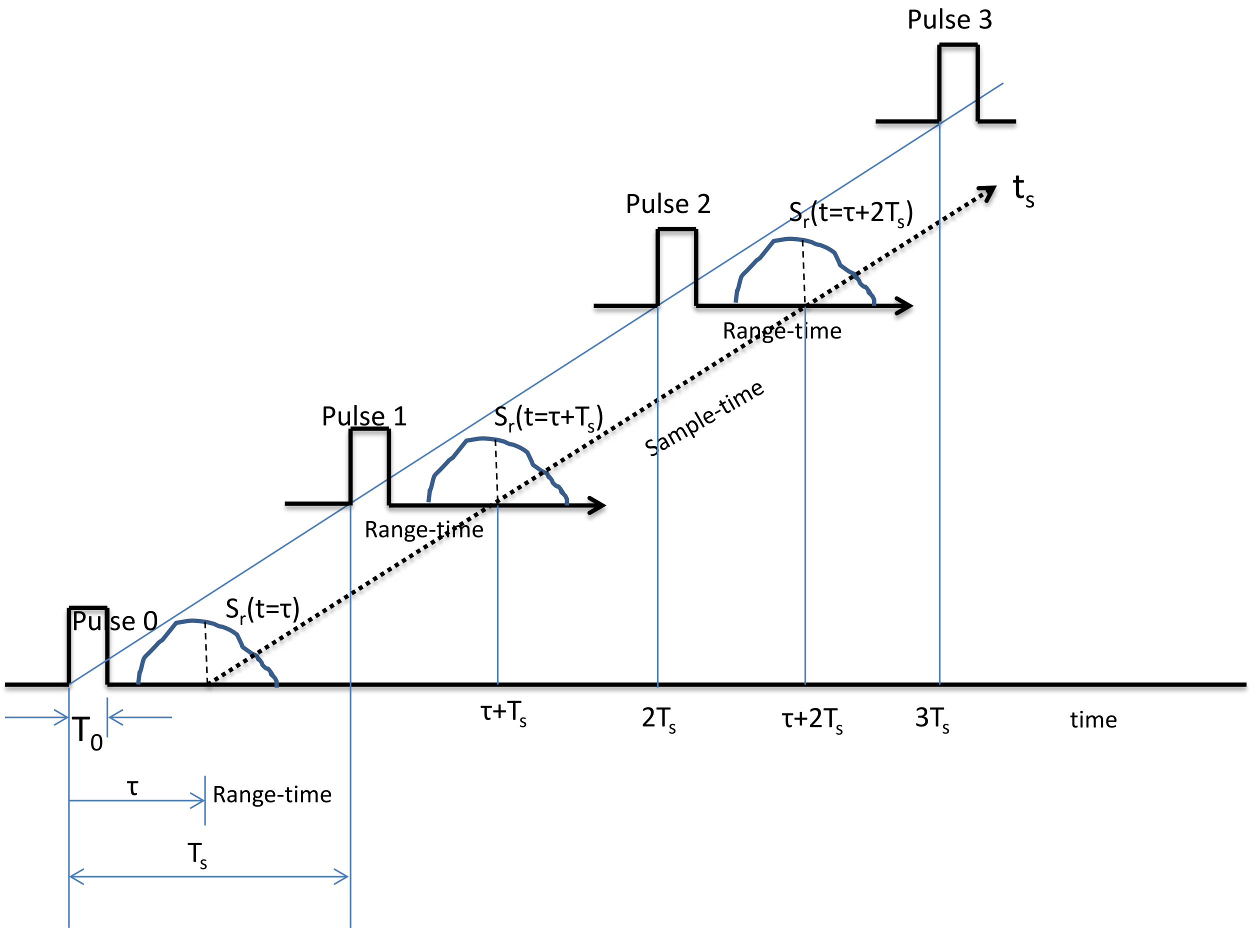

Figure 2.3: This plot is depicting the range-time axis and sample time axis, t_s, across multiple pulses with pulse repetition time as T_s [5].

$$\mathbf{K}(l) = E[\mathbf{Z}(n+l)(\mathbf{Z}^*(n)^T)]$$

$$= E[\begin{bmatrix} V_{hh}(n+l) \\ V_{vh}(n+l) \\ V_{hv}(n+l) \\ V_{vv}(n+l) \end{bmatrix} \begin{bmatrix} V_{hh}^*(n) & V_{vh}^*(n) & V_{hv}^*(n) & V_{vv}^*(n) \end{bmatrix}] \tag{2.4}$$

This matrix **K** has six independent terms and those can be written down as:

$$\begin{aligned} E[V_{hh}(n+l)V_{hh}^*(n)] &= R_{hh,hh}(l) \\ E[V_{hh}(n+l)V_{vh}^*(n)] &= R_{hh,vh}(l) \\ E[V_{hh}(n+l)V_{vv}^*(n)] &= R_{hh,vv}(l) \\ E[V_{vh}(n+l)V_{vh}^*(n)] &= R_{vh,vh}(l) \\ E[V_{vv}(n+l)V_{hv}^*(n)] &= R_{vv,hv}(l) \\ E[V_{vv}(n+l)V_{vv}^*(n)] &= R_{vv,vv}(l) \end{aligned} \tag{2.5}$$

The correlation coefficients for these are given by $\rho_{hh,hh}(l)$, $\rho_{hh,vh}(l)$, $\rho_{hh,vv}(l)$, $\rho_{vh,vh}(l)$, $\rho_{vv,hv}(l)$ and $\rho_{vv,vv}(l)$. Now let's talk about few of the pulsing schemes used in dual-polarization weather radars [5]:

1. Alternating Polarization Mode: Either horizontal or vertical polarization is transmitted, in alternate pulses.

2. Block Pulsing Mode: A block of pulses with fixed transmit pattern, is used.

3. Hybrid Mode: Simultaneous transmit of horizontal or vertical polarization, with simultaneous receive as well.

The Alternating polarization mode has simultaneous reception of H- and V-pol echoes. All these modes of operation can be illustrated with figure 2.4. We would come back to estimation of dual-polarization variables, under these pulsing scenarios later, after covering basic definitions of these variables.

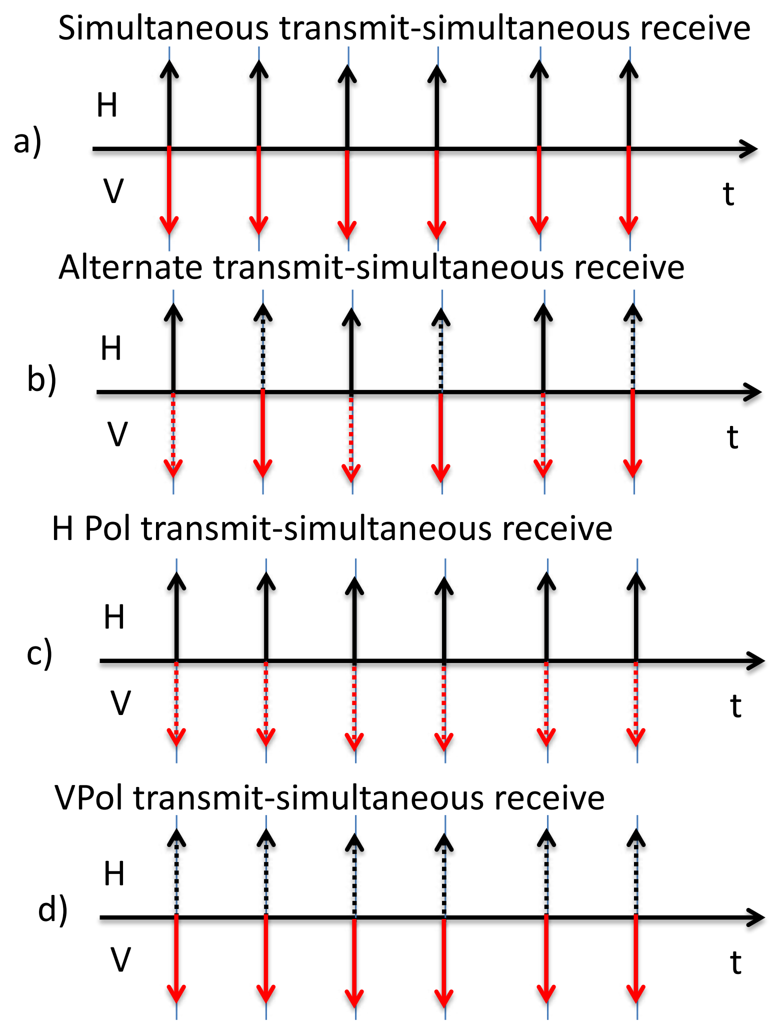

Figure 2.4: The pulsing schemes are demonstrated. a) depicts the hybrid mode, co-polar and cross-pol power coexist, however, co-pol power is significantly larger than cross-pol. Here, cross-pol cannot be estimated, b) is the alternating polarization mode, with simultaneous receive on H and V-Pol, co-polar and cross-pol returns can be measured, to give an estimate of covariance matrix in two pulses, c) and d) are either H-pol or V-pol transmit only, with simultaneous receive.

2.2 Single-polarization Moments

2.2.1 Reflectivity factor

The weather radar range equation, which includes the finite bandwidth loss factor (l_r) and receiver power gain (G_r), for a scatterer at range r is given by [5]:

$$P(r) = (cT_0/2)(G_r/l_r)[\lambda^2 P_t G_0^2/4\pi^3][\pi\theta\phi/8ln2]\eta/r^2 \tag{2.6}$$

where, T_0 is the pulse width, P_t is the power transmitted, θ, ϕ are the azimuth and elevation beamwidth, respectively. The power $P(r)$ is referenced to the receiver output. η is called the radar reflectivity (in m^2m^{-3}), or the back scatter cross-section per unit volume.

We can define a volume around (r, θ, ϕ) such that the scatterers in this volume dominate the contribution towards $P(r)$, which is known as resolution volume in space. The received mean power on H-pol or V-pol, can also be estimated through the digital samples from corresponding channels as:

$$\hat{P_{h/v}} = \frac{1}{N}\Sigma_{k=0}^{N-1} V_{hh/vv}(k)V_{hh/vv}^*(k) \tag{2.7}$$

$$\hat{P_h}^{co} = G_r + 10log(\hat{P_{h/v}}) \tag{2.8}$$

where G_r is the gain referenced till digital receiver.

2.2.2 Mean Doppler velocity

Here we would focus on the pulse-pair estimation of mean doppler velocity. If $V_{hh/vv}(n)$, where $n = 1, 2, ..., N$, are the time samples of the received echo separated by PRT T_s, then the auto-correlation at lag 1 is estimated as,

$$\hat{R}[1] = \frac{1}{N}\Sigma_{k=0}^{N-2} V_{hh/vv}[k+1]V_{hh/vv}^*[k] \tag{2.9}$$

The mean velocity can be computed from this by:

$$\hat{v} = -\frac{\lambda}{4\pi T_s} arg(\hat{R}[1]) \tag{2.10}$$

The variance of $\hat{v}$ is dependent upon the variance of phase of $\hat{R}[1]$. Using perturbation analysis, the variance of $\hat{v}$, can be written as [7]:

$$var(\hat{v}) = \frac{\lambda^2}{32\pi^2 T_s^2 |\rho[1]|^2} (\frac{1 - |\rho[1]|^2}{N^2}) \Sigma_{n=-(N-1)}^{N-1} |\rho[n]|^2 (N - |n|) \tag{2.11}$$

where N is the number of samples, T_s is the PRT and $|\rho[n]|$ is the magnitude of correlation coefficient function.

2.2.3 Spectral Width

The power spectral density of meteorological signals can be approximated by a Gaussian shape, with mean velocity v and standard deviation σ_v. The σ_v is often refereed to as spectral width. This can be estimated using the magnitude of auto-correlation at zero lag and lag one as:

$$\hat{\sigma_v} = \frac{\lambda}{2\pi T_s \sqrt{2}} [ln|\frac{\hat{R}[0]}{\hat{R}[1]}|]^{1/2} \tag{2.12}$$

Since only the magnitude of the auto-correlation is involved, thus σ_v can also be estimated from incoherent or non-doppler radars.

2.3 Polarimetric Moments

The back-scatter from hydrometeors depend upon the size and orientation of the particle with respect to the polarization state. Polarimetric moments, hence, provide additional information for better quantitative measurement of precipitation.

2.3.1 Differential Reflectivity

It is defined as:

$$Z_{dr} = 10log(\frac{\langle|S_{hh}|^2\rangle}{\langle|S_{vv}|^2\rangle}) \tag{2.13}$$

and can be used as a mean particle shape measure.

2.3.2 Co-polar Correlation

The lag zero correlation between the co-polar signals is given by:

$$\hat{R}_{vvhh} = \frac{1}{N}\Sigma_{k=0}^{N-1}V_{vv}[k]V_{hh}^{*}[k] \tag{2.14}$$

The magnitude and phase terms are given by:

$$|\rho_{hv}(0)| = \frac{|\hat{R}_{vvhh}|}{\sqrt{P_h}\sqrt{P_v}} \tag{2.15}$$

$$arg[\hat{R}_{vvhh}^{*}] = \psi_{dp} = \phi_{dp} + \delta \tag{2.16}$$

where ϕ_{dp} is the differential propagation phase shift and δ is the differential phase shift upon scattering. Under Rayleigh approximation, $\delta \sim 0$.

2.3.3 Linear Depolarization Ratio, LDR_{vh}

It can be defined as:

$$|LDR_{vh}(0)| = 10log_{10}\frac{|\hat{S}_{vh}|^2}{|\hat{S}_{hh}|^2} \tag{2.17}$$

The moments Z_{dr} and LDR_{vh} are the functions of incidence angle, orientation angle, relative permittivity and eccentricity of the spheroid (rain drops).

Now let us see how these moments are estimated based on the mode of operation.

2.4 Estimation of covariance matrix under alternating mode of operation

Here, the sequence of transmit is H, V, H, V .... and simultaneous reception. The total number of received signal samples would be 2N for both polarization states. This mode is depicted in figure 2.4-(b). This mode of operation, allows for the cross-polar return power measurement. The

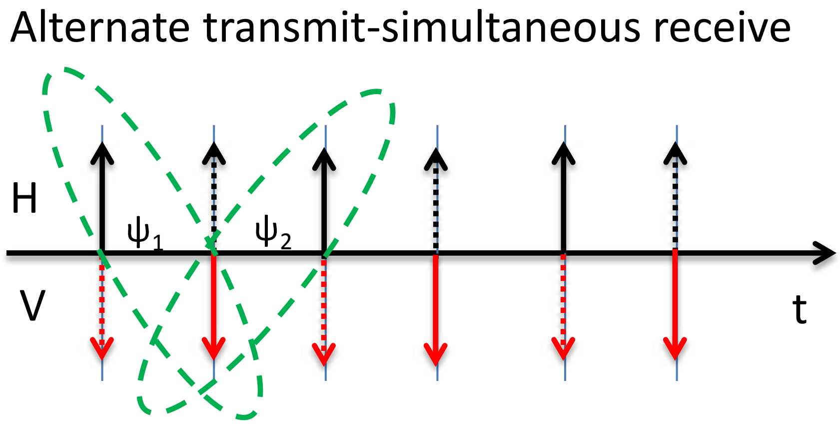

Figure 2.5: The formation of ψ_1 and ψ_2.

magnitude of the return signal on two polarizations, are related by factor Z_{dr} and mean phase between them, is the differential propagation phase ϕ_{dp}. The co-polar return signals for the H- and V-polarization can be written as [5]:

$$P_{co}^{h} = \frac{2}{N}\Sigma_{n=1}^{N/2}|V_{hh}[2n]|^2 \tag{2.18}$$

$$P_{co}^{v} = \frac{2}{N}\Sigma_{n=1}^{N/2}|V_{vv}[2n-1]|^2 \tag{2.19}$$

and the differential reflectivity becomes,

$$Z_{dr} = 10log_{10}(\frac{P_{co}^{h}}{P_{co}^{v}}) \tag{2.20}$$

Since the cross-polar signals are usually very weak (20-30 dB below co-polar), these cannot be used to compute velocity estimate or differential phase. Thus, we define two variables, ψ_1 and ψ_2, as shown in figure 2.5 [5].

$$\psi_1 = arg[\frac{2}{N}\Sigma_{n=1}^{N/2-1}V_{hh}[2n]V_{vv}^{*}[2n-1]] \tag{2.21}$$

$$\psi_2 = arg[\frac{2}{N}\Sigma_{n=1}^{N/2-1}V_{vv}[2n+1]V_{hh}^{*}[2n]] \tag{2.22}$$

For symmetric Doppler spectra, the mean velocity can be estimated from $\hat{R}[1]$. And the estimate of mean velocity in alternating mode is given by:

$$\hat{v} = -\frac{\lambda}{4\pi T_s}\frac{1}{2}(\psi_2 + \psi_1) \tag{2.23}$$

and,

$$\psi_{dp} = \frac{1}{2}(\psi_2 - \psi_1) \tag{2.24}$$

Since estimation of ψ_{dp} involves one half of algebraic sum of two phase estimates, they are unique in the interval of π. However, some constraints can be imposed on estimates of ψ_{dp} to resolve this ambiguity. Finally, let's look at the cross-polar power return:

$$P_{cx} = \frac{2}{N}\Sigma_{n=1}^{N/2}|V_{vh}[2n-1]|^2 \tag{2.25}$$

and the LDR can be written as:

$$LDR_{vh} = 10log_{10}(\frac{P_{cx}^h}{P_{co}^h}) \tag{2.26}$$

2.5 Few Example Radar Systems

2.5.1 CSU-CHILL S-band Radar

It is a research S-band radar, designed to provide high quality radar data as dual-polarized moment data as well as digitized radar signals. More or less, all the aspects of radar are under software control. Radar can be fully operated and monitored remotely. Data exchange between sub-systems happen over TCP/IP network. Additional processing power to implement advance algorithms, can be readily added to the system by adding more compute servers into the network.

This radar system implements polarization diversity through two separate transmitters, avoiding the necessity of a waveguide switching device. This is shown in figure 2.6.

Here due to the high isolation between H- and V-pol channels in both transmit and receive, the overall cross-polar performance of this dual transmit/dual receive system is limited by the

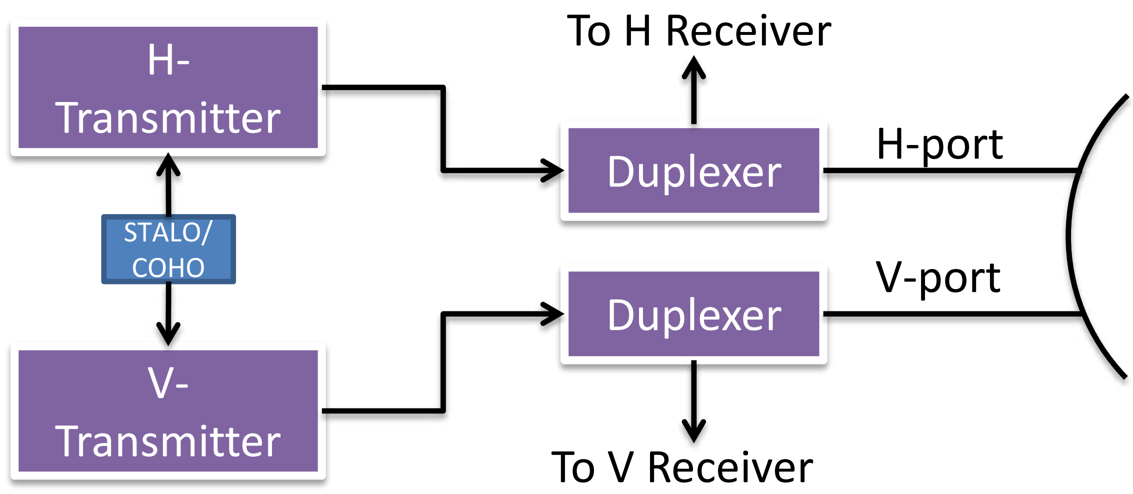

Figure 2.6: Simple block diagram for a dual-transmitter CHILL radar system.

polarization errors of the antenna. Its dual-offset Gregorian antenna reduces antenna cross-polar contamination and antenna sidelobes compared to more traditional center-fed, parabolic antenna. The performance characteristics of the radar is summarized in table 2.1.

The signal processor performs calibration of the system, which comprises of solar calibration, where solar emissions are used to estimate gain difference between the two polarization ports of antenna and the positioner error. The blue-sky measurement gives the estimate of receiver noise floor, and a test signal calibration for measuring receiver gain.

2.5.2 Dual-frequency dual-polarization Doppler Radar (D3R)

The radar has ku and ka band antennas, synchronized and co-aligned, integrated on a common positioner [1]. Both bands have their independent solid-state transmitters, analog and digital receivers, for flexible coding schemes and trigger generation for each polarization state. The system has various compute servers for generating moment data in real time and archiving nodes composed of Redundant Array of Inexpensive disks (RAID) for time series and moment data archiving. All servers, RAID storage, UPS and dehydrator are all in temperature controlled environment. The

Table 2.1: System Specifications of CHILL radar

Specification	Value
Antenna	
Diameter	8.5 m
Gain	43 dB
Beamwidth	1.1 deg
Inter-channel Isolation	-45 dB
Transmitter	
Peak Power	1 MW
Wavelength	11 cm
PRT	800-2500 ms
Pulse Width	0.3 to $1\mu s$
Receiver	
Noise Figure	3.4
Noise Power	-114 dBm at 1MHz BW
Dynamic Range	96 dB
Bandwidth	10 MHz

UPS and generator is capable of automated switching of power, in case of utility power failure. The specifications of D3R are listed in table 2.2.

D3R is able to measure polarimetric moments such as differential reflectivity, differential propagation phase, co-polar correlation coefficient, linear depolarization ratio, at both ku and ka bands. Also dual-frequency ratio (DFR) can be estimated as a ratio of ku-band reflectivity to ka-band reflectivity. D3R can operate in Simultaneous H- and V-polarization mode with uniform PRT or staggered PRT. Additionally, it also has Alternate H- and V-polarization transmit and both polarization receive with uniform or staggered PRT combinations. The staggered PRT mode is based upon 2/3 PRT ratio ($T_1 = 400\mu s$ and $T_2 = 600\mu s$), which allows for estimation of velocity for 2.5 times the unambiguous range, for the uniform effective PRT of $\frac{T_1+T_2}{2}$.

The moment processor allows for calibration using internal noise power generator for receiver gain calibration and also transmit power measurement through the internal calibration loop. The GUI based control and display has been developed, so as to send commands and scan information to the appropriate control and compute servers and configure them accordingly. Also, real time

Table 2.2: System Specifications of D3R radar

Specification	Value
Frequency	Ku: 13.91 GHz $\pm$ 25 MHz, Ka: 35.56 GHz $\pm$ 25 MHz
Operational Range (min)	450 m
Operational Range (max)	39.75 Km
Gain	Ku: 45.6 dBi, Ka: 44.3 dBi
Beamwidth (3 dB)	Ku: 0.86 deg, Ka: 0.90 deg
Cross-polar Isolation	< -30 dB
Transmitter Architecture	Solid State Power Amplifier modules
Peak Power	Ku: 200 W, Ka: 40 W per H and V channel
Receiver Noise Figure	Ku: 4.8, Ka: 6.3
Receiver Dynamic Range	90 dB
Bandwidth	5 MHz (instantaneous)

display for generated moment images, gives the radar operator a view of current radar observations. The various parts of D3R radar are illustrated in figure 2.7.

The research work presented in this thesis uses implementation of schemes on D3R radar, so our focus will be presenting more features of D3R, so that later understanding of the realization and data collected from this radar, would be better.

2.6 Radar Calibration

The radar range equation relates the average received power to reflectivity, via the radar constant (C).

$$P_0 = \frac{C\eta}{r_0^2} \tag{2.27}$$

where η is the reflectivity of scatterer under observation, and r_0 is the distance to scatterer. The radar constant C is given as:

$$C = (cT_0/2)(G_r/l_r)[\lambda^2 P_t G_0^2/4\pi^3][\pi\theta\phi/8ln2] \tag{2.28}$$

This equation has an implicit assumption about the reference plane, where all these quantities are being measured, to be at the antenna port. This is illustrated in figure 2.8 with respect to D3R system.

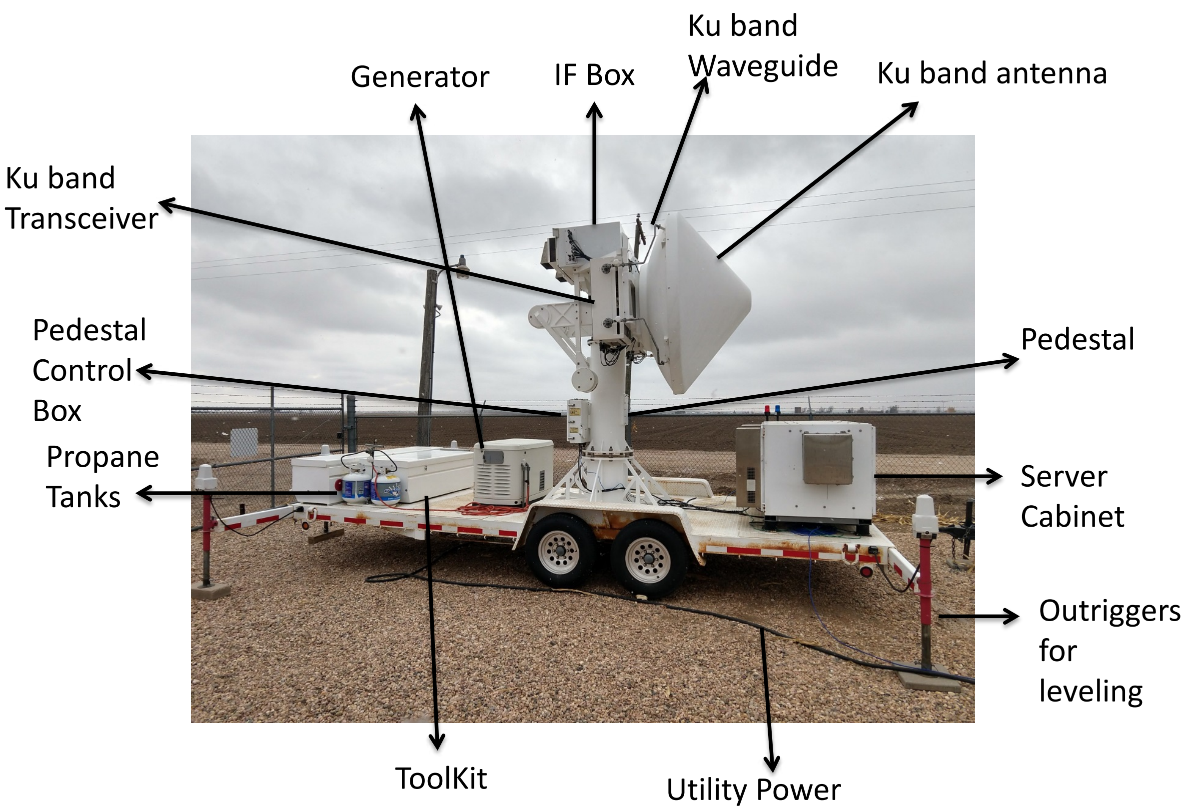

Figure 2.7: The radar on a flatbed trailer, deployed at the CSU-CHILL radar facility in Greeley. This side pose shows the important systems for ku band and the corresponding systems for ka band are on other side of the trailer.

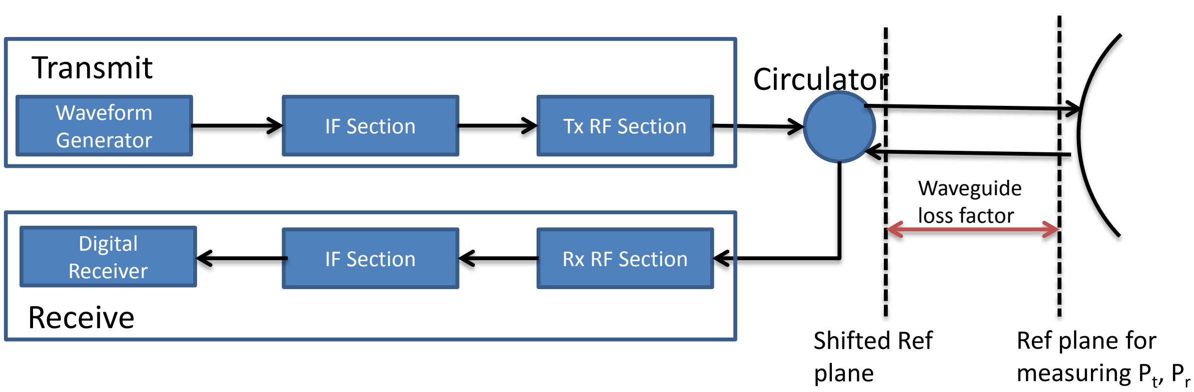

Figure 2.8: This shows the various components of gain and losses included in the radar equation for calibration with respect to the reference plane.

It is more convenient to calibrate receiver by moving the reference closer to receive, as depicted. In such a case, antenna gain has to be reduced by the waveguide loss factor. If P_{ref}^{New} is the received power at the new reference port, then reflectivity η can be expressed as:

$$\eta = \frac{r_0^2 P_{ref}^{New}}{(cT_0/2)(G_r/l_r)[\lambda^2 P_t G_0^2/4\pi^3][\pi\theta\phi/8ln2]} \tag{2.29}$$

and,

$$P_0 = \frac{G_r}{l_r} P_{ref}^{New} \tag{2.30}$$

l_r is the finite bandwidth loss factor and depends upon the shape of the receive filter and transmitted waveform. The equation (2.29) can also be written as:

$$\eta = C_{ref}^{New} r_0^2 P_{ref}^{New} \tag{2.31}$$

where,

$$C_{ref}^{New} = (2/cT_0)\frac{4\pi^3 l_{wg}^2}{\lambda^2 P_t G_0^2}[8ln2/\pi\theta\phi] \tag{2.32}$$

Now the equivalent reflectivity factor (Z_e) can be written as [5]:

$$Z_e = \frac{1}{\pi^5 |K_\omega|^2}(2/cT_0)\frac{4\pi^3 l_{wg}^2}{\lambda^2 P_t G_0^2}[8ln2/\pi\theta\phi] r_0^2 P_{ref}^{New} \tag{2.33}$$

The minimum detectable reflectivity, $Z_{e(min)}$ at a certain range, is defined when the signal to noise ratio becomes unity and hence the P_{ref}^{New} becomes kTB, where B is the noise bandwidth.

2.6.1 Metal Sphere Calibration for D3R

Metal sphere calibration was performed way back in 2013 for D3R, using a 10 inch metal sphere, for both ku and ka bands [1]. The metal sphere was tethered to a helium balloon. Figure 2.9 shows the observed power measurements, of a metal sphere of the same diameter to the one launched at various ranges from the radar. The analytically derived expected power observation for a metal sphere of the same diameter is included as a solid curve. This provides a complete

(a)

(b)

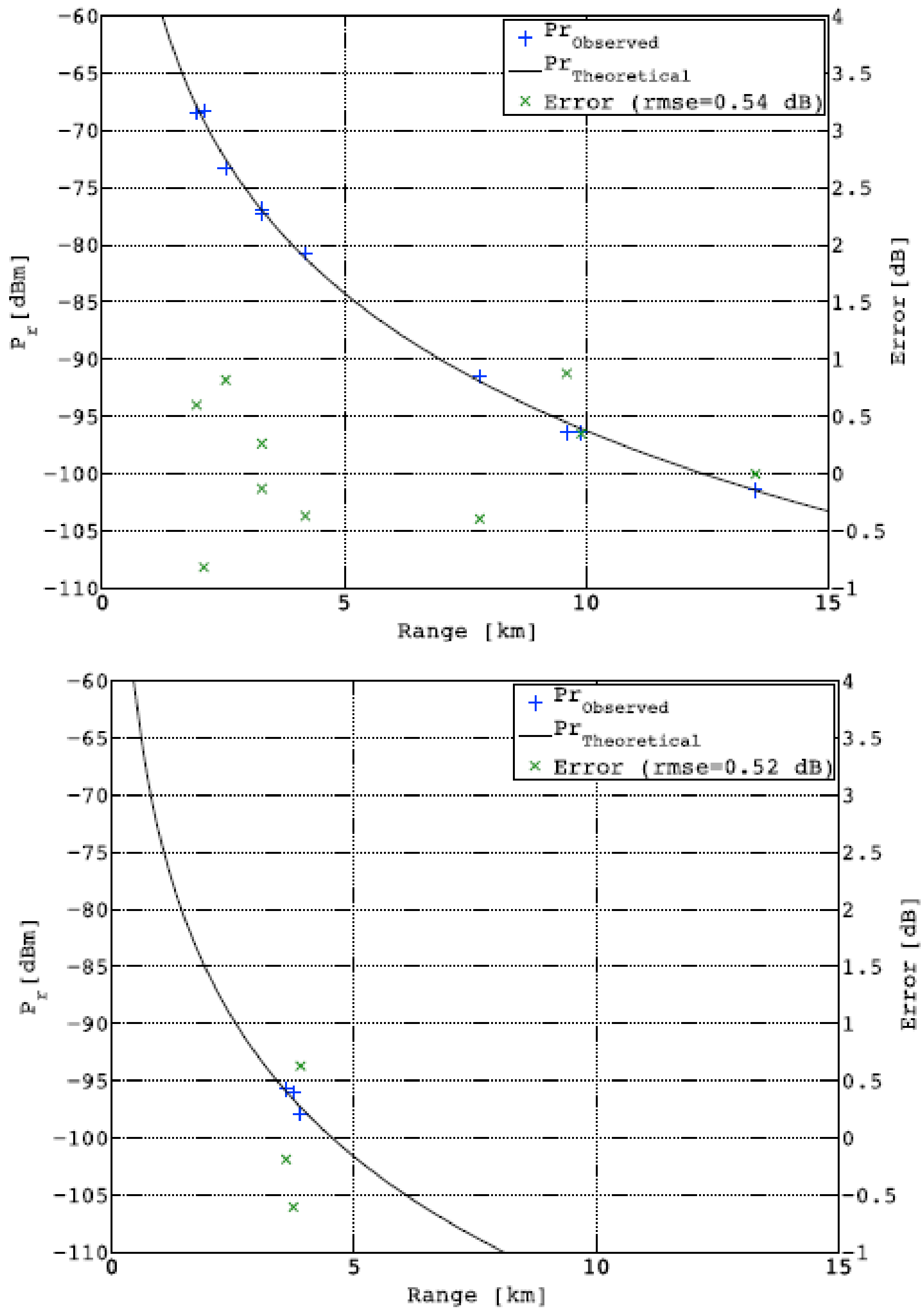

Figure 2.9: (a) depicts the power observed during the sphere calibration exercise for the Ku band radar. It is compared against the theoretical values. (b) depicts the same observations but for Ka band radar [1].

end-to-end system calibration for reflectivity and the observations shows remarkable agreement with theoretically expected values showing that the radar was well calibrated.

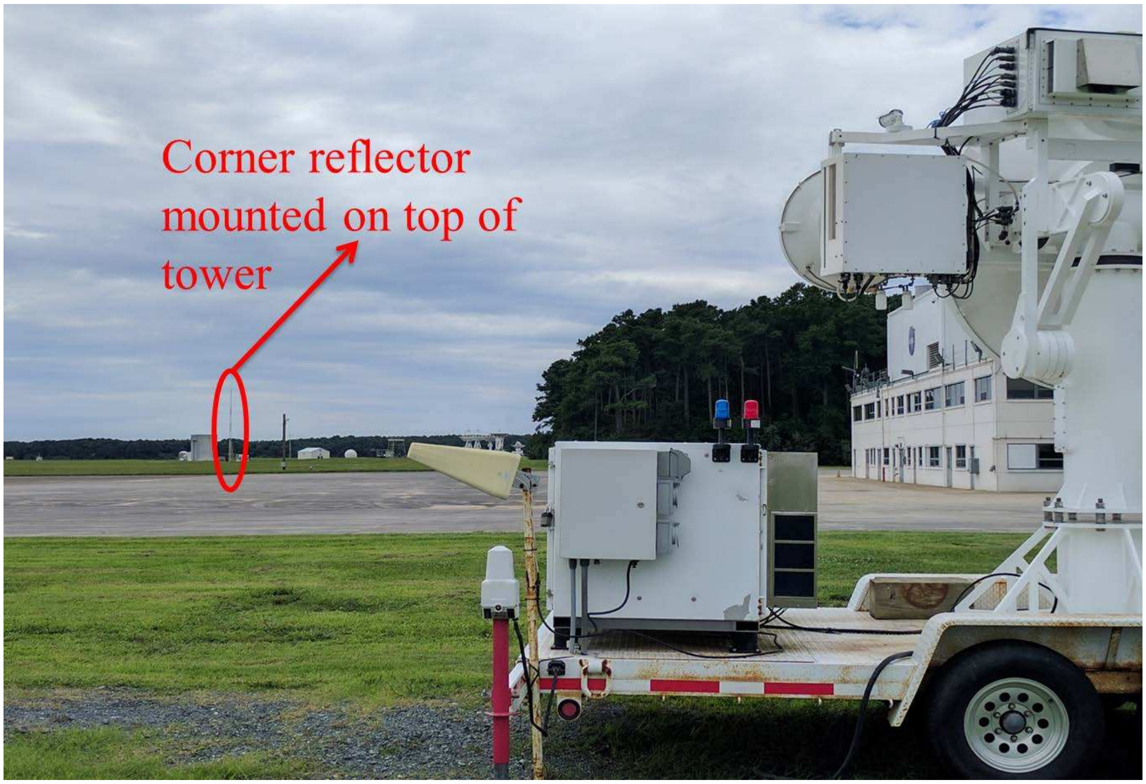

Figure 2.10: The view of tower and corner reflector from radar.

2.6.2 Corner Reflector Calibration for D3R

After the upgrade of D3R IF electronics, the corner reflector calibration exercise was undertaken in July 2017 at Wallops Flight Facility, VA, to check system calibration of reflectivity, before shipping the radar to South Korea for the Winter Olympics, 2018. The corner reflector was mounted on top of tower, 450 m away from radar, as shown in figure 2.10.

A much detailed view of the tower and corner reflector mounted on top of it, is shown in figure 2.11.

The height of the tower is 100 feet. The corner reflector RCS was computed using:

$$\sigma = \frac{4\pi L^4}{3\lambda^2} \tag{2.34}$$

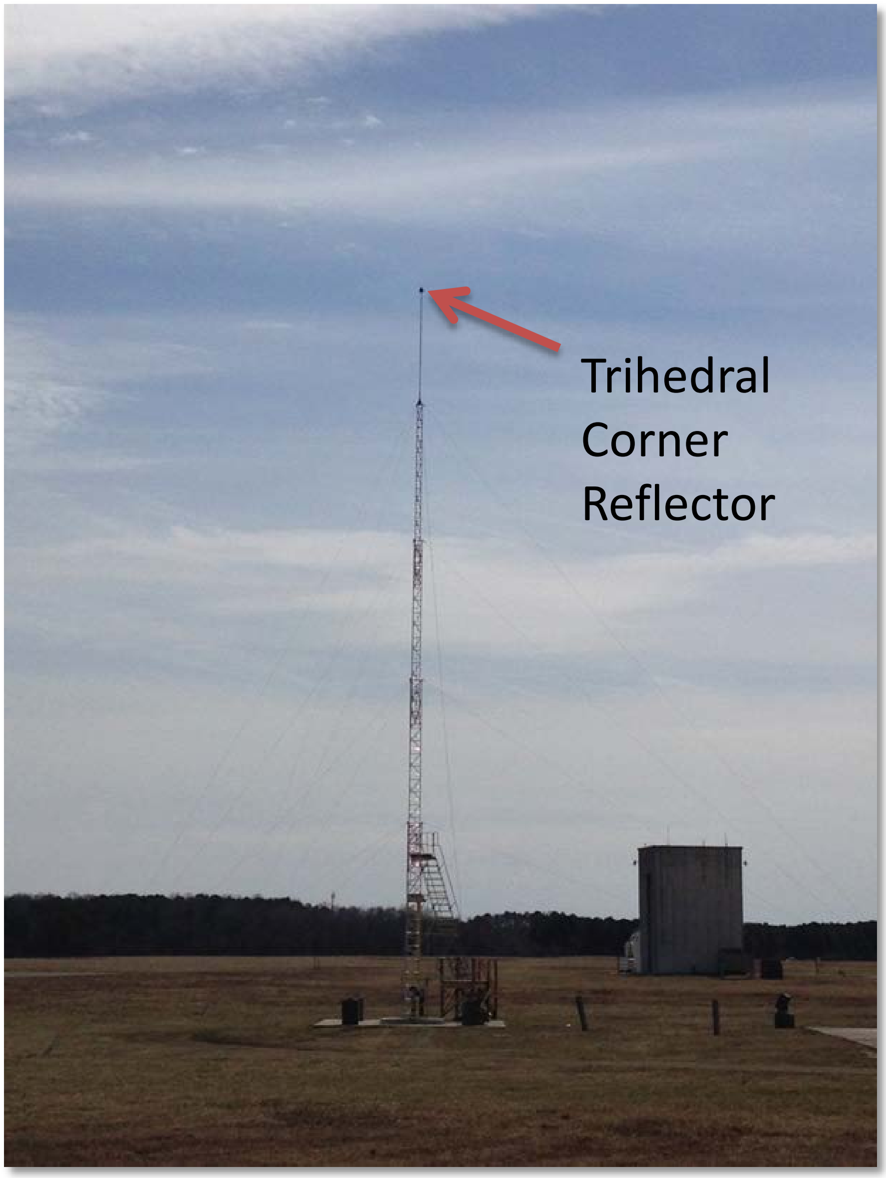

Figure 2.11: The corner reflector mounted on top of tower for the calibration exercise at WFF.

and at ku band frequency, it turns out to be $6.3m^2$ and at Ka band, the RCS was computed to be $41.2m^2$. The expected power return from corner reflector can be theoretically computed using equation 2.6. We need to adjust the timing for transmit waveform a bit, so that the straddle loss could be minimized. The theoretical values were then compared against the observed values of reflectivity, and bias could be computed. The tower was detected at radial 198 deg azimuth and

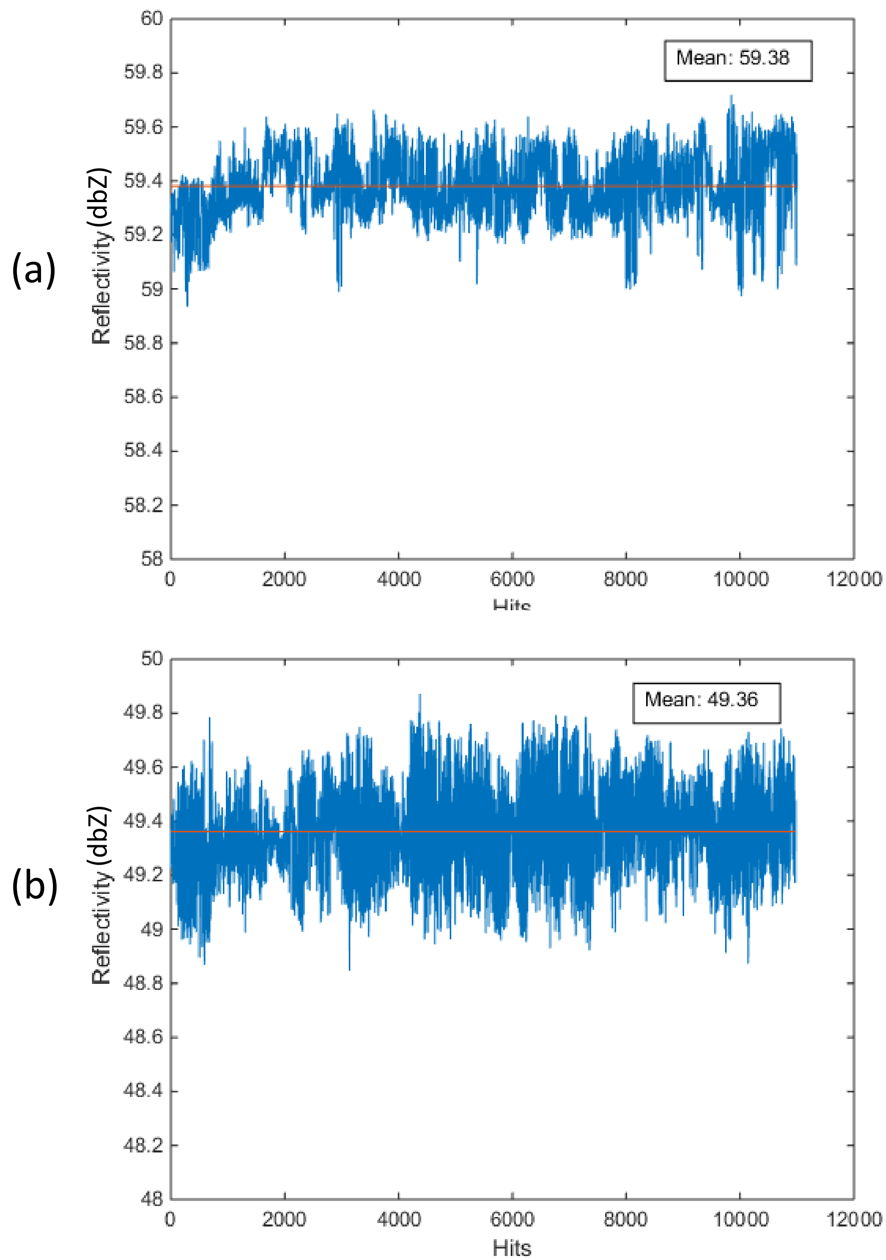

Figure 2.12: (a) are the maximum reflectivity values for ku band radar for the corner reflector obtained after the timing adjustments made. (b) depicts observations under similar settings as (a) but for ka-band radar.

1.98 deg elevation. The Mean reflectivity is plotted in figure 2.12 for the maximum signal strength obtained in a sweep, after the timing adjustments were made.

Chapter 3

MIMO Techniques

3.1 Introduction

Multiple input multiple output (MIMO) radar has been a concept which was lying around for years but now with ever increasing computing power, it is being realized. MIMO radar has multiple antenna elements in both transmit and receive, which looks like a phased array configuration. However, unlike phased arrays, MIMO is able to transmit different waveforms that are orthogonal. The receive processing consists of a series of matched/mismatched based filters to separate out these echoes.

MIMO radar is superior to conventional phased arrays (electronic scanning) and the parabolic reflectors (mechanical scans) with better localization accuracy and angular resolution [19]. These can be attributed to the fact that due to the waveform diversity, the output signals of different channels appear as spatial samples corresponding to the convolution of the transmit and receive aperture phase centers ([14]), which produces additional virtual array elements [18]. The phase centers of the transmit and receive aperture in MIMO radar system can be increased dramatically, which extends the array aperture ([15]) and provides a potential for the system to have a higher spatial sample ability and space resolution than a conventional reflector antenna or a phased array system.

MIMO based phased array radar has lot of potential for improving weather detection and enhancing the quality of polarimetric moments. This is because a MIMO array can potentially have more number of independent samples and wider virtual array creation leading to higher spatial resolution. This is useful to identify some of the critical features in storms or tornadoes, where high resolution image can improve the quality of forecasting. The MIMO concept was first developed for communications systems, for which orthogonal transmit-receive channels were used to circumvent channel fading [17]. However, this type of configuration used widely separated antenna to exploit spatial diversity. Our application uses colocated MIMO radar using multiple transmit waveforms to obtain further degrees of freedom and improve radar performance. In this chapter, we focus on colocated MIMO radar (also known as coherent MIMO), which requires the use of orthogonal waveforms on transmit has increased complexity and flexibility compared to phased array operation. MIMO radar has better angle estimation accuracy compared to phased array radar because of an apparent decrease in antenna beamwidth when the linear array is operated as a MIMO radar. For a MIMO radar system with M transmit and N receive antennas, placed at a spacing of d_T and d_R, respectively, $d_T = Nd_R$ yields a virtual array of NM receive elements which determines the aperture length. This can yield better spatial resolution for weather phased array systems. On similar lines, we can say that a spatial resolution similar to the traditional system can be achieved using a fewer number of antennas [14]. However, it is well known that MIMO system suffers from interference due to parallel transmission of the probing signals (waveforms) which demands appropriate receiver to suppress the interference and the same concept holds true for a weather MIMO system as well. It can be observed that orthogonality is a key requirement to gain performance benefits claimed. Thus the receiver and transmitter should ideally consist of perfect orthogonal waveforms with appropriate matched/mismatched filters. Such a waveform design has been detailed in chapter 5. It dwells on the design of a polyphase code pair and a mismatched filter pair that can achieve low level of peak auto-correlation and cross-correlation functions. A low level of peak cross-correlation function is essential to obtain orthogonality between the code/filter pairs. This can also be accomplished using the same waveform but modulated with different carrier frequency and this idea is explored in the chapter 6. It even deals with recovering weather radar moments under pulse to pulse frequency agility conditions.

Another benefit of MIMO for weather radar systems is the faster update rates available because of synthesis of a twice broad transmit beam pattern due to quadrant wise transmission (proposed here) and then using digital beamforming in receive to synthesize four simultaneous beams. This would cut down the overall volume scan time by a fourth. However, the downside is the loss of

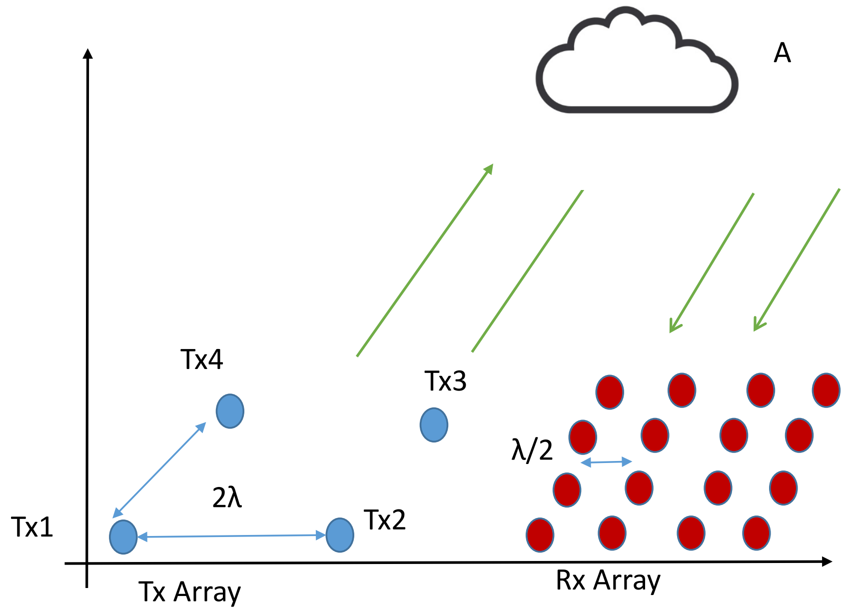

Figure 3.1: A conceptual representation of a weather MIMO radar configuration with M transmit and N receive antennas [16].

directivity (and SNR) due to broad transmit pattern. The update rate is an advantage for weather events which are evolving fast and in general for weather forecasting and nowcasting systems.

A higher number of independent samples is possible through a weather MIMO system because orthogonal waveforms from different quadrants of the array will likely increase the uncorrelated samples from the same volume in space where the weather event is being observed. These higher number of independent samples will aid in accurate measurements of weather radar products like reflectivity, velocity, spectral width etc (reduce errors).

A simplified diagrammatic representation of a weather MIMO system is depicted in Fig. 3.1. It is observing a weather event in the far field and is equipped with co-located antennas. Therefore, the directions of the target relative to the different transmit antennas and the receive antennas are the same, and the RCS of hydrometeors corresponding to different transmit–receive antenna pairs are also the same. Here the receive elements are in a 4x4 grid of $\lambda/2$ spacing and the corner elements are both transmit and receive. However, an important point to note here is that since the transmit elements are either energized one after the other (in case of time multiplexed operation) or they transmit individual orthogonal waveforms, each elemental pattern is omni directional (as there is no beamforming in transmit and beamforming happens only in receive). With this, the weather radar would be able to see all directions instantaneously, an application very favorable for weather imaging. This is because all of the receive beams could be formed simultaneously by a 2-dimensional fast Fourier transform across the elements of the array. This weather imaging capability of a MIMO array can be very useful for rapidly evolving storms and tornadoes where high update rates of the event can be very beneficial to save thousands of lives by issuing warnings at the right time. For this type of scenarios, weather MIMO arrays can also help with high resolution data to classify the event type better and higher update rates can lead to faster decisions to evacuate or take other steps in a timely manner.

3.2 Virtual Array formation for a weather MIMO array

A benefit of coherent weather MIMO radar is the ability to increase the angular resolution of the physical antenna array by forming a virtual array. Thus, by carefully selecting the geometry of the transmit and the receive arrays, we can increase the angular resolution of the system without adding more antennas to the arrays. In a coherent weather MIMO radar system, each antenna of the transmit array transmits an orthogonal waveform. Because of this orthogonality, it is possible to recover the transmitted signals at the receive array. The measurements at the physical receive array corresponding to each orthogonal waveform can then be stacked to form the measurements of the virtual array. The ways to obtain orthogonality has been highlighted in the introduction section. Time division multiplexing (TDM) is another way to achieve orthogonality among transmit channels.

Another significant point has been made in [20], which will be utilized further in arriving at a geometry for the weather radar antenna. It says that a MIMO system can be mapped to a conventional radar with virtual RX positions corresponding to the spatial convolution of the TX and RX phase centers. This can lead to a larger virtual array aperture, and therefore, to a higher resolution if a standard beamformer is used.

Thus it is necessary to distinguish the signals coming from different TX antennas at reception, which makes it possible to extract the information from each combination of the multiple TX and RX paths. This could be achieved via coding (discussed in chapter 5) or frequency division multiplexing (discussed in chapter 6).

With all this in mind, let's take a look at the proposed weather MIMO phased array concept. The normal surveillance could be carried out with this weather radar in the phased array mode, with the phase centre of the transmit at the physical centre of the array. However, if some weather event is to be observed with high spatial resolution, we could switch it to the MIMO mode where quadrant wise sequential transmission could take place (in case of TDM based MIMO) or in parallel (with orthogonal phase codes). In both these case, the weather MIMO mode will provide higher spatial resolution because of virtual array.

As already stated in earlier paragraphs that the weather MIMO configuration is equivalent to the spatial convolution of the transmit and receive phase centers and the formation of virtual array. This virtual array dimensions are 1.5 times the physical array size (in both axes), evident from the Fig. 3.2, hence the beamwidth reduction will happen by this factor and the spatial resolution will improve.

Since some of the virtual elements would appear on top of each other, these elements could aid in improving the estimation of polarimetric variables by providing with more independent samples and hence the reduction in error variance for these estimates.

3.3 Importance of MIMO systems for distributed targets

In this section, we demonstrate the importance of MIMO techniques for distributed environments which are typical of a weather event. Let's take an example of a tornado system, the main requirement would be to be able to observe tightly coupled velocity features of a tornado and also the hook shaped echoes present in the reflectivity profile. Such type of specific feature detection can be better done with a weather MIMO based system. Let's take a look a typical reflectivity profile of a tornado system as in Fig. 3.3. There are high reflectivity regions in the south-east sector

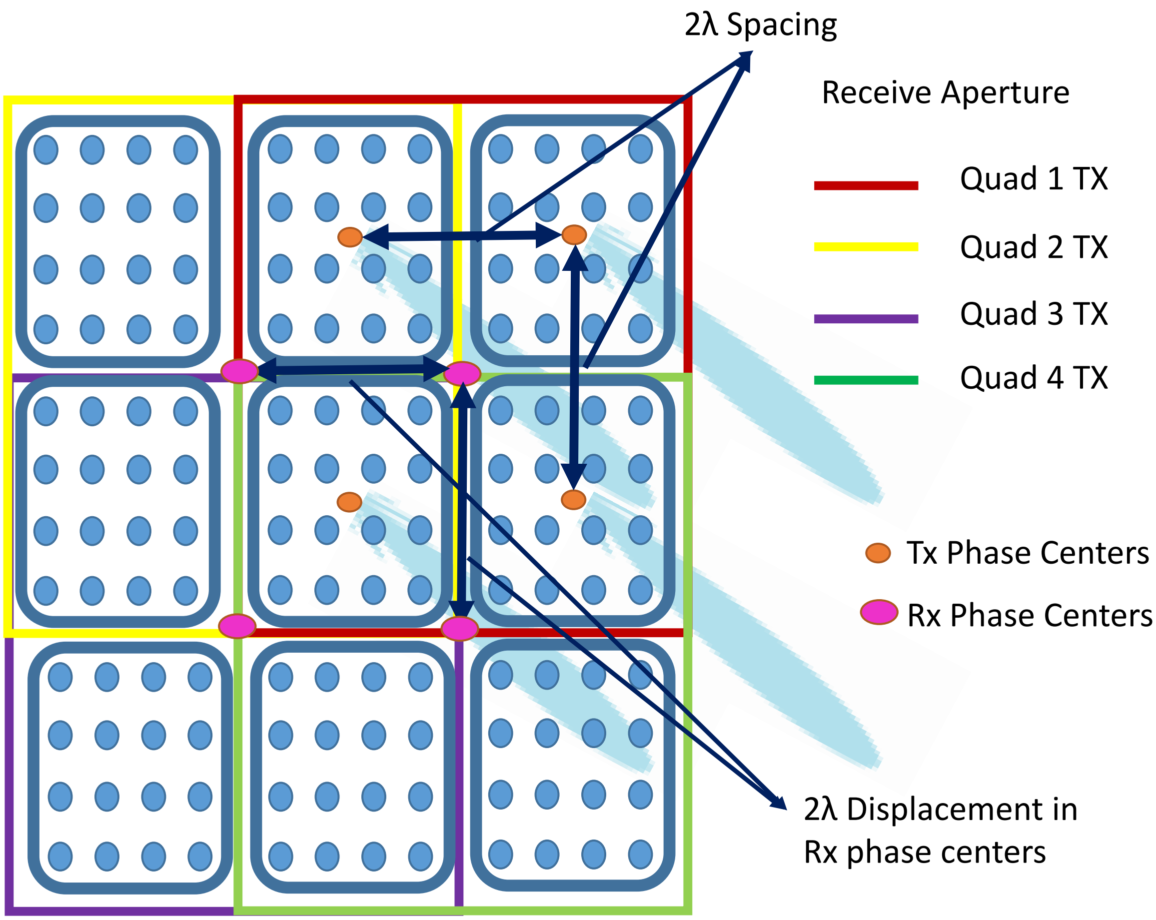

Figure 3.2: A 8x8 element phased array with multiple transmit phase centres based on quadrant. The whole array is divided into 4 quadrants.

and hook shaped profile clearly evident. Such high gradients of reflectivity in this region requires high spatial resolution to capture and give an accurate representation of the hook feature.

Another feature for a tornado event could be seen in the opposite velocity direction cores formed in and around the central part of the hook feature of a tornado. This can be seen in the circles marked in the Fig. 3.4. It can be easily observed that we need high spatial and Doppler resolution to see such features in detail.

Let's summarize some of the major benefits of MIMO systems for weather like targets:

1) Better spatial resolution than phased arrays or reflector antennas due to the virtual array aperture size bigger than the physical array.

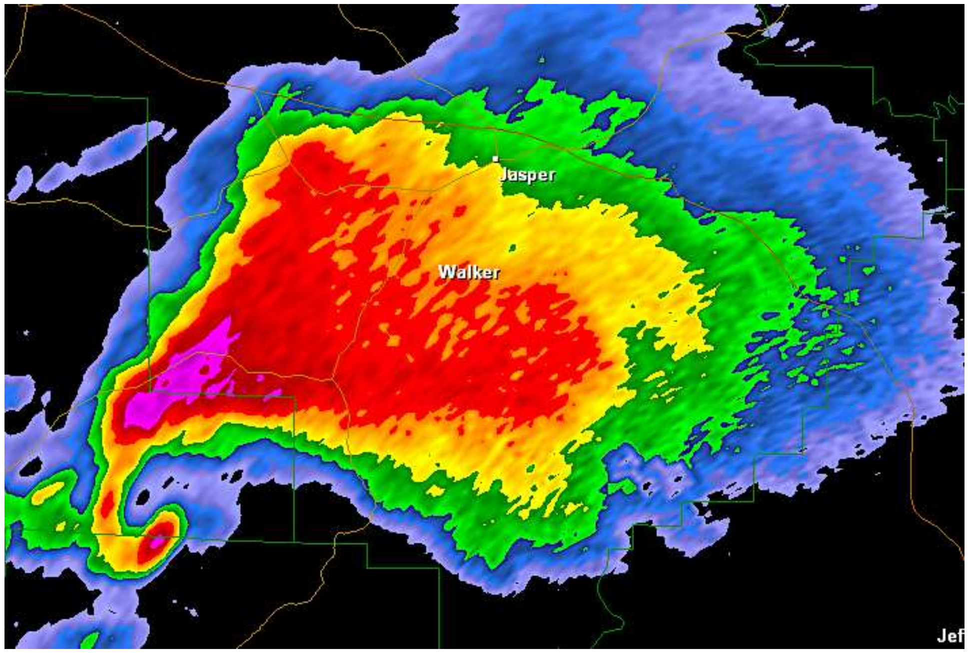

Figure 3.3: A typical hook shaped feature of a tornado event (image from AccuWeather website).

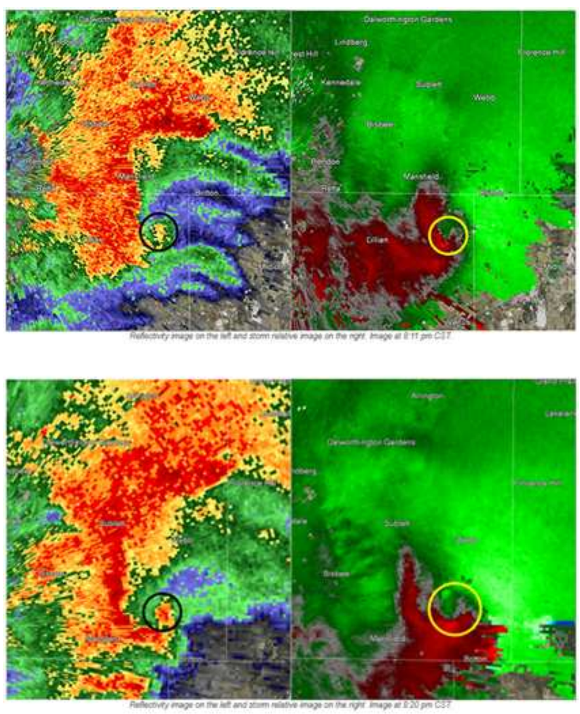

Figure 3.4: A typical hook shaped feature and the opposite velocity couplets of a tornado event. On the left are the reflectivity profile and on the right are the velocity profiles. Red depicts positive velocity and green shades are the negative velocities (image from NWS website).

2) More number of independent samples available for polarimetric weather radar moment estimation which is likely to give higher level of accuracy to the estimated moments than a phased array.

3) Weather event imaging possible with the use of high power transmit elements and multiple receive beams via digital beamforming.

4) Faster update rates possible with multiple receive beams.

3.3.1 Our Approach

In our proposed MIMO array for weather radar, we use quadrant wise transmission using polyphase orthogonal codes or frequency division multiplexing (FDM). With this, we can get virtual array dimensions which is one and a half times bigger than the physical dimensions, leading to possible increase in spatial resolution. We use beam steering in both transmit and receive arrays. Under this configuration, the transmit beamwidth is twice that of the receive in both the scan dimensions. The update rate will be twice in both the dimensions compared to a phased array.

Initially we start by simulating the antenna geometry and antenna patterns to gain insight into the weather MIMO capabilities of a phased array antenna. Here are the simulation parameters:

1) Centre frequency : 9.4 GHz (X-band).

2) Inter-element spacing = $\lambda/2$ = 16mm.

3) Beamwidth in both axes = 1.5 deg.

4) Dimensions:

Virtual array: 0.8m x 0.8m

Physical : 0.54m x 0.54 m

The simulation of the antenna pattern with this setup is shown in Fig. 3.5.

However, with taylor taper applied on the receive and retaining the beamwidth of 1.5 deg in both azimuth and elevation, the dimension of the virtual array comes out to be approx 1m x 1m size whereas the physical dimensions are at 0.67m x 0.67m size. The antenna size for both virtual and physical arrays have increased to compensate for the mainlobe broadening occurring due to the

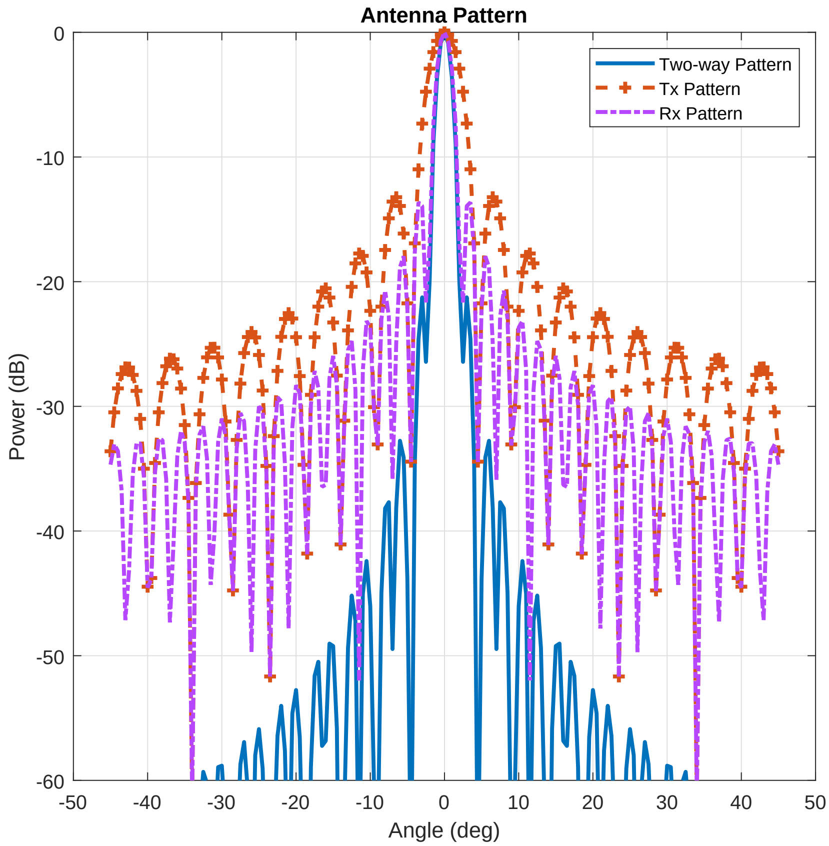

Figure 3.5: Transmit, Receive and two way patterns for the proposed weather MIMO system without tapering.

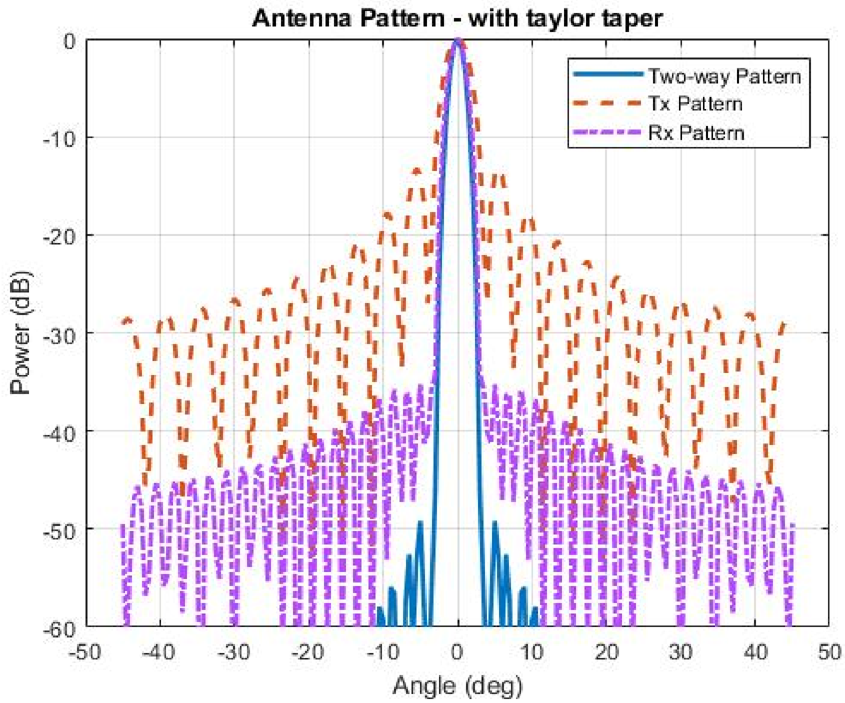

Figure 3.6: Transmit, Receive and two way patterns for the proposed weather MIMO system with taylor taper applied.

taper applied. The antenna pattern is shown in Fig. 3.6, where the first sidelobe can be observed to be at 50dB below the mainlobe peak power.

If we do the size comparison with the CSU Frontx phased array weather radar system, which operates in X-band, it has boresight beamwidth of 1.5 deg which is comparable to our simulated system. However, it's size is 1m in the electronic scan dimension. The same beamwidth could be obtained with 0.67m size with MIMO techniques. This can lead to savings on size, weight and power. Another example could be the NASA D3R which opeartes in Ku-band and has parabolic reflector antenna. It has a beamwidth of 0.9 deg in both dimensions and the dish size is approx. 1.83m diameter. If we scale the dish size for the operating frequency of X-band and beamwidth of 1.5 deg for comparison sake with our simulation parameters, we see that since the size would be smaller for a broad beam but then the frequency would scale it back to the same dimension. Thus compared to 1.83m diameter of the dish, our simulated value of size which is 0.67m is much smaller. There is a value addition in terms of size, weight and power with MIMO techniques in this example also.

The number of independent samples from a MIMO configuration is certainly very important from the perspective of reduced standard deviation of errors in estimation of different weather radar moments. From [5], it can be seen that the variance of mean power is given by:

$$var(P_{est}) = \frac{(P_{mean})^2}{N} \sum_{l=-(N-1)}^{(N-1)} (1 - \frac{|l|}{N} \rho_p[l]) \tag{3.1}$$

where N is the number of samples, l is the time lag and $\rho_p[l]$ is the correlation coefficient at time lag l. If the samples are uncorrelated, then $\rho_p[l] = 0, l \neq 0$, and the variance of the estimated power becomes inversely proportional to the number of independent samples.

Fig. 3.7 shows the standard deviation of mean power estimate at S-band ($\lambda = 10$ cm) in dB shown for Gaussian-shaped Doppler spectrum with various spectral widths (in m/s). In our proposed quadrant wise transmission from the weather MIMO phased array of 0.67m x 0.67m size, there are likely four times the number of uncorrelated samples available for processing, that can reduce the variance of estimated moments as evident from Fig. 3.7.

Additionally, with the proposed configuration, there are likely one and a half times more spatial independent samples available in a weather MIMO because there will be a half quadrant overlap between the virtual elements and the physical elements as the transmit phase center moves from one quadrant to the another. This will give rise to double the elements for the overlapped portion of the array. This can be better depicted in Fig. 3.8 with the help of 8x8 array MIMO virtual array formation.

The update rate of the CSU Frontx X-band phased array radar is 1ms. Assuming a coverage of ± 45 deg in azimuth direction, with a 1.5 deg beam, it would require 60 ms to cover this sector. However, with the weather MIMO array, it will be able to scan this volume in half time by synthesizing two beams in azimuth using digital beamforming.

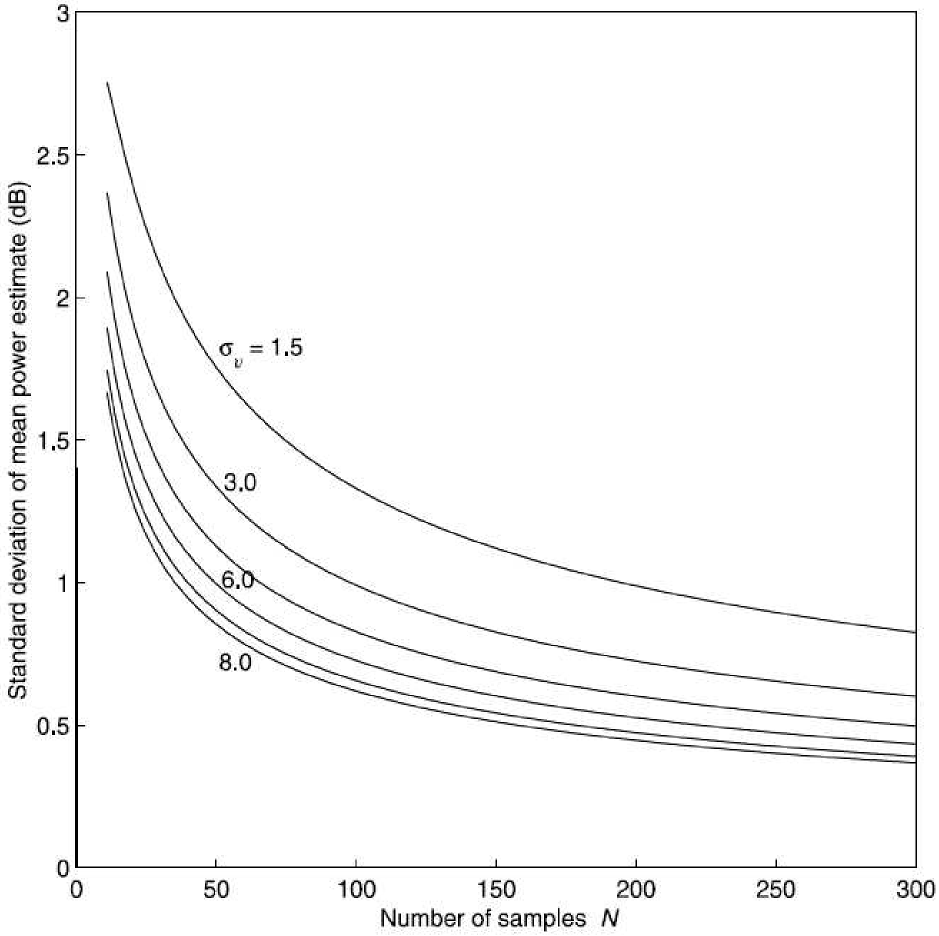

Figure 3.7: The dependence of standard deviation of the mean power estimate with the number of independent samples. [[5]].

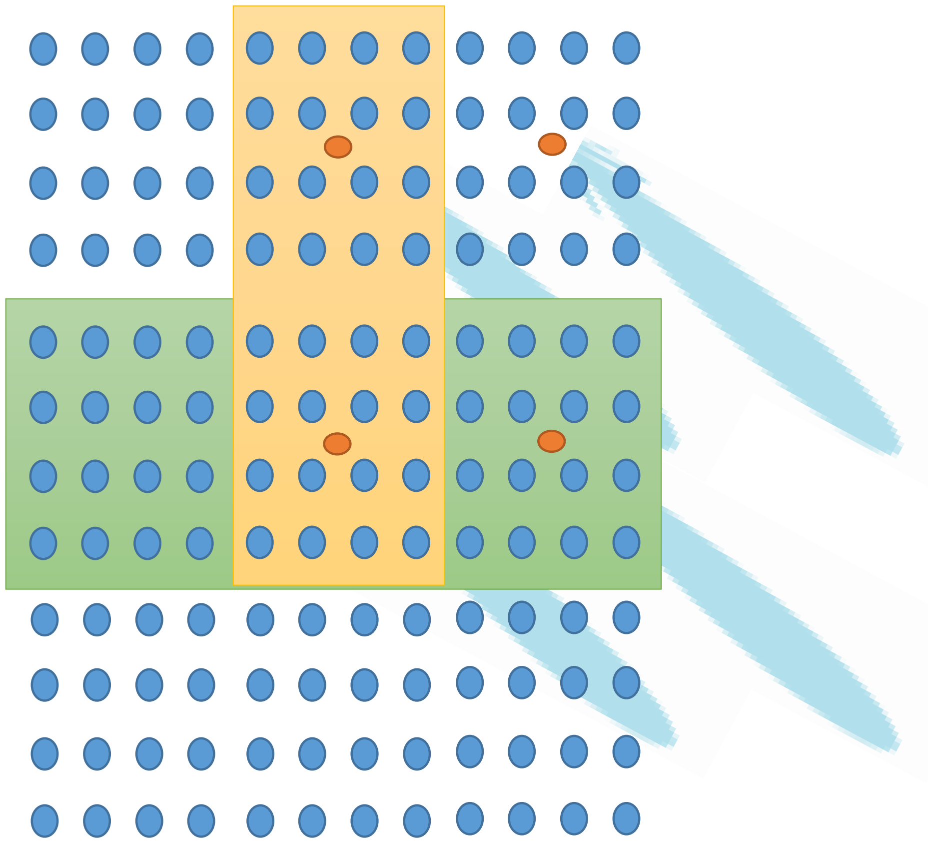

Figure 3.8: The depiction of common spatial receive elements as the transmit phase center moves. The highligted portion of the array gives rise to one and half times more number of independent samples.

3.4 Analysis using simulated weather return echoes

We start with simulation of the two way pattern of a normal phased array with 2 deg beamwidth and then MIMO virtual array with 1.5 deg beamwidth. The simulation setup is at 9.4GHz frequency (X-band) with taylor taper. The physical dimension of this array is 0.67m x 0.67m. Our aim first would be to show how much of an error in a reflectivity profile for a distributed target as weather, will be observed with a 2 deg beam using a standard phased array as against the 1.5 deg beam synthesized using MIMO beamformer. The assumption of 1.5 deg beam using MIMO comes from the formation of virtual array which is one and a half times bigger than physical aperture using quadrant wise transmission. To show the effectiveness of recovery of a reflectivity profile in azimuth using 2 deg beam and 1.5 deg beam respectively, we start with a high spatial resolution reflectivity profile sampled at 0.02 deg in azimuth dimension at a fixed range. We try to reconstruct this high resolution profile with these two different beams at every 1 deg azimuth steps (the electronic beamsteering would switch both the beams in 1 deg steps). Then we calculate the error in the reconstructed profile for these two beamshapes. The profile has a features of reflectivity fluctuating between low to high and then again back to low within a short azimuth span. The simulated reflectivity profiles are generated using a weather radar echo simulator, which is configured to generate pulse echoes with corresponding reflected power (scaled with radar constant to match the reflectivity values). Next the simulated power returns are averaged out and modulated with the radiation pattern in the spatial dimension (Refer to Fig. 3.9). Also refer to steps given in Algorithm 1.

Now let's see the reconstructed profile using the beamshape of 2 deg and 1.5 deg, which was obtained with 0.67m x 0.67m size physical array and 1m x 1m virtual array obtained with MIMO technique. Fig. 3.10 gives the two way radiation patterns of the two beams that we are considering here to evaluate the effectiveness of MIMO arrays for weather. Both patterns have sidelobes below -55dBc because of the taylor taper used. The bigger mainlobe of the radiation pattern of 2 deg beam has a higher negative impact on the reconstruction ability for sensing the low to high transitions or vice versa in a reflectivity profile in a distributed target as against 1.5 deg beam. This is because

Algorithm 1 Time Series simulation method for reconstruction of reflectivity profile using two different beamshapes.

1: Simulate the time series echo returns from weather at a fixed range and number of pulses along the beam for every 0.02 deg azimuth degrees as per the reflectivity profile.
2: Start with beam center at 0 deg and multiply the beam pattern with the reflectivity profile for the span of the beam.
3: Average along the pulse dimension.
4: Repeat steps 2 and 3 for every 1 deg increment in azimuth.
5: Do these steps for both the beamshapes.
6: Plot the reconstructed profile with both beamshapes along with the original profile.
7: Calculate error between desired and reconstructed values.

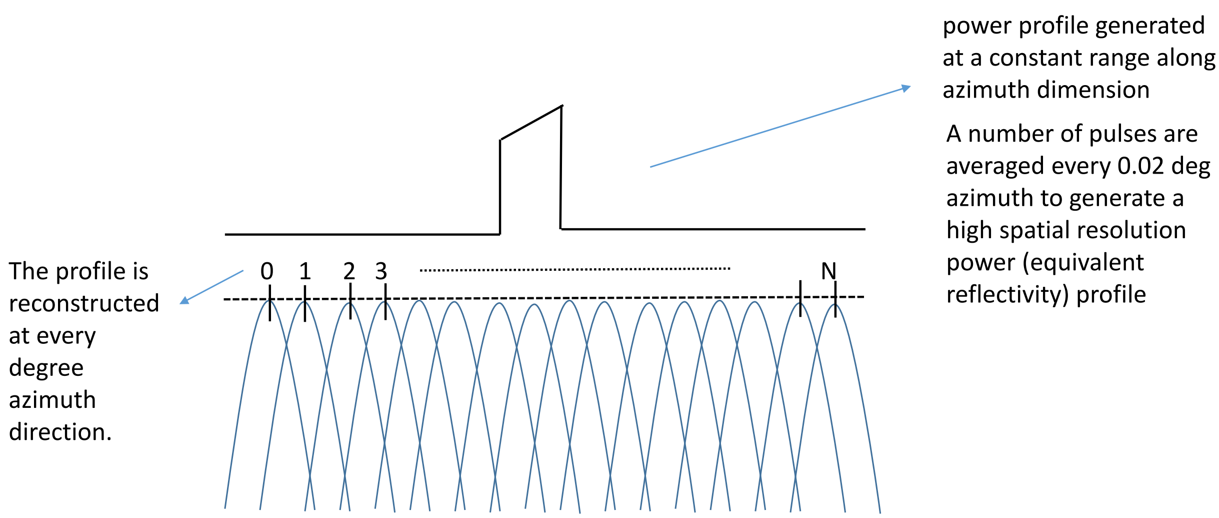

Figure 3.9: The process of simulating the constant power weather echo profile across all azimuths and reconstruction with a beampattern.

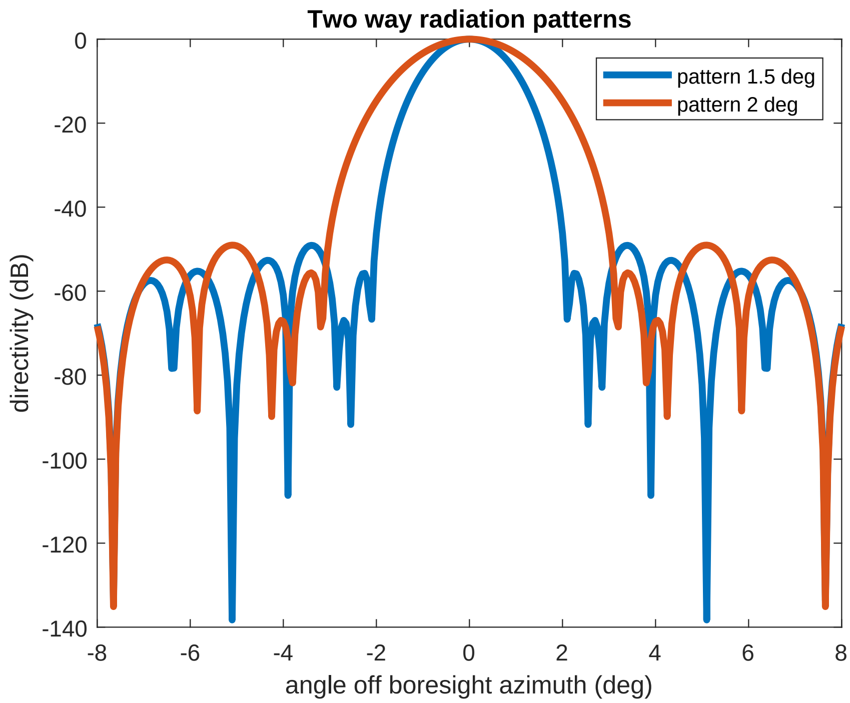

Figure 3.10: The process of simulating the constant power weather echo profile across all azimuths and reconstruction with a beampattern.

the bigger mainlobe of 2 deg beam is representative of a bigger volume in space and cannot track fast changes in reflectivity profiles. Fig shows the reconstruction abilities of the two beampatterns discussed. It is evident that the 1.5 deg beam has a comparatively less error in reconstruction than the 2 deg beam.

3.5 Summary

The overall takeaway from this chapter is that the MIMO configuration is beneficial for weather radar as it improves the spatial resolution of the array without physical addition of more elements and provides more number of independent samples. But the price to pay is reduction in SNR and computational complexity of the system.

In this chapter, we simulate the beam patterns of the proposed array with 1.5 deg beamwidth which results in a 0.67m x 0.67m physical size. We also show through weather time series simula-

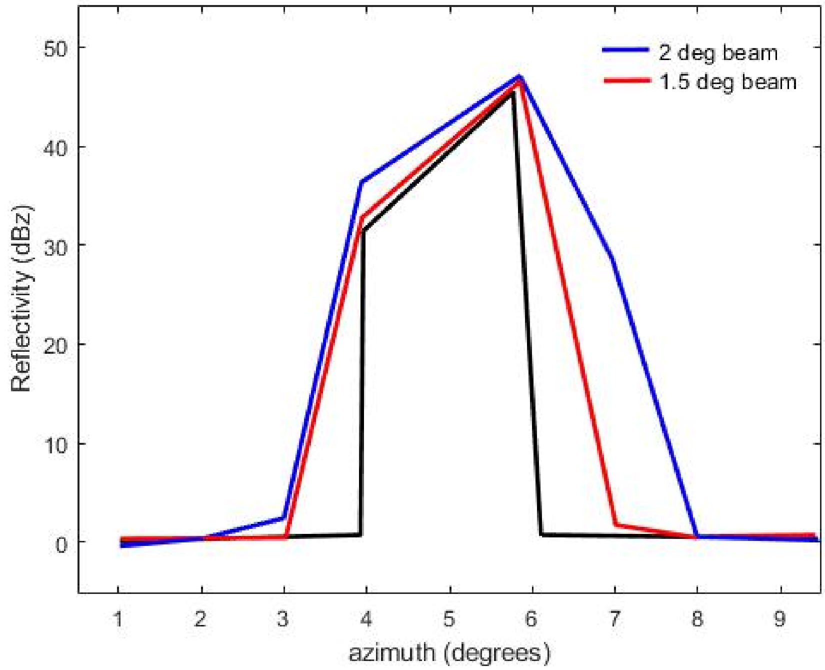

Figure 3.11: The reconstructed profile using 2 deg beam without MIMO and 1.5 deg beam (with MIMO), where the black line represents the true reflectivity profile.

tions that this array would result in less spatial errors on the measured reflectivity as compared to a 2 deg beam array which would result without the virtual array and MIMO techniques.

Chapter 4

NASA D3R ENHANCEMENTS: DATA AND CONTROL FEATURES

4.1 Motivation for upgrade

During the year 2017, D3R went through a major upgrade, specially with the digital receiver and waveform generation subsystems. In this chapter, the D3R IF system upgrade will be discussed with a focus on key features of the new system. One of the primary motivations for this upgrade is to enable additional radar sensitivity and improve range resolution to 30 meters. Therefore, there would be an improvement of upto 5 times in range resolution. Moreover, for resolution of 150m, there is possibility of enhanced sensitivity by tuning waveforms and filters. Additionally, there is a chance of improvement in quality of dual-polarization moments like differential reflectivity (Z_{dr}), linear depolarization ratio (LDR), etc because of reduced cross-polar contamination. This is possible through orthogonal waveform design. There is also possibility of improved multi-trip suppression and retrieval with waveform and pulse to pulse frequency control. Hence, the flexible architecture would enable research into new radar signal processing techniques to enhance performance.

As a part of the upgrade process, the waveform generator and digital receive sub-systems were changed along with their Intermediate Frequency (IF) electronics [51]. As a result of change in IF sections, the clock generation scheme and the IF up-converter and down-converters have also been modified. Both the IF waveform generator and the digital receive sections have been packaged into a high speed digital module, based on Virtex 6 Field Programmable Gate Arrays (FPGA). The ADCs and DACs have a high spur free dynamic range (SFDR), so as to enable sampling of intense storms to light cloud and snow observations. With high dynamic range, the sensitivity of the system can be improved, if the receive gain is tailored to toggle the lowest resolution bit of the

ADC converter. This will enable the noise to be contained in the lowest bits (with a fine tuning of the receiver gain). Usually, if the SFDR is not good, additional spurious signals also be detected along with the weather echoes. These spurious signals may be due to the inter-modulation products of the mixer, which came in band due to aliasing and improper filtering or due to non-linearities of the ADC device itself. In this chapter, we present analysis to contain these inter-modulation products and demonstrate the filtering requirements for such high dynamic range requirements. Also, we would highlight many such design features for the IF Stages, which has been incorporated in D3R as part of version 2.0 system for enhanced resolution, sensitivity and software control.

4.2 Design and Simulations

The digital module with DAC interface can generate upto a certain frequency range to maintain reasonable sampling rates with which digital in-phase and quadrature samples can be interfaced from FPGA to DAC device and also a feasible filter design. The IF stages and the analog bandwidth of these IF stages, were designed with the help of simulations of the mixer products and the rejections required in order to meet the dynamic range requirements. The challenge was to remove the Local Oscillator (LO) feedthrough, which is the high power spurious component, which can be trade-off with other intermodulation power levels. This made us to fix the analog bandwidth to get adequate rejection of LO feedthrough and other mixer products and harmonics [51].

With the simulations for the mixer products and the amount of gain required in the IF sections, the design evolved for the up-converter portion for the Ku and Ka band. The overall design philosophy was to segregate the LO generation portions to clock box and IF up-convert stages to waveform box. The LO power requirements were satisfied partially at the clock box level and partially at the waveform box level. Thus the design meets requirements of power to drive the transceiver inputs and maintains good spectral purity of signals (managed through adequate filtering stages). Based on simulations of mixer products and LO leakage, the filtering requirements were determined. These requirements are more stringent for the up-convert stages than the receive,

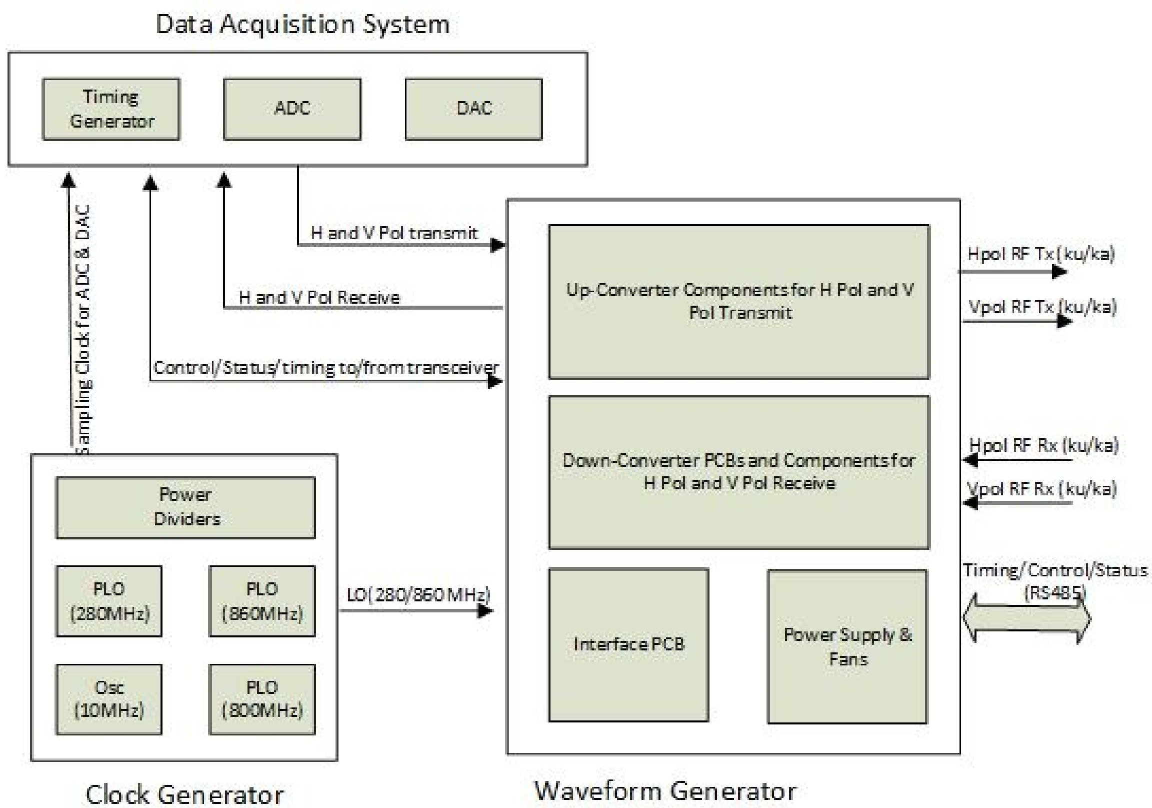

Figure 4.1: Design of IF stages for ku and ka band, showing the different sub-systems involved.

as the power at each stage is high and most of the components in the chain operate near to 3dB compression level.

After the gain and the mixing stages, we finally arrive at last IF stage on the horizontal and vertically polarized receiver channels, further digitized by the ADC digital module. The receive path uses amplifier with flat gain (over our region of interest) and low noise. The high inter-modulation products of the mixer are suppressed by filters in the receive chain and also finally the spectrum is cleaned up by an anti-aliasing filter before ADC sampling. It should be made sure that the spurious components do not leak through even after coherent integration. The components of the receive chain have high individual Third Order Intercept points (OIP3) such that the resultant OIP3 is high. This has aided us in achieving high SFDR for the receiver. The products with high OIP3 consume high power and require cooling, thus there is a tradeoff between power requirements and OIP3.

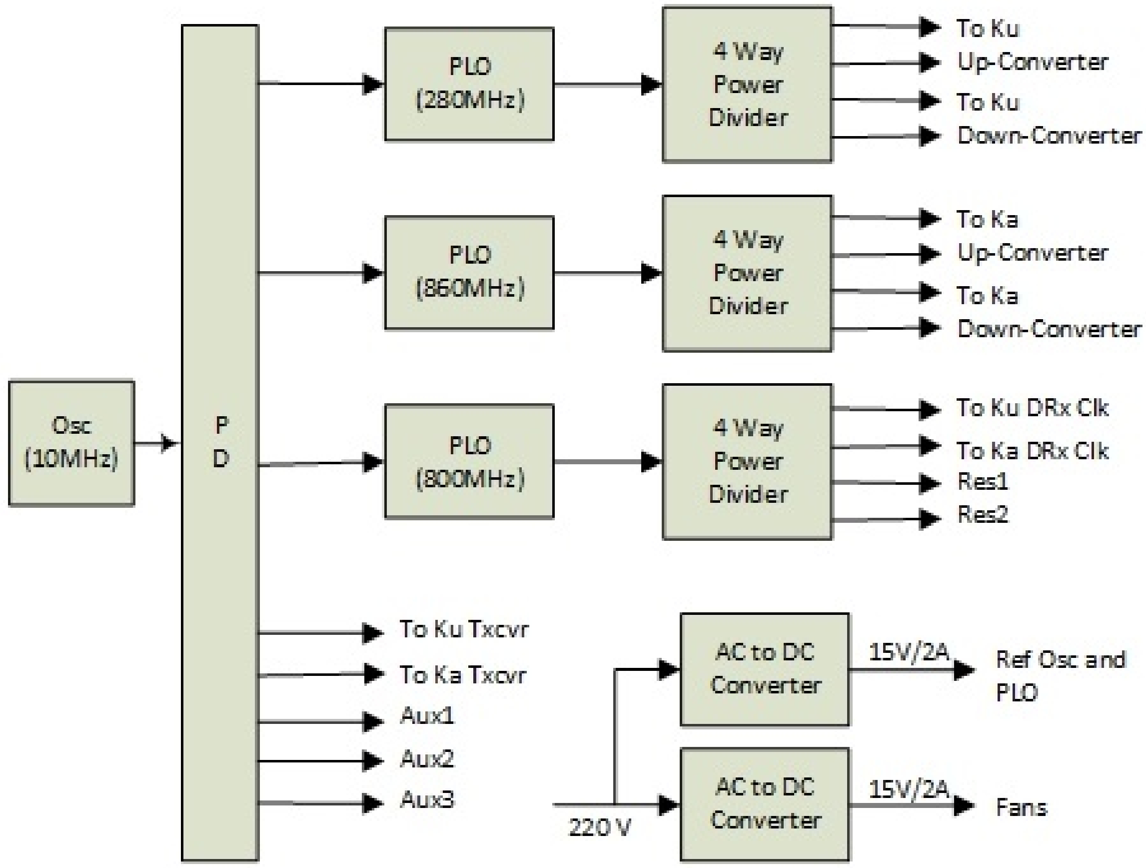

Figure 4.2: The basic block diagram showing synthesis of different IF frequencies and clocks for ku and ka sections.

Figure 4.1 shows the overall division of design and functionality in different sub-systems. These sub-systems were designed for ku and ka band with different frequencies at IF.

The IF frequency planning is accomplished after simulations and availability of synthesizer modules for those frequencies. Appropriate amplification or attenuation stages are added to meet the requirement of drive levels for the up and down converter stages. A basic block diagram expaining this, is in Figure 4.2. All of these components are part of the clock box.

4.2.1 Board Layout and Shielding Enclosures

The board layout is done keeping in mind the RF design and layout guidelines and appropriate shielding enclosures are used to curb EMI to/from these boards. We also designed a signal interface board to drive RS485 signals and receive them and convert to LVDS format, for the digitizer module. Transient suppressors were added to the 485 lines, which traverse long distances. 1pps signal and sync-in are the coaxial inputs to this board and sync out is the coaxial output, from this board. The sync in- sync out interface is provided so as to maintain synchronization between ku and ka systems.

4.2.2 Receive Gain

The receiver gain is calculated based on the highest strength signal strength expected from nearby strong scatterers which can be resolved, without saturating the ADC. In our case, for the calibration exercise, we mount a corner reflector, around 500 m away from the radar. This corner reflector is on top of a tall platform, to clear the sidelobe returns from ground, and for achieving a high enough SNR, for reflectivity calibration. This high received power from this corner reflector has to be adequately resolved, if we need to do the calibration exercise for receive and transmit calibration. For achieving this, not only ADC full scale should be sufficient to represent this power and not saturate but also, the intermediate amplifiers should be operating in a linear region as well. With the received power as reference, to ensure that none of the intermediate amplifiers were saturated, we had set up attenuators in between and thus, the appropriate gain for the IF stages was set. After the gain of the receivers were set up, we could also calculate the noise power seen by the ADC. The receive gain is apportioned into various stages, so that the power and cooling requirements of the amplifiers at different stages can be managed.

4.3 New Design Capability

The new design has coupled transmit waveform generator and digital receiver that would enable synchronous pulse-by-pulse change of transmit waveform and receiver filters. Also, flexible pulse-by-pulse frequency selection is possible. This flexible architecture enables new waveform sets to be developed, to meet science goals for sensitivity, range, velocity, etc. The longer mis-matched filters possible with new design, are capable of reducing peak sidelobe level (auto-correlation function for a non-zero delay). Hence it has the ability to mitigate the interference of strong scatterers over

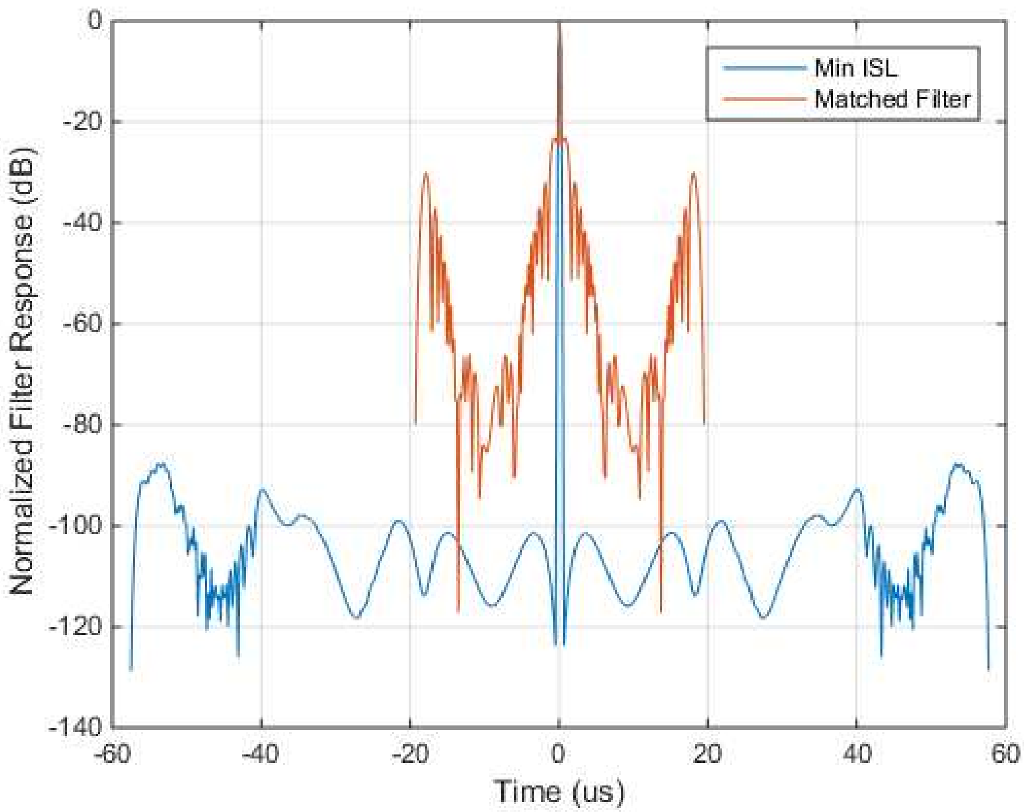

Figure 4.3: Comparison of peak sidelobe levels for matched filter and mis-matched filtering techniques for a chirp waveform.

adjoining range gates. It can be observed in Figure 5.6, that there is a significant improvement in peak sidelobe levels in case of length of filter is much greater than the length of sampled pulse waveform. The minimum integrated sidelobe (ISL) filter is generated with the use of mis-matched filtering techniques. For simulation, we used chirp with bandwidth = 5MHz, pulsewidth = 20 us and sampling rate = 5MHz.

An effective combination of inter-pulse (phase change on pulse to pulse basis) and intra-pulse (phase change on a sub-pulse basis) can lead to reconstruction of multiple trips and thereby lead to increase in pulse repitition frequency (PRF). An increase in PRF would lead to better velocity retrievals (less folding). With this, instantaneous measurement of scattering matrix by using simultaneous mode of operation can be accomplished. And lesser bias in measurements possible by reduction in cross-polar power. These techniques will be discussed at depth in later chapters.

4.3.1 Sensitivity Analysis

A highly sensitive system is able to detect intense reflectivity patterns as well as relatively weak precipitation echoes. A wideband pulse compression filter has a high range resolution but is less sensitive to weak echoes (due to relatively high noise power by opening up high receive bandwidth).

Reflectivity can be computed from receive power $\mathbf{P}_0$ by:

$$\mathbf{Z}_e = \mathbf{C}\mathbf{R}^2\mathbf{P}_0 \tag{4.1}$$

where, Radar Constant $\mathbf{C}$ is given by:

$$\mathbf{C} = \frac{1}{\Pi^5|K_w|^2}\frac{2}{c\tau}\frac{l_r}{g_r}\frac{4\Pi^3 l_{wg}^2}{P_t G_0^2}\frac{8ln(2)}{\Pi\phi_B\theta_B}\lambda \tag{4.2}$$

Equation 3 can also be written as [5]:

$$\mathbf{Z}_e[dBz] = P_0[dBm] + \mathbf{C}[dB] + 20logR[Km] \tag{4.3}$$

Minimum detectable reflectivity $\mathbf{Z}_e$, at a given range R is defined when the SNR is unity, ie, P_0 = kTB (B is the receiver equivalent noise bandwidth) or,

$$min\mathbf{Z}_e[dBz] = 10logkTB[dBm] + \mathbf{C}[dB] + 20logR[Km] \tag{4.4}$$

Thus the curve of minimum detectable reflectivity can be plotted as a function of range and mean noise power, after the pulse compression band-limiting has taken place.

Taking into consideration the current receive gain and the LNA noise power at receiver front-end, the noise power at the output of pulse compression filter is computed for Ku band by considering various time-bandwidth products (with constant T = 20μs). Later sensitivity curve is plotted by using equation 4.4. Corresponding to range resolution of 30m, a passband of 5MHz pulse com-

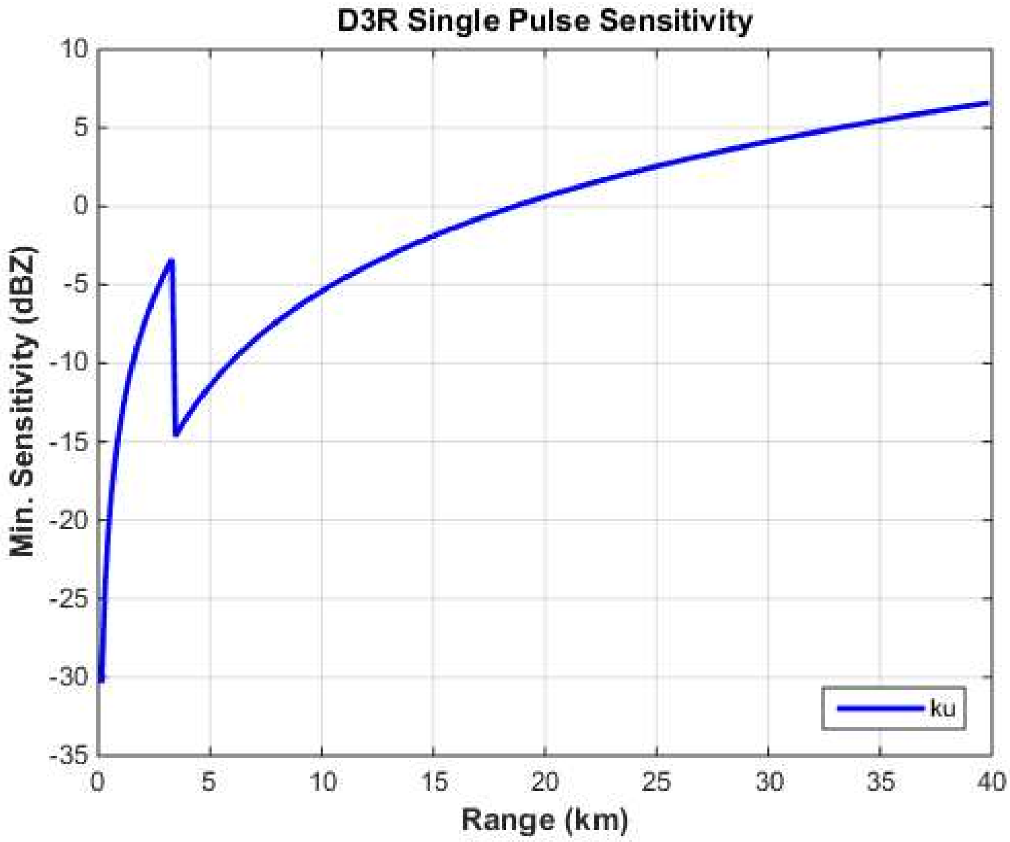

Figure 4.4: New System: Bandpass = 5MHz, Resolution = 30m

pression filter was synthesized and the sensitivity curve is shown in Figure 4.4. Also the previous system with a passband of 3.6MHz and 150m range resolution is shown in Figure 4.5. From the two figures, clearly the trade-off between range resolution, receiver bandwidth and sensitivity can be seen. Sensitivity suffers when we open up more receive bandwidth, but there is an improvement in resolution.

From these sections, it can be easily observed that a greater degree of programmability of the system is required to satisfy different trade-offs while observing various meteorological events. For example, for making observations for the evolution of cloud micro-physics prior to an event, we wish to have a higher sensitive system. A lower temporal resolution would not be a great concern here. However, if there is a big rain or snow event being captured, then we can compromise on sensitivity and instead have a high resolution data captured for the core of the storm, to observe and analyze it better. Therefore, there is a greater need of flexible and programmable weather

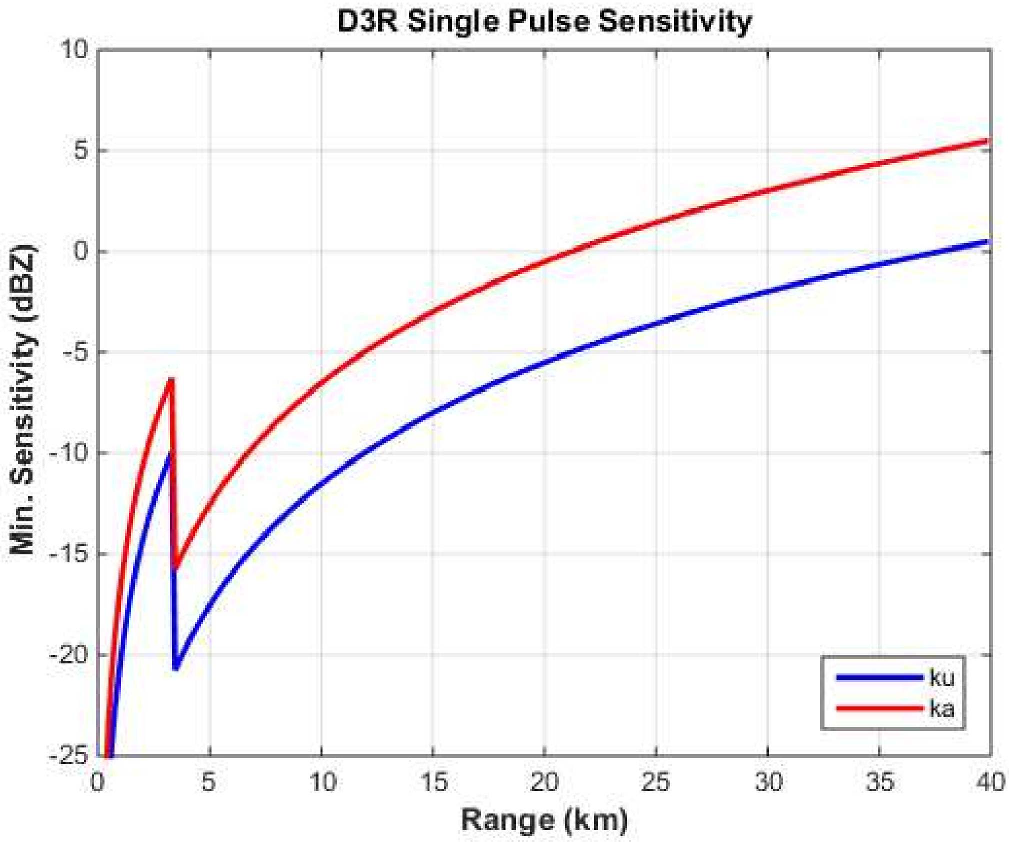

Figure 4.5: Previous System: Bandpass = 3.6MHz, Resolution = 150m

radar solution. The upgrade of D3R was meant to address these issues. The different fixed and programmable features in the radar after the upgrade is shown in figure 4.6.

The D3R after the hardware upgrade of IF electronics was deployed for the ICE-POP experiment in S.Korea. The goal of ICE-POP 2018 was to understand the winter precipitation regime with complex terrain and the associated processes with the focus of improving the short term forecasting and nowcasting systems. The experiment was supported by Korea Meterological Administration (KMA) and National Institute of Meterological Science (NIMS). The D3R, with its simultaneous operation in Ku and Ka band helped in understanding the winter precipitation by focusing on the micro-physical aspects of measurement, which was useful in forecasting of orographic snow during the PyeongChang Winter Olympics. Also, since the coastline of the ocean was very near, these observations also aided in understanding interactions between ocean and mountain regions and formation of the clouds and snow.

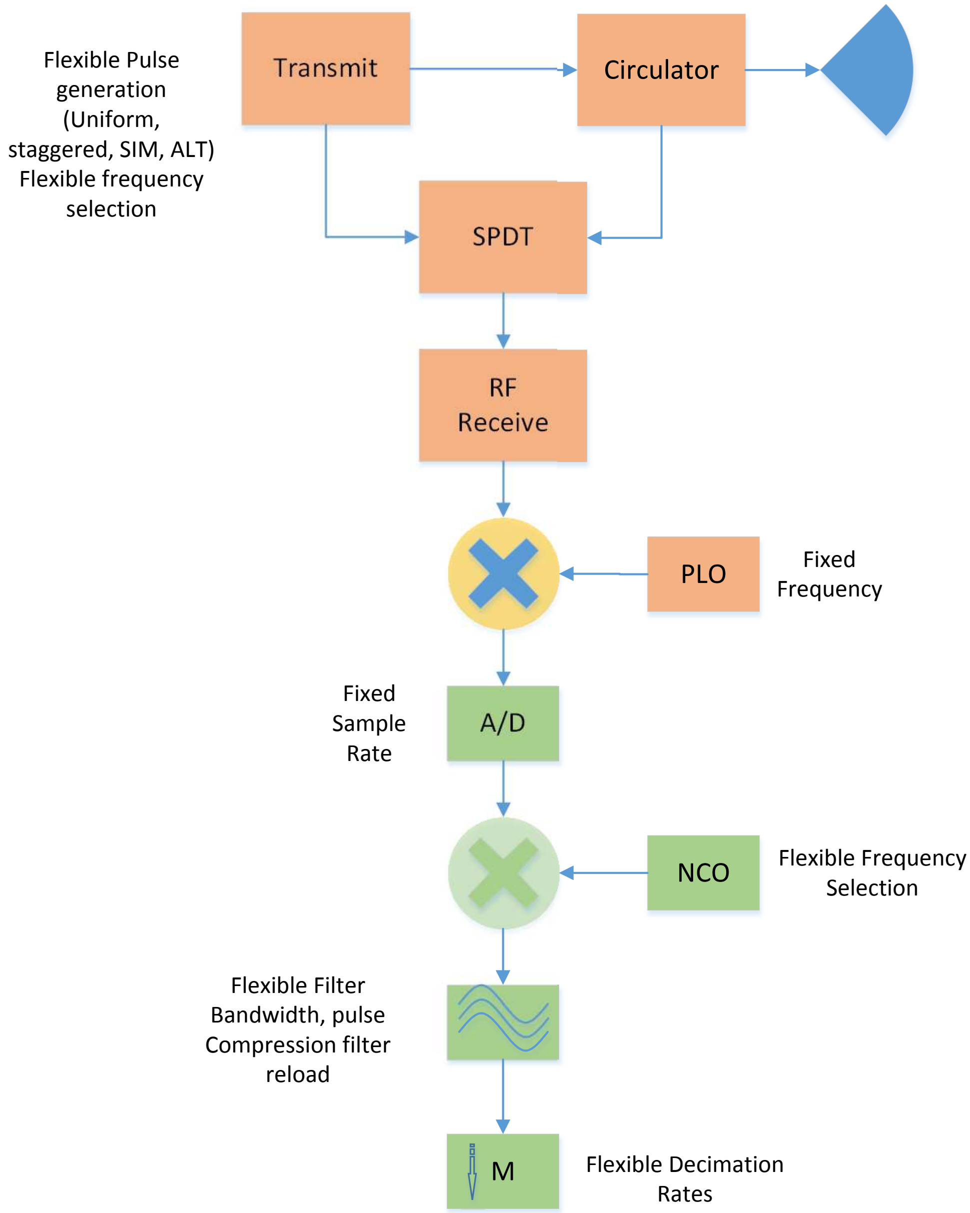

Figure 4.6: Different fixed and programmable features of the radar at various stages.

4.4 ICE-POP 2018 Experiment

The Olympic and the Paralympic games was hosted in two major clusters as PyeongChang mountain cluster and Gangneung coastal cluster. These clusters had various snow and ice venues.

The selection of these venues was made based on their avearge temperature in February and March and also based on the average precipitation over the past several years. In conclusion, these venues have had a high level of precipitation and low temperature which were ideal to hold the winter Olymics and Paralympic games [8]. The Gangneung Coastal cluster had a coastal climate and was a good place to understand the dynamics in snow precipitation between the interface of coastal region and mountainous region (PheongChang Cluster). The basic process includes the warm air with the heat and moisture supplied by the sea moving upwards over the mountain region forming snow clouds, induced by frictional differences between sea and land. The D3R observations aided in understanding of the evolution of these snow clouds through its dual polarization observations.

The D3R dual polarimetric measurements and their combination could also be used to characterize falling snow [2]. Multiple frequency observations, such as Ku and Ka band, are useful to study microphysical processes. Figure 4.7 shows the various sites hosting instruments in the campaign (marked in yellow pins), with the range of D3R highlighted by the circle. The other instruments at these sites were Parsivel disdrometer, Micro-Rain Radar (MRR), 2D Video Distrometers (2DVD) and X-band radars.

4.4.1 Performance of D3R

The NASA D3R which was previously stationed at Wallops flight facility (WFF) went through system upgrades until early 2017. Then the radar was calibrated using a corner reflector which was placed on top of a tower at a known distance. During the calibration process, the system parameters were adjusted to achieve optimal performance. This calibration event was done prior to shipping the radar to South Korea for the field campaign. The D3R was deployed in the DGW rooftop in late October 2017. This provided enough time for the radar to go through calibration process and also measure some rain events to make sure the system is working well before the actual Winter Olympics games started. The solar calibration was done to calibrate for the direction alignment with respect to the true north and check the co-alignment of ku and ka band antennas. The results of a solar calibration which ran on 4th December 2017 is shown in figure 4.8. From

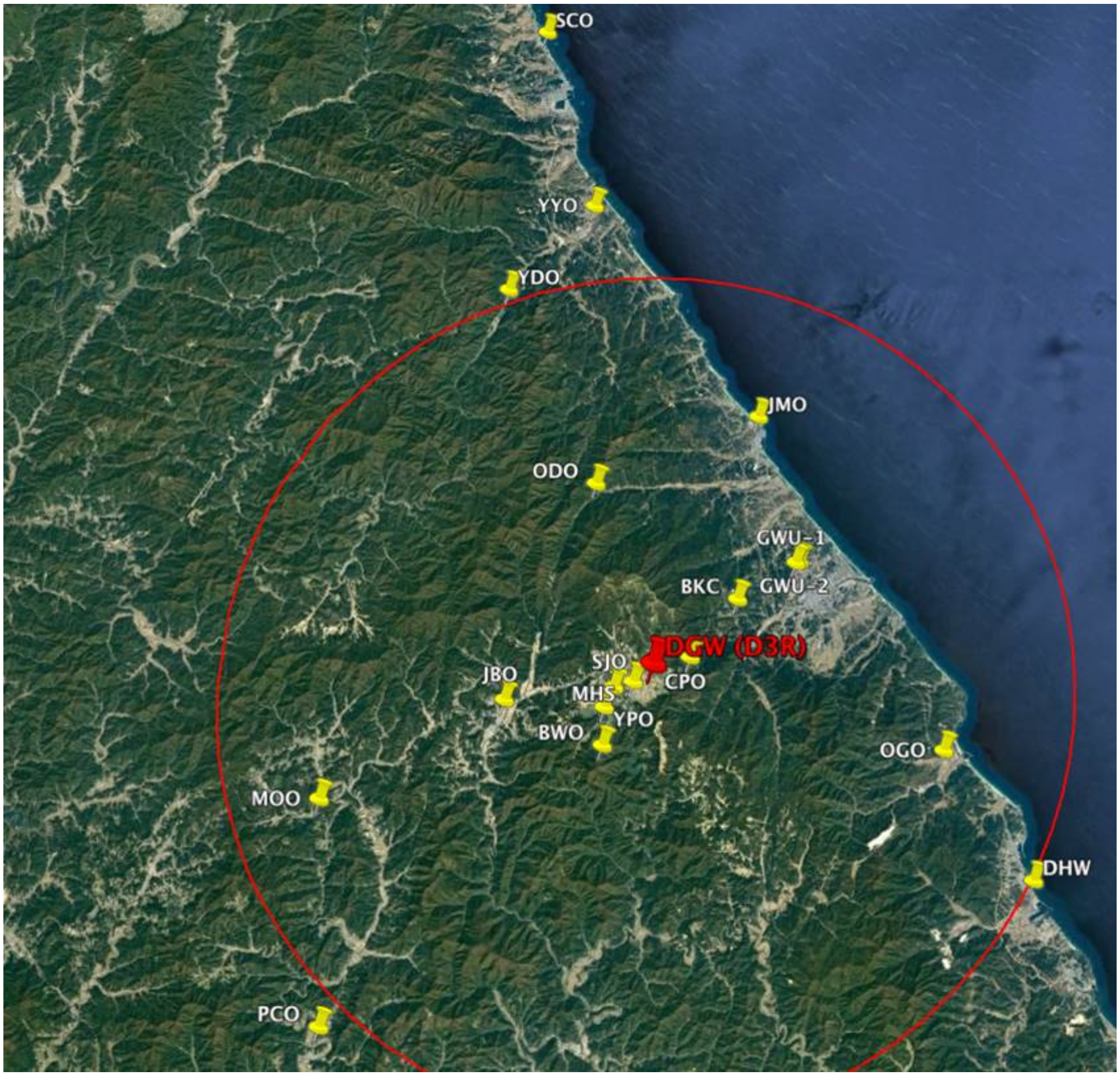

Figure 4.7: The sites which were involved in the ICEPOP 2018 campaign (equipped with instruments).

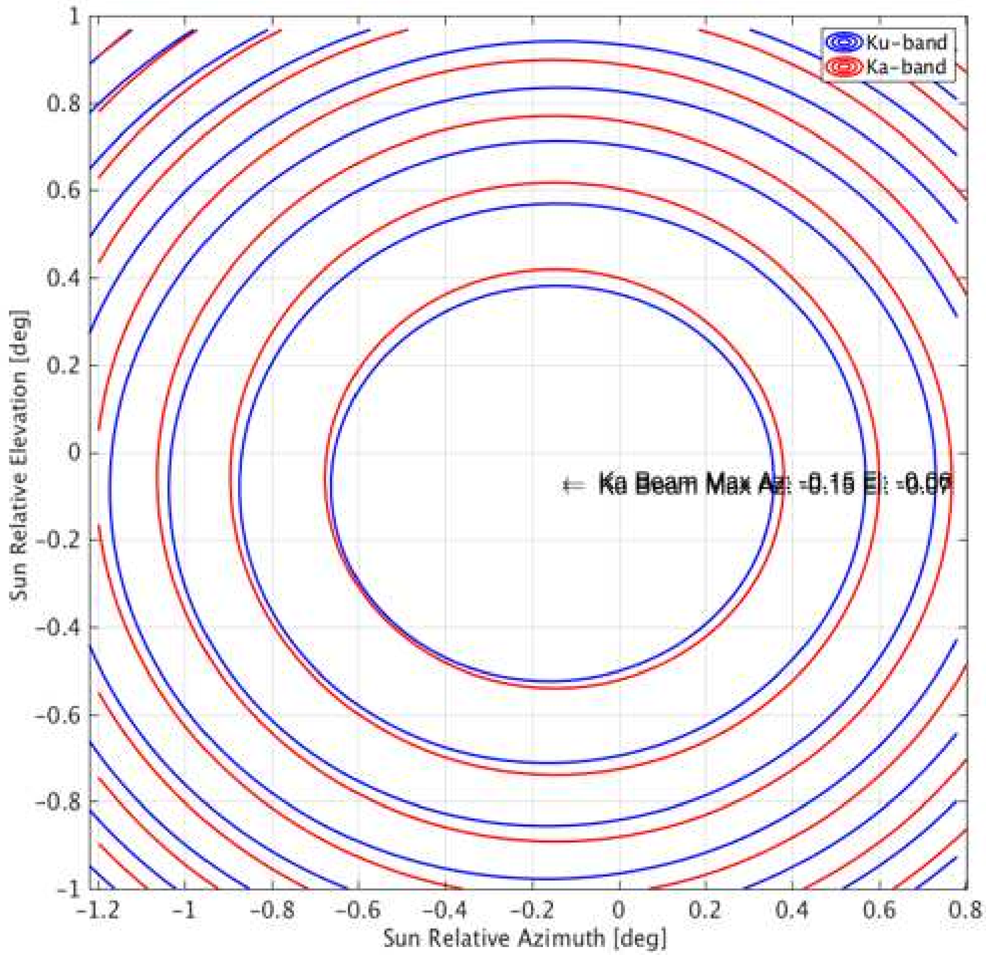

Figure 4.8: Result of solar calibration on 4th December 2017.

the solar calibration results, we can see that there is very good alignment of both antennas within $<0.1°$ elevation accuracy and $<0.15°$ azimuth accuracy respectively.

Deploying the radar early helped to capture some early winter snow events. D3R was scanning plan position indicator (PPI) and range height indicator (RHI) scans capturing various interesting precipitation cases due to the complex terrain. In the early part of the campaign, few rain events were captured and slowly it transitioned to snow events. There were heavy snow events in second half of February and early March, which was the time between the Olympics and Paralympics games.

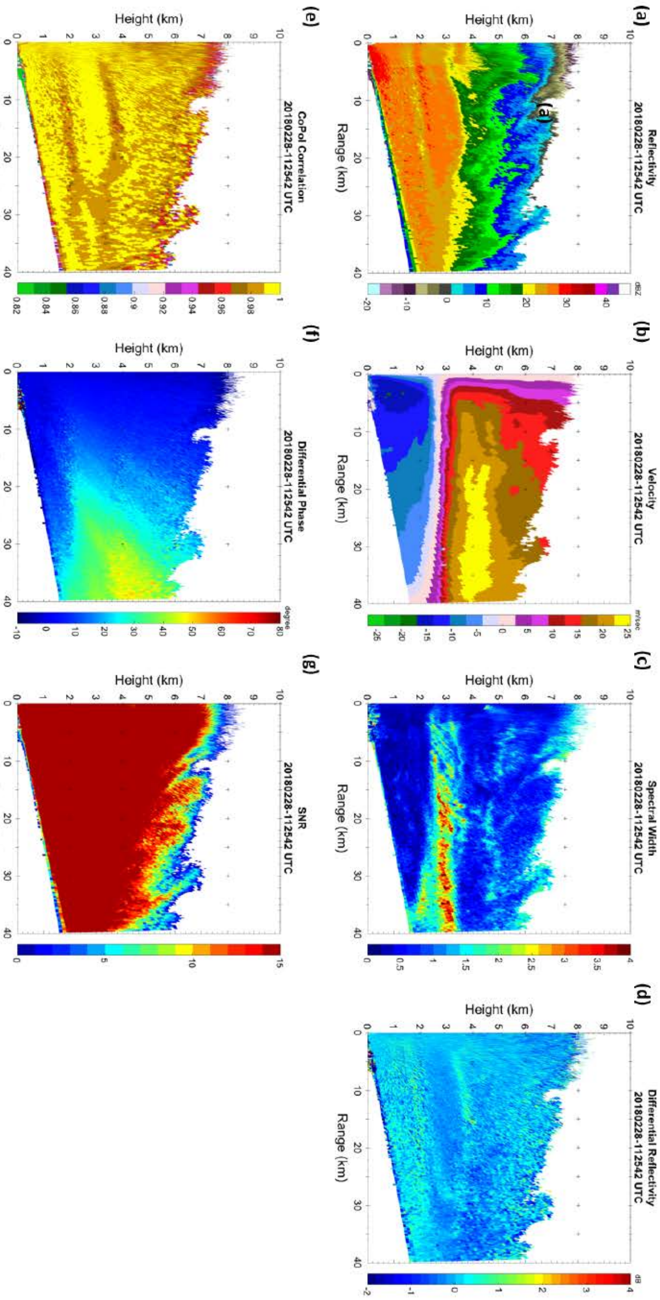

Figure 4.9: Various moment variables from the D3R for the 28th February case.

The D3R's Ku- band dual-polarization variables for the 28th Feb 2018 case is shown in the figure 4.9. The precipitation event occurred on this day was interesting because of the change in precipitation phases during the event from rain to freezing rain and snow. The snow event was also significant because of the fact that, a total of 41.2 cm of snow accumulated on that day. In the figure, we can see various dual-polarization variables from the D3R for a RHI scan. Going from top to bottom clockwise reflectivity, velocity, spectral width, differential reflectivity, dual frequency ratio, signal to noise ratio, differential phase and the co-polar correlation are shown. It can be observed that the storm is reaching till 6 km in height.

Chapter 5

Intra-Pulse Polyphase Coding System for Second Trip Suppression in a Weather Radar

5.1 Introduction

The use of phase codes to radars and communication has gained a lot of momentum recently because of the new computational approaches and more computing power available to search for long phase codes. There are more degrees of freedom for the design of a polyphase code than a binary code or chirp waveform. But the design complexity is generally higher, and many computational techniques can be used to obtain the desired properties for radar application ([26], [27] and [28]).

Many phase coding schemes exist in literature to retrieve weather radar products from the second, third and so on, trip echoes (after the unambiguous range). These codes can be broadly categorized into inter-pulse codes, which may be defined as a single phase offset per pulse (to the basic waveform). In this category, random phase codes and systematic phase codes, are popular to retrieve first and overlaid second trip ([29], [30] and many references within). The idea is to incorporate a random phase or a phase from Chu code sequence [31], per pulse, so that the second trip is whitened or gets modulated differently from the first trip or vice versa (depending upon the trip that is being retrieved). The suppression effect can be seen over the integration duration, comprising of many such pulses. Under the same category are Walsh-Hadamard codes, that have been shown in [32], to give a wide separation between co-polar and cross-polar returns (in simultaneous transmission of both polarizations). On the other hand, intra-pulse scheme rely on polyphase or binary codes within the pulse, to achieve the separation on account of its correlation properties. This orthogonality between intra-pulse polyphase codes has been used in this thesis for obtaining second trip suppression, if alternate pulses are coded with these codes from the orthogonal code set.

Additionally, the suppression abilities of second trip echoes in case of inter-pulse phase coding schemes (discussed in [29] and [30]), are dependent upon spectral width. This is because of filtering out second trip power amongst multiple replicas. Since there is no concept of using notch filters to suppress second trips in case of intra-pulse polyphase code, because this ability is inherent in the code, thus performance is not limited by multi-modal distributions or wider spectral width in general.

The properties that we would try to optimize for intra-pulse polyphase codes are the aperiodic auto-correlation for a given code, and the aperiodic cross-correlation between any pair of codes in the code set. Let us call this as an orthogonal set and begin with two polyphase codes $\{s_1(t), s_2(t)\}$, each of length L. For each time delay τ (time variable being t), this set should satisfy the following properties:

$$\int_t s_1(t)s_2^*(t+\tau)dt = 0, \tau = 0, 1, 2, ..., L-1, \tag{5.1}$$

$$\int_t s_l(t)s_l^*(t+\tau)dt = \begin{cases} 1, & \text{if } \tau = 0, l \in 1, 2. \\ 0, & \text{otherwise.} \end{cases} \tag{5.2}$$

It conveys that the correlation between two codes in the set is zero for all lags, and the auto-correlation is an impulse like function with unity response at zero lag and vanishes at all other lags. Such polyphase codes are very difficult to design and only optimal approximations can be achieved with pseudo-orthogonality. The optimization is carried out minimizing the cost function (also known as error function) derived from the above properties over the set of possible phase values, usually with gradient search. The orthogonality between codes manifests itself in their cross-correlation function and has been utilized in this thesis for suppression of second trip echoes, if alternate pulses have the same code. If more code-filter pairs could be synthesized, then suppression of other trip echoes can also be achieved.

The cost function (to be minimized) is the total energy in the sidelobes, better known as the integrated sidelobe level (ISL). In radar terminology, the aperiodic auto-correlation function is referred to as matched filtering. However, it is shown in [4], that the peak sidelobe level can be very effectively reduced using a mismatched filter which has a slight loss in signal to noise ratio (SNR), termed as mismatched filter loss. The correlation of code **a** with mismatched filter **b**, can be written as:

$$c_m = \Sigma_{i=1}^{L} a_i b_{i+m}^*, m \in (-L, L), \tag{5.3}$$

where L is length of mismatched filter (the code is zero padded to make it equal to the length L). Total sidelobe energy is defined as:

$$E = \Sigma_{m=-L+1}^{L-1} |c_m|^2, m \neq 0. \tag{5.4}$$

Because this energy function is non-convex mainly due to the unimodular constraint (constant modulus waveform), the local solvers would be driven towards local minima. Thus, the problem must be approached by driving multiple local solvers throughout the search space. We start by forming the energy (i.e., error) function for a mismatched-filter-based code to optimize auto-correlation sidelobe energy. Since the minimum ISL mismatched filter is known for a given polyphase code [34], we use that closed-form solution and iterate over different codes from the search space using local and global solvers, to obtain a code-filter pair with minimum ISL. A mismatched filter can optimally reduce the peak auto-correlation sidelobe, the same idea could be extended to include cross-correlation sidelobe energy as well. Therefore, we extend this strategy to the orthogonal code set, forming the error function comprising of auto-correlation sidelobe and cross-correlation sidelobe energy. For a given pair of polyphase code, the closed form of minimum ISL filter (mismatched) is derived and then we iterate over possible code filter pairs to find optimal solution. Thus we are trying to jointly optimize code and filters in this framework to find best polyphase codes satisfying the properties in equations 1 and 2.

Much of the literature published in the past deals with the design of polyphase code using a matched filter approach. This either requires a high pulse width or high bandwidth, to obtain a large number of samples essential for reasonable peak auto-correlation and cross-correlation sidelobes. An increase in pulse width would lead to more blind range. A high bandwidth requirement complicates the overall system design (RF, IF, filter design etc). Because of this, we formulated a mismatched-filter-based polyphase code pulse compression system, where the pulse width and bandwidth, can be maintained relatively small compared to the filter length. Further, lesser is the ratio of sampled pulse width to the filter length, there is likely improvement in peak sidelobe level. In D3R, pulse width is decided based on the total energy required to meet the sensitivity goal and lesser blind range. This type of joint formulation utilizing polyphase codes using mismatched filter to reduce auto-correlation and cross-correlation peak sidelobes for a weather radar is quite unique. Our approach is to estimate polyphase codes, using global optimization routines to arrive at a pair of polyphase codes with corresponding mismatched filters. And the criterion for optimal solution is to achieve a minimum of combined auto-and cross-correlation sidelobe energy. The idea behind the use of mismatched filter is since it is able to lower peak auto-correlation sidelobe, then it should be able to lower peak cross-correlation sidelobe as well (by spreading out sidelobe energy into a larger coefficient space). This idea has not been explored yet and is the novelty of this framework.

The gradient of the error function helps in the minimization process with speedy convergence, saving the solver with approximation using finite difference methods. When possible, this gradient can be set to zero to obtain a closed-form solution or it can be used iteratively in algorithms such as gradient descent, to find an optimal solution. In this thesis, we have derived the gradient of the error function based on mismatched filter (similar to [47]) so as to aid in convergence.

The performance of the synthesized code is analyzed through the use of ambiguity function, which has been modified for mismatched filter and also cross-ambiguity is introduced for orthogonal waveform set. The cross-ambiguity function quantifies the performance of cross-correlation between a pair of polyphase codes, over delay-doppler plane. The ambiguity function used here was restricted to the doppler experienced by weather scenarios. Both auto- and cross-ambiguity functions are very useful to evaluate the performance of the synthesized code.

The generated set of polyphase codes can be used for second trip suppression. Let's say, we design two polyphase sequences which are pseudo-orthogonal. The first and second trip echoes are coded with this sequence set. Then, the cross-correlation function between sequences in the set will give the separation of first and second trip echoes. The effectiveness of these codes, for second trip suppression will be demonstrated using simulation of weather echoes (of first and second trips) and later with D3R radar data (currently at CSU-CHILL radar site in Greeley, CO), on which this scheme has been realized.

5.2 Polyphase Code Design Problem

5.2.1 Matched-Filter-Based Orthogonal Polyphase Code:

The design, in this sub-section, is based on the assumption that the filter and samples in the transmit waveform are of the same length and matched to the code transmitted. Matched filter optimizes the signal to noise ratio of the target, with the Gaussian noise assumption, while the mismatched filter optimizes the signal to sidelobe ratio, with large lengths. There are number of papers ([28], [26]) which elaborate or optimize the correlation function. But the majority of them either use large pulse widths or higher bandwidth. The comparison of different codes and their correlation function is given in Fig. 5.1, 5.2, 5.3, based on Hadamard, Chu and Cyclic Algorithms (CA) respectively. These are all with a matched filter assumption.

The Hadamard codes are known for their orthogonal properties. These codes can be obtained by selecting a row of Hadamard Matrix $\mathbf{M}_L$, which is a $L \times L$ matrix. Each row of this matrix differs from other rows in exactly $L/2$ places. Additionally, $\mathbf{M}_L\mathbf{M}_L^t = L\mathbf{I}_L$, any two rows of this matrix are orthogonal at zero correlation lag, but we need to see the response at other lags as well, which is given in the Fig. 5.1. For this simulation, the Hadamard code was generated using the recursive formula:

$$\mathbf{M}_L = \begin{pmatrix} \mathbf{M}_{L/2} & \mathbf{M}_{L/2} \\ \mathbf{M}_{L/2} & \overline{\mathbf{M}_{L/2}} \end{pmatrix}, \tag{5.5}$$

where $\overline{\mathbf{M}_{L/2}}$ is the complement of $\mathbf{M}_{L/2}$. When $L = 2$, the Hadamard code is:

$$\mathbf{M}_2 = \begin{bmatrix} 1 & 1 \\ 1 & -1 \end{bmatrix}. \tag{5.6}$$

It is easy to observe from Fig. 5.1 that the correlation function value is non-zero for all lags and the peak sidelobe is around $20dB$ below the mainlobe.

Systematic Chu codes are of the type given by, $a = exp(j\boldsymbol{\psi})$ [31]. These are designed in such a way that the phase change on a sub-pulse basis should be:

$$\boldsymbol{\phi}_l = \boldsymbol{\psi}_{l-1} - \boldsymbol{\psi}_l = n\pi l^2/L; \qquad l = 0, ..., L-1. \tag{5.7}$$

The integer L is made equal to the number of samples, which forces the code to repeat through one or more full cycles in the sample sequence. Depending on the choice of n, the periodicity of the code is L or sub-multiples of L. For more details on the construction of these codes, the reader is referred to [30] and [31]. This Chu code has zero auto-correlation for all lags except 0 and multiples of L, and can be obtained by selecting n relatively prime to L. For demonstration, we select $n = 1$ and $L = 256$, so that there is one auto-correlation peak in the convolution integral of equation (5.1). The two Chu codes are obtained by selecting an overall length of 512 and then using one half of the sequence as one code (and the other half as the second code). If we plot the cross correlation function of these two codes (shown in Fig. 5.2), we can see that there is a deep null in the cross-correlation function at the place of auto-correlation peak. But to achieve this level of performance, the code length has to be large.

The polyphase orthogonal signal design can also be carried out using cyclic algorithms (CA) and CA-New (CAN) (introduced in [28]). In that paper, it is shown that to design good polyphase code waveform sets with good auto- and cross-correlation properties, we can minimize the following error function, shown to be equivalent to minimizing the sidelobe energy:

$$\varepsilon = ||\mathbf{R}_0 - L\mathbf{I}_M||^2 + 2\Sigma_{n=1}^{L-1}||\mathbf{R}_n||^2, \tag{5.8}$$

where $\mathbf{R}_n$ is the coded waveform covariance matrix at lag n, L is the length of the code and $\mathbf{I}_M$ is an identity matrix of size M. M signify the number of sequences in the code set. For our case, $M = 2$. This error function can be represented conveniently in the spectral domain, to form a computationally efficient algorithm called CAN. The correlation function obtained from two sequences generated with CAN algorithm (L = 256 samples) is shown in Fig. 5.3.

Another version of the CAN algorithm is the weighted CAN (WeCAN) [28], which aims at minimizing the following error function:

$$\varepsilon = \gamma_0^2||\mathbf{R}_0 - L\mathbf{I}_M||^2 + 2\Sigma_{n=1}^{L-1}\gamma_n^2||\mathbf{R}_n||^2, \tag{5.9}$$

where $\gamma_{n=0}^{L-1}$ are real-valued weights. These can put emphasis on the reduction of sidelobe power in certain regions of the waveform ambiguity function.

A very significant point to be noted from [28] is that the ε in both error functions of CAN and WeCAN, cannot be made arbitrarily small, even without the unit-modulus constraint on the absolute values of the code. But we can select a $P \leq (L + M)/2M$, which is a region around the mid-point on delay axis, of the correlation function. In that region P, it is possible to make ε very small. This is depicted in the simulation of CAN derived code-filter pairs (Fig. 5.3). These codes might be useful for applications like SAR imaging, where the transmit pulse lengths are large and we might be only interested in certain lags around the center of the correlation function. However, this performance is not enough for a weather radar applications, as the scatterers have a wide spatial and temporal distribution.

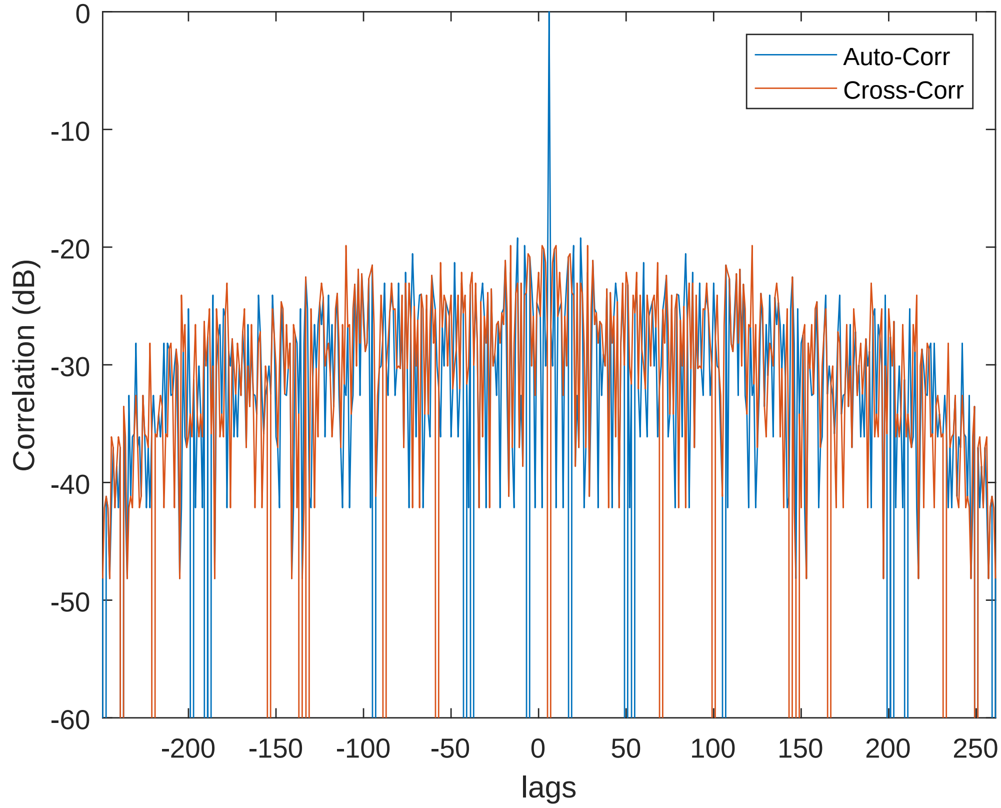

Figure 5.1: The correlation function (auto- and cross-correlations functions) with Hadamard codes obtained from the rows of the hadamard matrix. The code length and the filter length are both 256 samples.

5.2.2 Mismatched-Filter-Based Orthogonal Polyphase Code:

The motivation behind the use of mismatched-filter-based method is to have relatively larger filter lengths compared to the sequence length transmitted so that the peak sidelobe energy can be spread into much larger coefficient space. This approach has more flexibility as we can optimize the sequences and filters separately in an optimization framework, to obtain better sequences. We would start by design of optimal code-filter pair with regard to auto-correlation sidelobe energy (and later add cross-correlation sidelobe energy):

$$\mathbf{y}_{ij} = \mathbf{h}_j \mathbf{X}_i^m, \tag{5.10}$$

where $\mathbf{h}_j$ is the mismatched filter designed for the j^{th} sequence in the orthogonal code set and $\mathbf{X}_i^m$ is the modified transmit convolution matrix for the i^{th} sequence, obtained by deleting the columns

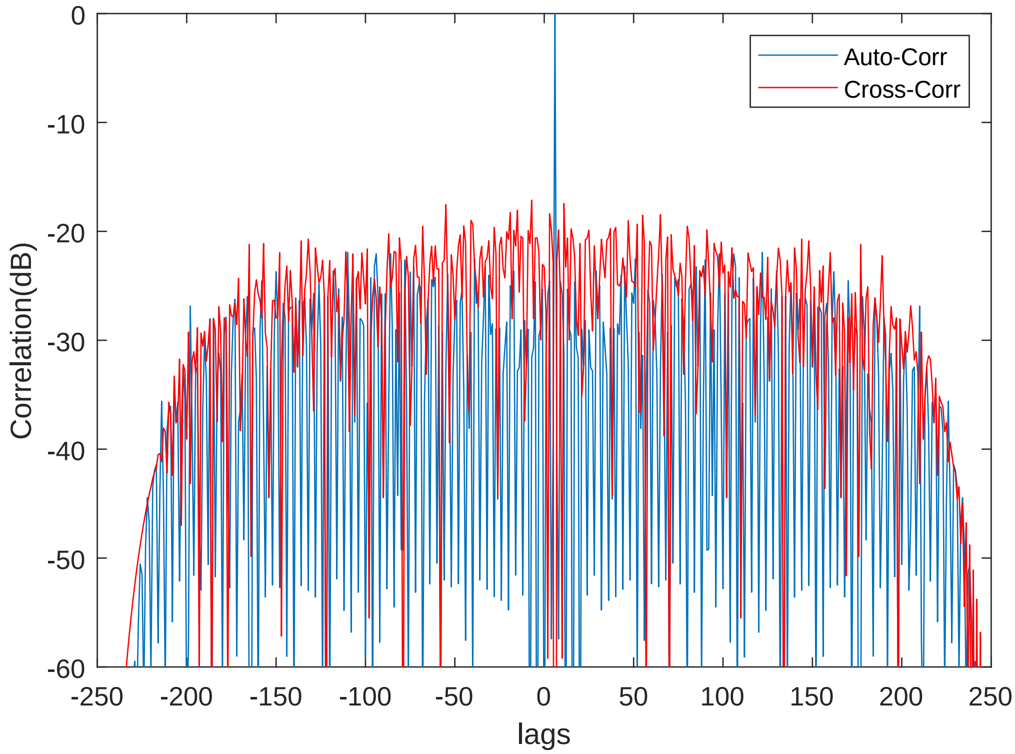

Figure 5.2: The auto- and cross-correlation functions with Chu codes.

of transmit convolution matrix that corresponds to the mainlobe after convolution operation. The error function corresponding to the energy in auto-correlation sidelobes can be written as:

$$\varepsilon_{hi} = \mathbf{h}_i^t \mathbf{X}_i^m \mathbf{X}_i^{mH} \mathbf{h}_i^*. \tag{5.11}$$

With the constraint of $\mathbf{x}_i^t \mathbf{h}_i = L$, $\mathbf{x}_i$ being the i^{th} sequence of the orthogonal code set and L is the length of code, the error function has got a minimum at [34]:

$$\mathbf{h}_i^t = (\mathbf{X}_i^m \mathbf{X}_i^{mH})^{-1} \mathbf{x}_i L / \mathbf{x}_i^H (\mathbf{X}_i^m \mathbf{X}_i^{mH})^{-1} \mathbf{x}_i. \tag{5.12}$$

If the polyphase code-filter pairs to be optimized for both auto- and cross-correlation energy (using mismatched filter), then the error function gets modified as:

$$\varepsilon_{hi} = \mathbf{h}_i^t \Sigma_{i=1}^M (\mathbf{X}_i^m \mathbf{X}_i^{mH}) \mathbf{h}_i^*, \tag{5.13}$$

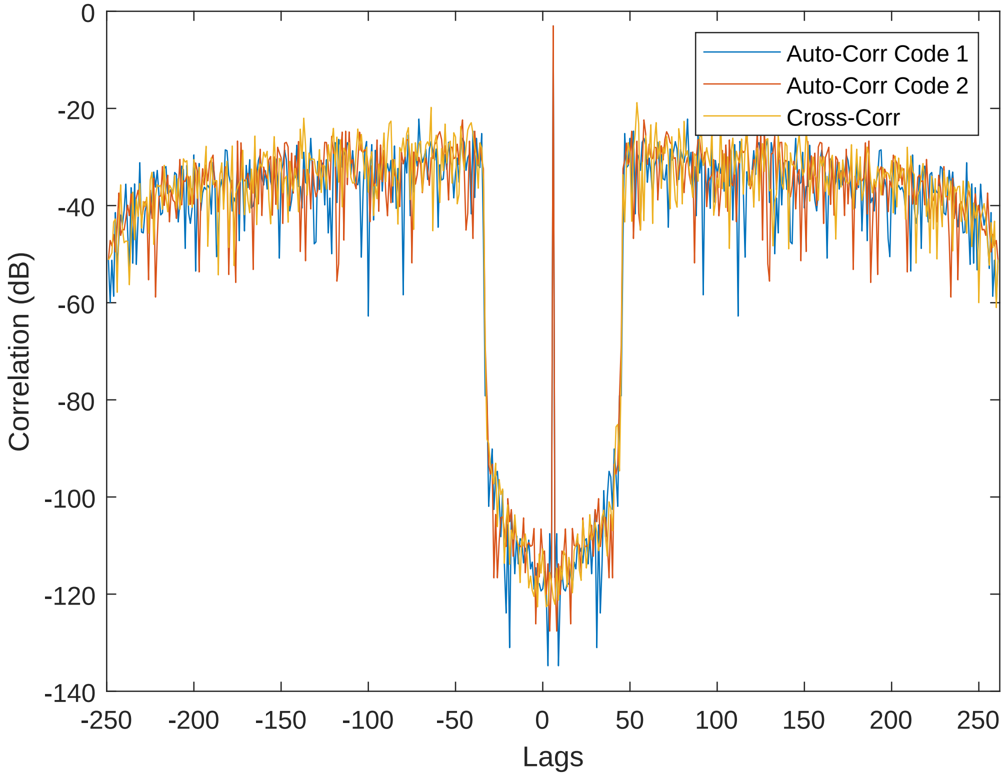

Figure 5.3: The correlation function with CAN based codes. Here the orthogonal sequence set comprises of {code1, code2}.

where M is the number of codes in the orthogonal set and the optimum filter weights would be:

$$\mathbf{h}_i^t = (\Sigma_{i=1}^M(\mathbf{X}_i^m\mathbf{X}_i^{mH})^{-1}\mathbf{x}_i L/\mathbf{x}_i^H(\Sigma_{i=1}^M(\mathbf{X}_i^m\mathbf{X}_i^{mH}))^{-1}\mathbf{x}_i. \tag{5.14}$$

This is the well-known closed form expression for the minimization vector:

$$\mathbf{h}_i^t = (\Sigma_{i=1}^M(\mathbf{X}_i^m\mathbf{X}_i^{mH}))^{-1}\mathbf{x}_i, \tag{5.15}$$

and the denominator part of equation (5.14) is for normalization.

Our method starts with a set of two codes, randomly generated. For simulation, we took $L = 40$ for a pulse width of $20\mu s$ and bandwidth of 2 MHz. The filters based on equation (5.16) were generated (optimal in ISL of the auto- and cross-correlation sidelobes). After we have obtained a set of initial codes and filters, then we iterate over the permissible code combinations and simultaneously trying to find minima for the error function in equation (5.14) using optimization methods. In the next iteration, when a new code is found, again we get ISL filter using equation (5.16) and the error function is evaluated. This continues until we reach at least a local minima. The mainlobe width is assumed to be 5 samples. This method jointly optimizes the polyphase codes and filters. Subsequently, global optimization forces the local solvers to run from various initial points in the search space, which are obtained using the scatter search. More details in 5.2.3 about setting up the optimization process.

It is easy to realize that it is difficult to obtain very low levels of auto-correlation and cross-correlation of sequences. In reality, there are bounds on how low the correlation sidelobes can be simultaneously achieved. Initially, it was explored by Dr. Sarwate in [36] and Welch in [37]. Moreover, the potential application of sequences with good correlation properties is immense, for example, in a multiple-input multiple-output (MIMO) radar [38], communication, etc. When we employ orthogonal signals for transmitting in a MIMO radar, there is a significant improvement in detection performance due to spatial diversity. Also, these codes can significantly improve the bandwidth efficiency of a code-division multiple-access (CDMA) based system in addition to enhancing the interference-free operation [40]. In the weather radar community, such codes can potentially lead to instantaneous measurement of scattering matrix parameters [39]. Another class of polyphase codes that try to achieve orthogonality of sequences is complete complementary codes (CCC). They are generalizations of space-time block codes and Golay complementary codes, developed to explore polarization diversity. Golay pairs have zero auto-correlation sidelobes if the autocorrelation function of the pair is added together, which essentially means that the pair has complementary sidelobes. Additionally, CCC's have the property that its cross-correlation sidelobes also vanishes for the sum of cross-correlations of the pairs in the set. A very general definition of CCC is given in [41]. Much finer details about their construction methods and making these codes doppler tolerant are given in [42] - [45].

Another point to be noted here is that, for example, in D3R radar, the number of mismatched filter coefficients is fixed (based on resources) but the pulse width might vary, for example, for a 1MHz bandwidth, we have $20\mu s$ or $40\mu s$ pulse width. However, since the ratio of the number of waveform coefficients to the number of filter coefficients (WF2FC) has become twice (in case of $40\mu s$ pulse width), we have observed peak sidelobe levels degrading by as much as 10 dBs. The worst case peak sidelobe levels are obtained when the number of waveform coefficients becomes equal to the number of filter coefficients, which is a case of matched filter design. Additionally, if the bandwidth increases, even with the same pulse width, the number of waveform coefficients would increase and the ratio of WF2FC would increase as well, having an adverse impact on the peak sidelobe ratios. Thus this technique works best when the WF2FC ratio is small (0.042 for D3R operating at 1MHz bandwidth and $20\mu s$ pulse width).

5.2.3 Setting up the Optimization Problem

The goal of the optimization problem is defined by the objective function, $g(x)$, and a set of constraints on the variables, which define the limits of acceptable space for these variables. The standard problem is defined by:

$$\begin{aligned} & min_x g(x) \\ & s.t. E_i(x) = 0, i = 1, ..., m \\ & I_j(x) \leqslant 0, j = 1, ..., n \\ & \mathbf{x}_l \leqslant \mathbf{x} \leqslant \mathbf{x}_u, \end{aligned} \tag{5.16}$$

where E_i and and I_i are equality and inequality constraints for **x**. The last statement tells us about the lower and upper bounds on **x**. A global optimizer is the one that finds $\mathbf{x}_{min}$ from the full feasible set. In case, either the objective function or the constraints are non-linear then such a problem can be shown to have first-order optimal solution, if it satisfies the Karush Kuhn Tucker (KKT) conditions [55], through the use of Lagrange's multipliers. These are necessary to combine the objective function and the constraints and they scale the gradients to fulfill the condition. The optimization problem of minimal sidelobe energy in equation (5.14) is a non-linear function with non-convex unit modulus constraint, which defines the $g(x)$ and $E_i(x)$ of equation (5.16). The inequality constraints and the bounds on x are defined in section 5.2.4. Hence the combined objective function satisfying the KKT conditions will be non-convex and non-linear having multiple local minima. For such a case, we need to run global optimization routines to find an optimal solution. As the pulse width or the bandwidth increases, we would have more variables to optimize with each variable able to take valid values between $[0, 2\pi]$. It can be observed that the search space is huge and the global minima will be difficult to obtain with direct search methods. Hence the use of gradient-based method.

The gradient-based method requires that the objective function, constraints, and gradients be continuous. We have used Sequential Quadratic Programming (SQP) and Active set based gradient search. These methods transform the given problem to a set of sub-problems that may be easier to solve. These are likely to converge to a local minima for a non-convex non-linear constraint problem and require gradient and Hessian. The gradient, if not supplied, is approximated using finite difference method and the Hessian is usually computed at each iteration using a quasi-Newton method called Broydon-Fletcher-Goldfarb-Shanno (BFGS) [54].

Both multi-start or global search can be used along with a local solver over the whole of search space, for our non-convex non-linear problem and constraint to obtain a global minima. Multi-start runs the local optimizer from multiple feasible start points. Individual runs can be in parallel. It starts with uniformly distributed start points within the domain. Global search, however, starts with initial point x_0 and a set of potential starting points using scatter search [52]. Since global search analyzes start points and reject those points that are not likely to improve upon the best minima, it is faster and more logical to work with. In section 5.2.5, we derive the gradient of the error function so that local search can likely converge faster.

The computational search solvers have been studied extensively like the use of exhaustive search, evolutionary algorithms and heuristic search, for the design of polyphase codes or sequences. They can all be used to optimize the local search around an initial point. The exhaustive search complexity is $O(2^n)$ for binary sequences of length n and it can be reduced to $O(1.85^n)$ by using branch and bound [35]. However, this complexity would increase further with the number of symbols in the polyphase sequence hence heuristics methods such as [48] should be used for large sequences. The evolutionary methods such as genetic algorithms are likely to fail because the generation step creates candidates by mutation or crossover. But a linear combination of two good sequences will not necessarily provide a sequence that has better correlation properties. The cyclic algorithm named CAN, introduced in [28], provides sequences of larger lengths but instead of the original ISL cost function, it tries to minimize another simpler criterion which is shown to be equivalent to ISL. However, it needs to be modified to take our framework of mismatched filter (CAN based algorithms are derived with the matched filter approach). Even the majorization-minimization (MM) method in [27], which works directly with the ISL cost function has to be modified significantly for use with mismatched filter.

5.2.4 Constraints

We already mentioned the uni-modular constraint on the optimization problem. This is important for the transmit section which might need to operate in saturation mode. Moreover with the use of a mismatched filter, an overall constraint on the gain and phase terms of the combined code-filter pair has to be incorporated. Apart from this, there is also a need for another constraint that the gain and phase terms of code-filter pair 1 be equal to gain and phase terms of code-filter pair 2. These pairs were obtained using the joint optimization procedure described in section 5.2.3. This would ensure that for the velocity retrieval, the phase imbalance of odd and even pulses, do not give rise to additional spurious velocity components. The gain balance between these pairs would aid in reflectivity calibration.

5.2.5 Derivative of the Error/Energy function

Let us look first, at the gradient of autocorrelation sidelobe energy (or the error function). If **a** is the polyphase sequence with unit magnitude constraint, then

$$c_m = \Sigma_{i=1}^{N} a_i a_{i+m}^*, m \in (-N, N). \tag{5.17}$$

With the weighing and exponential term in the error function, as used in [47]:

$$\varepsilon = 2\Sigma_{m=1}^{N} w_m (c_m c_m^*)^p. \tag{5.18}$$

It turns out that the partial derivative of the error function w.r.t. α, which is the phase angle of **a**, comes out to be [47]:

$$\delta = \frac{\partial \varepsilon}{\partial \alpha} = 4p\Im(\mathbf{a} \circ ((\boldsymbol{\beta} \circ \mathbf{c}) * \mathbf{a})), \tag{5.19}$$

where $\beta_m = w_m (c_m c_m^*)^{p-1}$ and $x \circ y$ is the Hadamard product of x and y.

Next for our application, we expand this derivative for a mismatched filter case and we begin with:

$$c_m = \Sigma_{i=1}^{N} a_i b_{i+m}^*, m \in (-N, N), \tag{5.20}$$

where **b** contains the filter coefficients and N is its length. After forming the error function as per equation (5.18) and taking its derivative w.r.t. real part of **a**, we get,

$$\begin{aligned}
\frac{\partial \varepsilon}{\partial \Re(a_j)} &= 2p\Sigma_{m=-N+1}^{N-1} \beta_m [\Re(c_m) \frac{\partial \Re(c_m)}{\partial \Re(a_j)} + \Im(c_m) \frac{\partial \Im(c_m)}{\partial \Re(a_j)}] \\
\Re(c_m) &= \Re(\Sigma_{i=1}^{N} a_i b_{i+m}^*) \\
&= \Sigma_{i=1}^{N} [\Re(a_i)\Re(b_{i+m}) + \Im(a_i)\Im(b_{i+m})] \\
\Im(c_m) &= \Sigma_{i=1}^{N} [-\Re(a_i)\Im(b_{i+m}) + \Im(a_i)\Re(b_{i+m})].
\end{aligned} \tag{5.21}$$

The partial derivatives are zero unless $i = j$, so that,

$$\begin{aligned}
\frac{\partial \Re(c_m)}{\partial \Re(a_j)} &= \Re(b_{j+m}) \\
\frac{\partial \Im(c_m)}{\partial \Re(a_j)} &= -\Im(b_{j+m}).
\end{aligned} \tag{5.22}$$

Thus, we can write,

$$\frac{\partial \varepsilon}{\partial \Re(a_j)} = 2p\Sigma_{m=-N+1}^{N-1}\beta_m[\Re(c_m)\Re(b_{j+m}) - \Im(c_m)\Im(b_{j+m})]. \tag{5.23}$$

Similarly, we can write,

$$\frac{\partial \varepsilon}{\partial \Im(a_j)} = 2p\Sigma_{m=-N+1}^{N-1}\beta_m[\Re(c_m)\Im(b_{j+m}) - \Im(c_m)\Re(b_{j+m})]. \tag{5.24}$$

Let α be the phase angle of **a**, then using the chain rule we get,

$$\frac{\partial \varepsilon}{\partial \alpha_j} = \Re(a_j)\frac{\partial E}{\partial \Im(a_j)} - \Im(a_j)\frac{\partial E}{\partial \Re(a_j)}. \tag{5.25}$$

Using equations above, we get,

$$\begin{aligned}\frac{\partial \varepsilon}{\partial \alpha_j} &= 2p\Sigma_{m=-N+1}^{N-1}\beta_m[\Re(c_m)\Im(b_{j+m})\Re(a_j) \\ &- \Im(c_m)\Re(b_{j+m})\Re(a_j) - \Re(c_m)\Re(b_{j+m})\Im(a_j) \\ &+ \Im(c_m)\Im(b_{j+m})\Im(a_j)].\end{aligned} \tag{5.26}$$

This derivative of the error function, is a guiding direction in the local search under framework of codes and mismatched filters.

5.2.6 Ambiguity Function for mismatched filters

The ambiguity function for a mismatched filter represents the effect of delay and doppler on sidelobes and mainlobe, on a code-filter pair. In general, ambiguity functions are good tools to analyze the performance of synthesized polyphase codes for doppler tolerance in a weather sensing application. In any case, the ambiguity function at $(\tau, f_d) = (0, 0)$ corresponds to a matched output to the signal reflected perfectly from the target of interest. The ambiguity function $|\chi(\tau, f_d)|$ for a polyphase code **a** and mismatched filter **b**, can be written as:

$$|\chi(\tau, f_d)| = |\Sigma_{n=-N+1}^{N-1}a(n)b(n+\tau)exp(j2\pi f_d n)|. \tag{5.27}$$

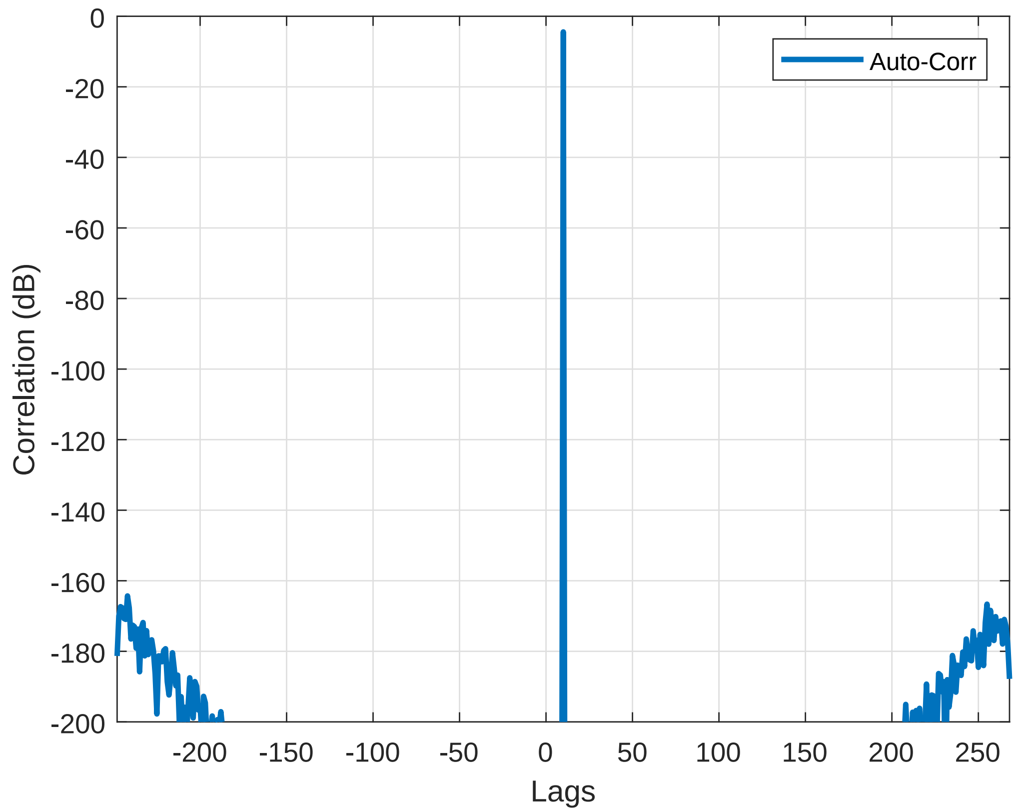

Figure 5.4: The zero doppler cut of the synthesized polyphase code of length 40 with uni-modular constraint (from auto-ambiguity function).

In plots, we would be showing only the positive Doppler shifts as the ambiguity function is symmetric around zero. We start with ambiguity functions achieved with optimization carried out for auto-correlation sidelobe energy, as the error function (using mismatched ISL filters).

Fig. 5.4 and 5.5 show the zero-doppler cut (from ambiguity function) of a polyphase code and filter with uni-modular constraint (synthesized with only auto-correlation sidelobe energy error function with global search). It used mismatched filter length of 480 coefficients. The zero Doppler cut has very low sidelobes in the whole domain with a one-sample mainlobe. The doppler performance of the code is also good under reasonable doppler assumption (peak sidelobe level below -150dB). The sidelobes are practically zero throughout the correlation space for zero doppler condition. Such level of sidelobe performance is far superior to the matched filter counterparts and even for Chirp based mismatched filters. Both matched filter and mismatched filter sidelobe

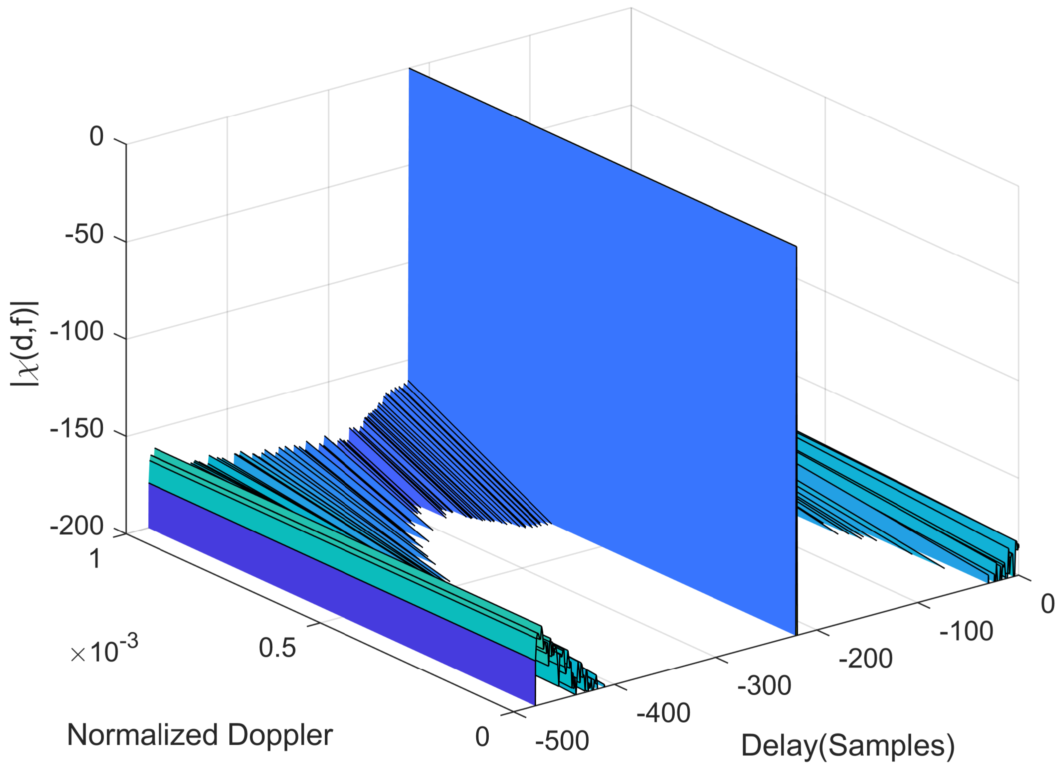

Figure 5.5: Auto-ambiguity Function of polyphase code with length 40 samples (PW = $20\mu s$, BW = 2MHz) and the mismatched filter length of 480 samples.

level for a Chirp based waveform is depicted in Fig. 5.6. The peak sidelobe level for a Chirp based mismatched filter is $\sim -85dBc$ (the dBc units used here is the relative power of the peak sidelobes with respect to the carrier power normalized to 0 dBm). However, the polyphase based optimization yields peak sidelobe performance better than $-180dBc$.

The Auto-ambiguity and the Cross-ambiguity functions, are defined next, in the context of our framework. Let the orthogonal code set comprise of two polyphase codes, $\{\mathbf{a}_1, \mathbf{a}_2\} \in \mathbb{C}$ and the corresponding ISL filters be $\{\mathbf{b}_1, \mathbf{b}_2\} \in \mathbb{C}$. These sets are obtained minimization of auto-correlation sidelobe energy in $\{\mathbf{a}_1 * \mathbf{b}_1 + \mathbf{a}_2 * \mathbf{b}_2\}$ and cross-correlation sidelobe energy in $\{\mathbf{a}_1 * \mathbf{b}_2 + \mathbf{a}_2 * \mathbf{b}_1\}$. Under these assumptions, the auto-ambiguity function is defined as:

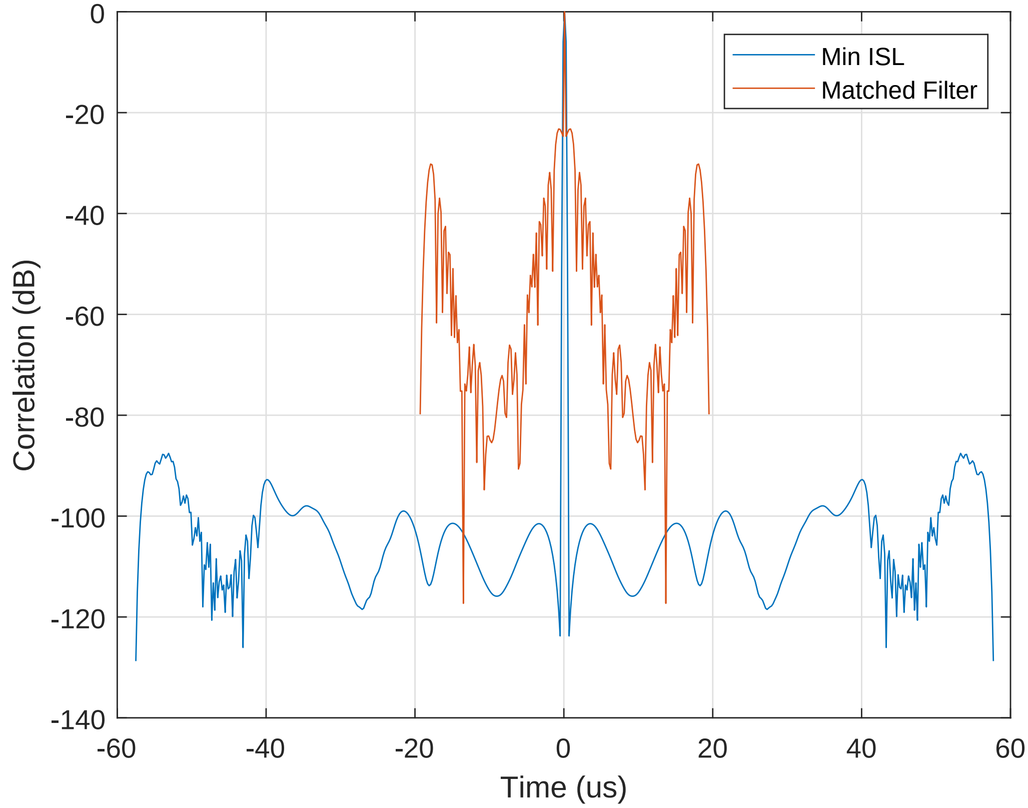

Figure 5.6: A comparison of peak sidelobe levels for a matched and mismatched-filter-based on Chirp waveform. Blue depicts mismatched filter designed with minimum ISL criterion

$$|\chi_{1auto}(\tau, f_d)| = |\Sigma_{n=-N+1}^{N-1} a_1(n) b_1(n+\tau) exp(j2\pi f_d n)|,$$
$$|\chi_{2auto}(\tau, f_d)| = |\Sigma_{n=-N+1}^{N-1} a_2(n) b_2(n+\tau) exp(j2\pi f_d n)|. \tag{5.28}$$

whereas the cross-ambiguity function is defined as:

$$|\chi_{1cross}(\tau, f_d)| = |\Sigma_{n=-N+1}^{N-1} a_1(n) b_2(n+\tau) exp(j2\pi f_d n)|,$$
$$|\chi_{2cross}(\tau, f_d)| = |\Sigma_{n=-N+1}^{N-1} a_2(n) b_1(n+\tau) exp(j2\pi f_d n)|. \tag{5.29}$$

Let us see the physical realization of these with the help of ambiguity function plots for a pair of orthogonal polyphase codes and mismatched filters synthesized with global search. The advantages of global search were discussed in section 5.2.3 along with scatter search algorithm (to obtain good initial points for the local search). This is used here to come up with code-filter pairs. The

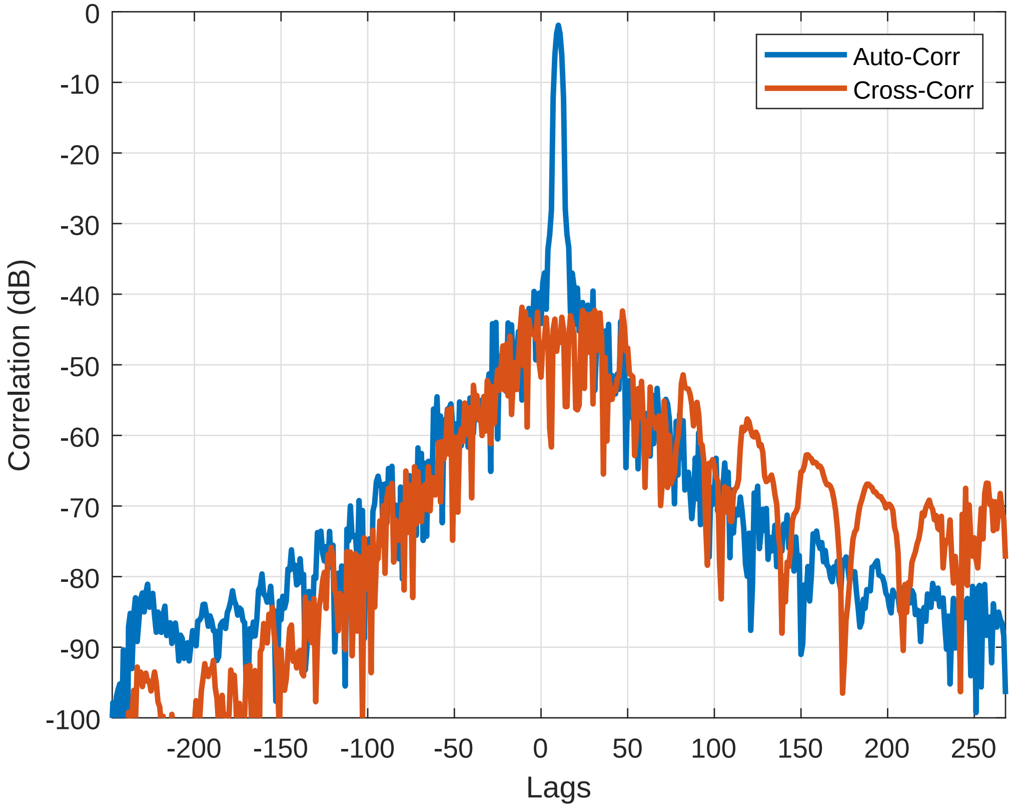

Figure 5.7: The zero doppler cut of the ambiguity function for the auto-correlation $\{\mathbf{a}_1 * \mathbf{b}_1\}$ and cross-correlation $\{\mathbf{a}_1 * \mathbf{b}_2\}$. The mainlobe width is set to 5.

error/cost function used is equation (5.13) along with the constraints in section 5.2.4. Additionally, the derivative of error function in section 5.2.5 is used to aid the optimization process. Finally, two code-filter pairs were obtained and their auto- and cross-correlation functions are depicted in Fig. 5.7 (zero-doppler cut). Fig. 5.8 and 5.9 gives the effect of moderate doppler frequencies on these code-filter pairs.

It can be easily observed from these plots that both the peak auto- and cross-correlation sidelobe levels are better than $-40dBc$, and in general, they are better than $-70dBc$ for half of the correlation space. This level of performance has not been demonstrated before, even for large code lengths and it can suppress the second trip echoes in a weather radar system to a great degree. Even though this is not sufficient for second trip retrieval but these codes work well for the suppression

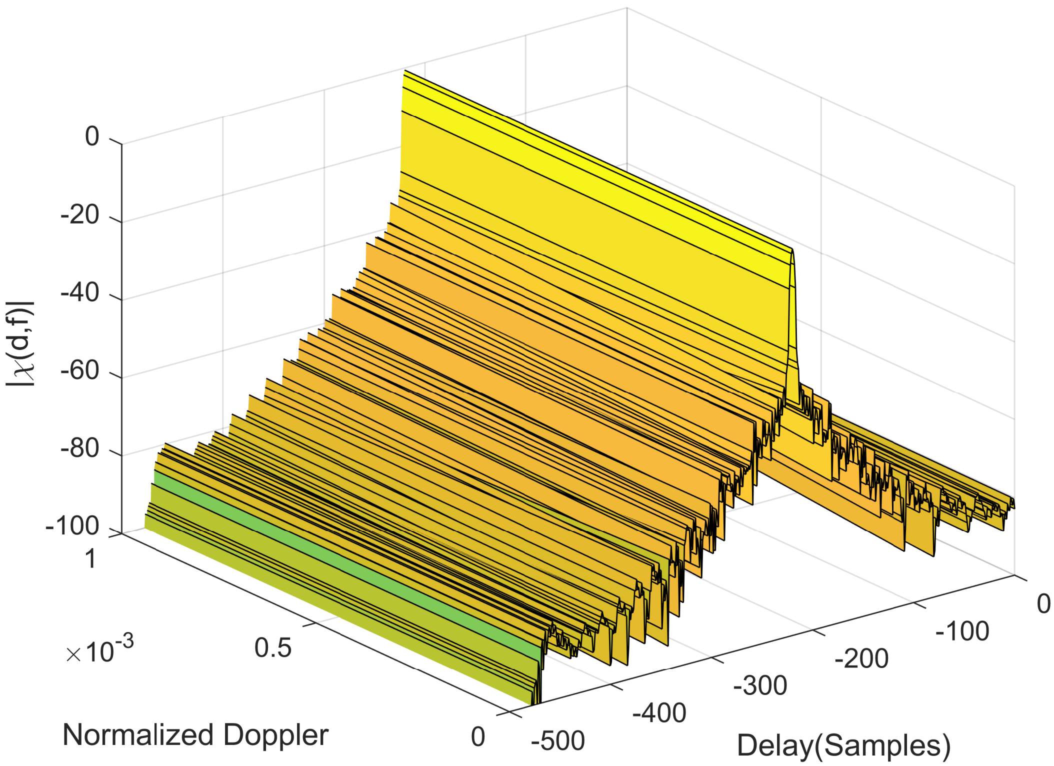

Figure 5.8: The Auto-ambiguity function plot of $\{\mathbf{a}_1 * \mathbf{b}_1\}$.

scheme as also substantiated from D3R weather radar data. Before implementing it on the actual system, we test it using a weather radar data simulator.

5.3 Simulation of weather radar signals and modeling of phase noise errors

The computer simulation of In-phase and Quadrature returns from a weather scenario is essential to study the effectiveness of these coding techniques. With the simulator, we have the capacity to evaluate the newly developed polyphase code for weather radar in a controlled environment without actually physically testing on the radar platform. The parameters for simulation are the values from the NASA D3R weather radar system (Ku band) which has recently been upgraded

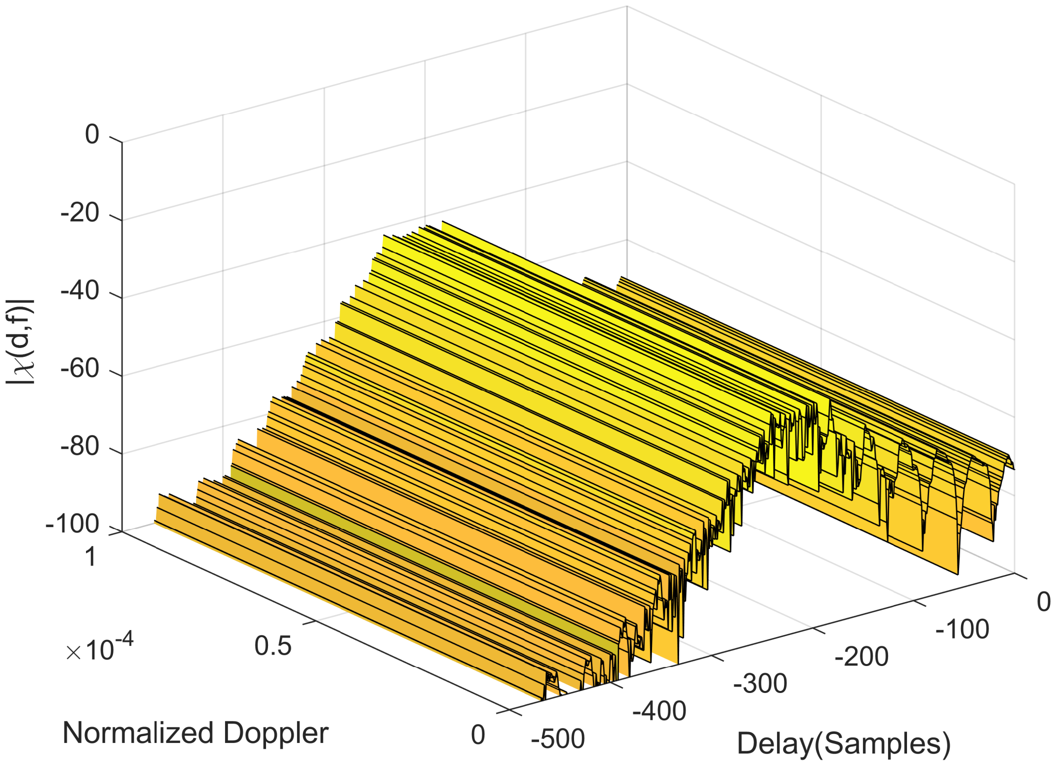

Figure 5.9: The Cross-ambiguity function plot of $\{\mathbf{a}_1 * \mathbf{b}_2\}$.

with new IF sub-systems [50], [51]. A brief specifications of this radar are given in Table 5.1. The time series simulation of weather echoes for a radar is detailed in [46].

Table 5.1: Brief Specifications of D3R (Ku band)

Specification	Value
Frequency	13.91 GHz $\pm$ 25 MHz
Range resolution	150 m (nominal)
Maximum operational range	39.75 km
Peak power	200 W per H and V channel
Receiver dynamic range	90 dB

The weather radar simulator generates a Gaussian time series $x(nt_s)$ with mean zero and variance σ_f^2. To impart a velocity f_D,

$$y(nt_s) = x(nt_s)exp(2\pi f_D nt_s). \tag{5.30}$$

This time series is complex Gaussian centered at f_D. This received signal after down-conversion has a component of transmit and receive phase noise and can be written down as:

$$y(nt_s) = y_{wpn}(nt_s)exp(j\phi(nt_s)) + w(nt_s), \tag{5.31}$$

where $\phi(nt_s)$ denotes the phase noise process and $w(nt_s)$ is zero-mean complex-valued additive white Gaussian noise (AWGN) that models the effect of noise from other components of the system. The phase noise can lead to perturbation of polyphase codes and the sidelobes. Convolution of simulated weather echo returns with polyphase code will lead to uncompressed receiver down-converter samples. Next, if we convolve it with mismatched filter coefficients, this would simulate polyphase code being transmitted, scattering through a weather event and being received/compressed with mismatched filter. Hence the utility of generated code-filter pairs can be assessed. It can be written down as:

$$y_{exp} = (y * C) * C^*_{filt}, \tag{5.32}$$

where y_{exp} consists of samples obtained after effects of polyphase code C, mismatched filter coefficients, C_{filt} and phase noise. The $*$ denotes convolution operator. The whole simulation process is depicted in Fig. 5.10.

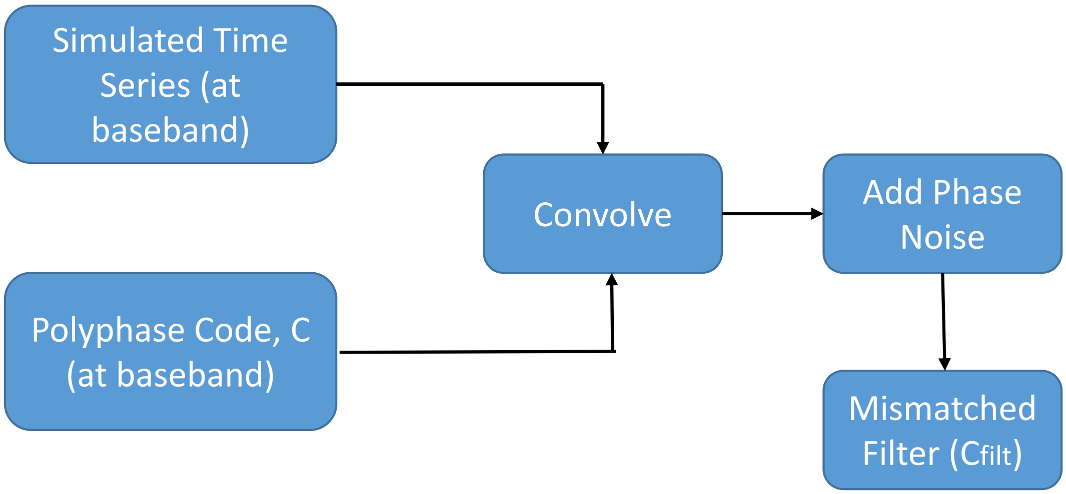

Figure 5.10: The process of simulating weather echoes to validate the performance of polyphase codes.

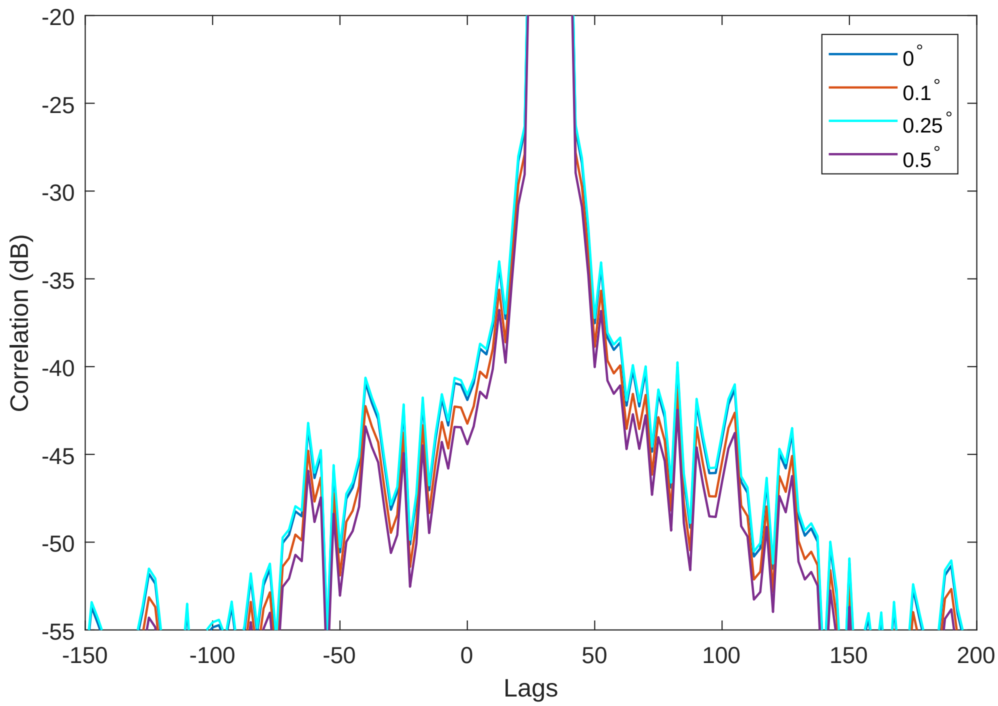

Figure 5.11: Effect of system phase noise on performance of code-filter pairs with cumulative transmit and receive phase noise. The rms values shown are phase jitter calculated from phase noise, integrated over the receive bandwidth.

Before moving on to the actual weather time series simulation and results, we undertook a single target simulation to analyze the peak sidelobe degradation with phase noise. These are

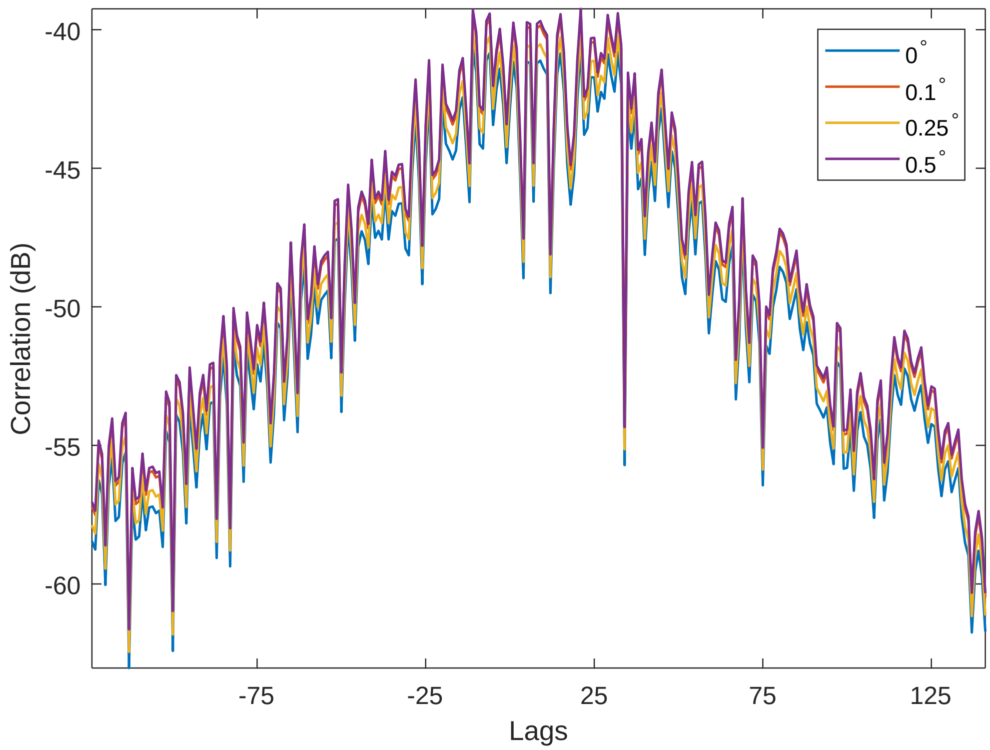

Figure 5.12: The phase noise degrades the peak sidelobe level in the cross-correlation function between the code 2 and mismatched filter 1. Only one pair of cross-correlation function is plotted here, to show the phase jitter effect.

depicted in the Fig. 5.11 and 5.12. The peak sidelobe level is getting worse by 3-4 dB as we go from no phase noise case to $0.5°$ RMS phase noise (phase jitter). Now let's proceed to define a method where we can incorporate the generated optimal two code-filter pairs and test for the second trip suppression capability of these codes.

Method

To test second trip suppression, one pair of code will be generated with good auto and cross-correlation properties, by following the global optimization procedure in sections above. The alternate pulses will be modulated with the same code. Let's say, the pulse 1 gets modulated with code C1 and the pulse 2 with code C2 and so on. The filters for this code to be loaded in such a way that to recover first trip parameters, we load the filter with coefficients P1 and P2 during the pulse time-coded with C1 and C2 respectively. However, to recover the second trip parameters,

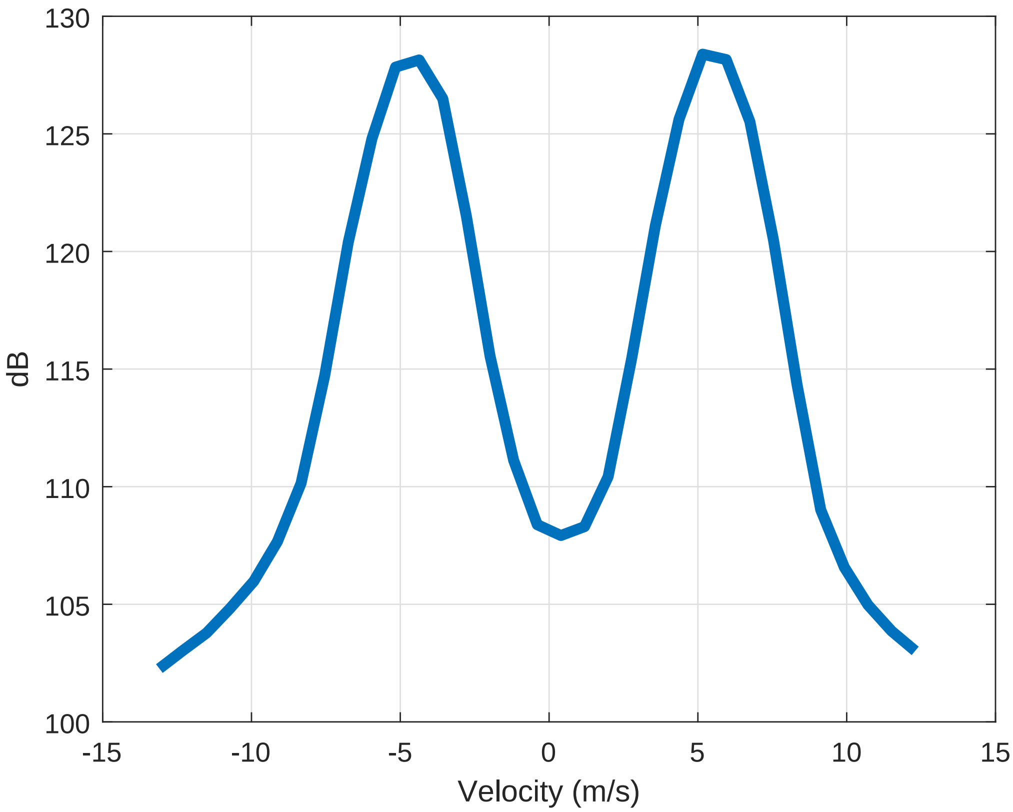

Figure 5.13: Overall combined spectrum of simulated first and second trip echo with equal power ratio with parameters: $BW = 2MHz$, $PW = 40\mu s$.

we load the coefficients P2 and P1 during the pulse time-coded with C1 and C2, respectively. It is to be noted that P1 was generated to optimize the autocorrelation with C1 and cross-correlation with C2 and vice-versa. To recover both trips simultaneously we need two filters, one loaded with coefficient sequence P1 and P2 for recovery of first trip while the other filter loaded with coefficient sequence P2 and P1 for recovery of second trip parameters. It is to be noted that in this thesis, we are trying to show the suppression capability for second trip echoes and not their retrieval ability. A good retrieval code must have a much lower peak cross-correlation and sidelobe levels with the other pair (so that a much higher first trip power will have sufficient suppression, to be a practically viable option).

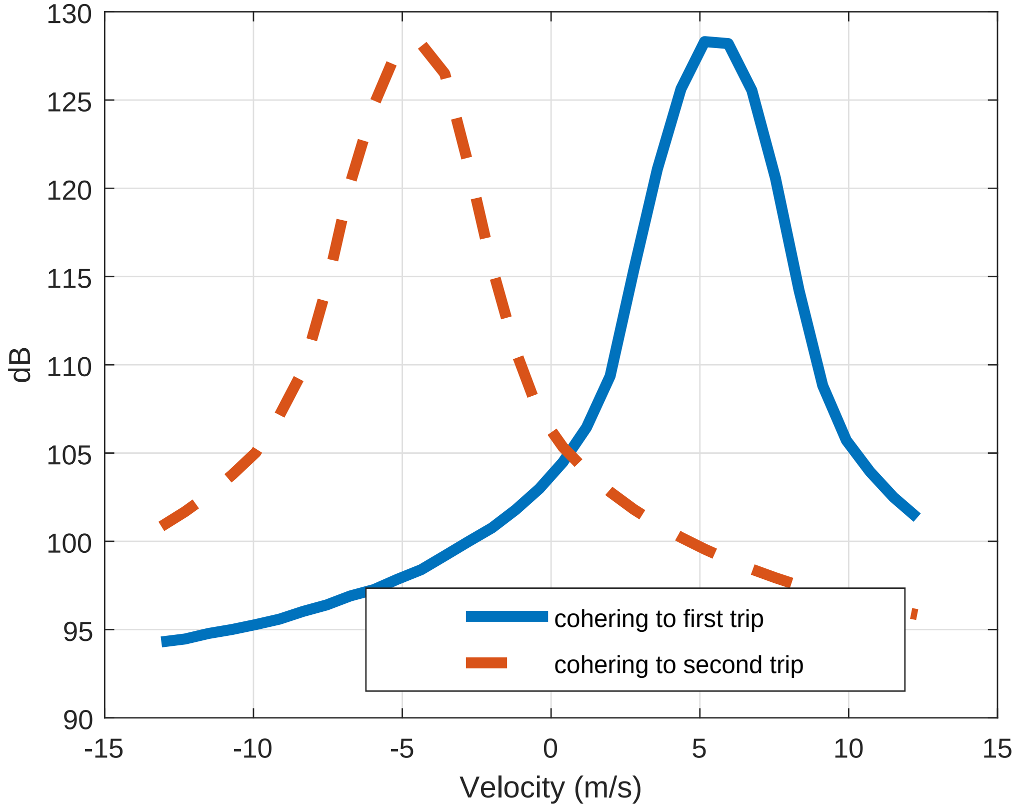

Figure 5.14: Second trip/first trip suppression obtained with orthogonal polyphase codes.

Simulation Results

To demonstrate improvements for second trip suppression, we convolve with the generated codes, pulse wise, to have the modulated time series echo returns from each range gate. Fig. 5.13 depicts the power ratios of the first and second trips used for simulation with the first trip centered at 5m/s while the second trip at -5m/s. After the combined signal goes through P1/P2 filters, Fig. 5.14 depicts the power ratios achieved. There is > 20dB of suppression of second trip observed using the simulation method and it can greatly reduce the bias on the measurement of dual-polarization moments of first trip. Hence the quality of measurements for the first trip can be vastly improved. Later similar levels of suppression of second trips were observed even in radar data.

5.3.1 Effect of system phase on polyphase code performance

There is an extra phase term added on top of the phase of the polyphase code which is due to the summation of group delay for the transmit and receive chain's components. This is referred to as the system phase and should be measured and subtracted out to improve performance. The true phase of the pulse compressor system using a polyphase generator can be obtained through simulation and the system phase can be measured on top of the true phase value, using the calibration loop. The various constant system phase terms in D3R architecture are shown in Fig. 5.17. The ϕ_w is the actual code phase that should be ideally measured at the digital receiver. However, what would be measured is $\phi_t + \phi_e + \phi_r + \phi_w$, which are the transmitter phase, extra phase term and the receiver phase respectively. Through the calibration loop, we can measure $\phi_t + \phi_c + \phi_r$ where ϕ_c is the phase term through the coupler. This is the closest we can measure system phase in D3R and can be compensated.

5.4 Observations from NASA D3R Weather radar

D3R has synchronous operation between Ku-band (13.91 GHz) and Ka-band (35.56 GHz). It is based on solid-state transmitters and the processing is capable of pulse compression in real-time using FPGA based digital receiver system. Recently, the D3R radar was upgraded with a new version of digital receiver hardware and firmware which supports larger filter length and multiple phase coded waveforms and also newer IF sub-systems. The second trip for D3R would correspond to echoes beyond 75 km for a $500\mu s$ pri. One of the cases where suppression of second trips with the synthesized polyphase codes could be observed is depicted in Fig. 6.13. Although, we can have cross-correlation function (zero-doppler cut) $\sim$ 40dB below the auto-correlation peak, for a single target case. However, it should be emphasized that for a weather scenario, since the scatterers are continuous, the cross-correlation sidelobes may interfere constructively to degrade the peak sidelobe level achieved with a single target case.

A good amount of rejection of second trip echoes can be observed in this case, in the reflectivity and velocity spectrum, for the polyphase combination. To quantify this, we plot the power profile for the normal transmission and with polyphase coding for this case, along radial at $238°$ azimuth. This is shown in Fig. 5.18. It can be easily seen that the coding has cleared up the second trip echo and beyond 18 km of range, it is reduced below the noise floor. The velocity plot in Fig. 5.19 compares the suppression that the polyphase codes have over normal transmission in the second trip velocity domain. More than 20dB of reduction in second trip power can be observed from these velocity plots. Another case with a second trip visible in the D3R unambiguous range is shown in Fig. 6.15. In this case, all the weather echoes appearing in radar range is second trip. Also, it was confirmed with nearby FTG radar station based in Denver, Colorado (part of NEXRAD weather network). The spectral plots for ray at radial $118.8°$ azimuth, depicts the removal of second trip velocity. From these plots, at least 20dB of suppression of second trip echoes can be observed. And these observations are in line with the simulation results of section 5.3.

The concept of intra-pulse coding (the polyphase coded waveforms demonstrated here) is quite different from the existing Chu code based suppression schemes (inter-pulse coding), which is being used in NEXRAD (Next generation weather radar) SZ modes. Some of these differences were enumerated in section 5.1. It should be emphasized that the second trip suppression capabilities of Chu inter-pulse based codes have been shown to be $\sim 40dB$ in [30] and in our case also, it is close to this number at similar phase noise conditions. However, the rejection of echoes from the trips of non-interest, in case of the Chu codes, is a function of spectral widths and would degrade in case of multi-modal distributions and wider spectral width.

5.5 Conclusion

The utility of intra-pulse polyphase coding techniques for weather radar systems is demonstrated and the recent research in developing codes with good correlation properties was utilized for weather radar application. A new polyphase code and mismatched-filter-based compression system has been developed to generate multiple code-filter pairs with optimal correlation properties. In this work, we focused on the design of two such pairs, however, in general, this framework can be used to synthesize multiple pairs. This technique has been applied for second trip suppression for D3R weather radar. Simulations were carried out, initially, to ascertain the performance of these new polyphase codes. The real-time implementation was carried out in NASA D3R weather radar, to see the suppression abilities of the developed code-filter pairs. Although the suppression ability of these codes are limited by the cross-correlation function between the pair of codes, shown to be $\sim$ 40 dB for single targets, a much better result could be obtained at the cost of mainlobe broadening (leading to reduced resolution) or a much larger length of the mismatched filter (more resources). We agree that a much higher level of performance is required for better suppression for second trip weather echoes and is a topic of further research. Additionally, the pair of codes used in this work, does not have suppression for odd trip echoes. However, using the same framework, more code-filter pairs can be synthesized, and third, fourth and so on pulses can be coded to achieve odd trip suppression as well. But the cross-correlation sidelobe levels may degrade.

Also, it should be highlighted that for a short-wavelength radar as D3R, a short duration (1μs) pulse is utilized to mitigate the blind range of the long duration (20μs) pulse. The short duration pulse is uncoded and would still have second-trip contamination. As far as dual-polarization moments like differential reflectivity, co-polar correlation coefficient, and differential phase are concerned, our idea is that since the same polyphase code-filter pair would be programmed on both horizontal and vertical polarizations, pulse wise. Then there is no adverse impact on these moments.

Another bottleneck lies in the implementation of large length of mismatched filters in firmware (FPGA) which complicates the overall design. But with the advancement of FPGA design techniques and better and larger devices available, this limitation is readily being overcome.

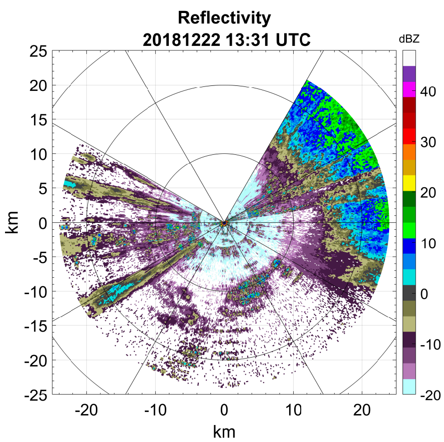

(a)

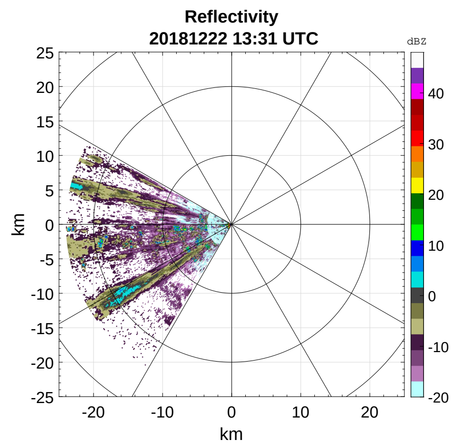

(b)

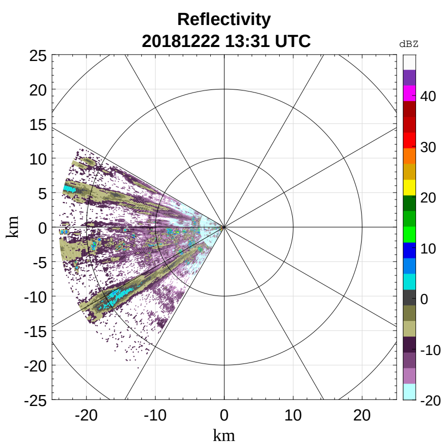

(c)

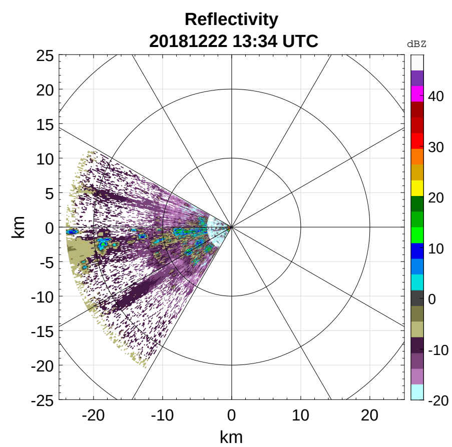

(d)

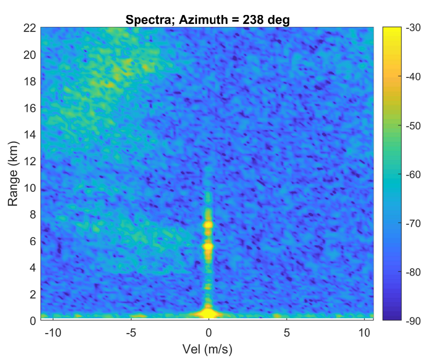

(e)

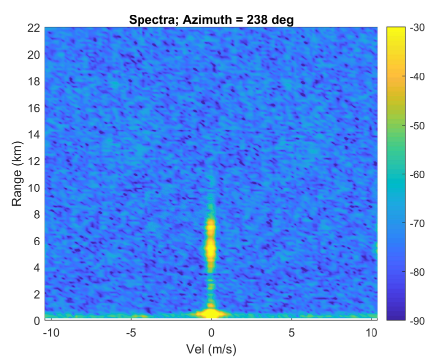

(f)

Figure 5.15: (a) and (b) depict the reflectivity without polyphase codes. It is using a chirp waveform. The south-west region has second trips as confirmed with a Nexrad radar. The first trip lies towards the north-eastern region in this case. (c) and (d) are coded with orthogonal polyphase. The elevation is 2 deg and clearly suppression can be observed at $\sim$ radial 238 $^\circ$ azimuth. (e) shows the doppler spectra along the same radial, for normal transmission, whereas, (f) has the same measurement but polyphase code and filter pairs are used.

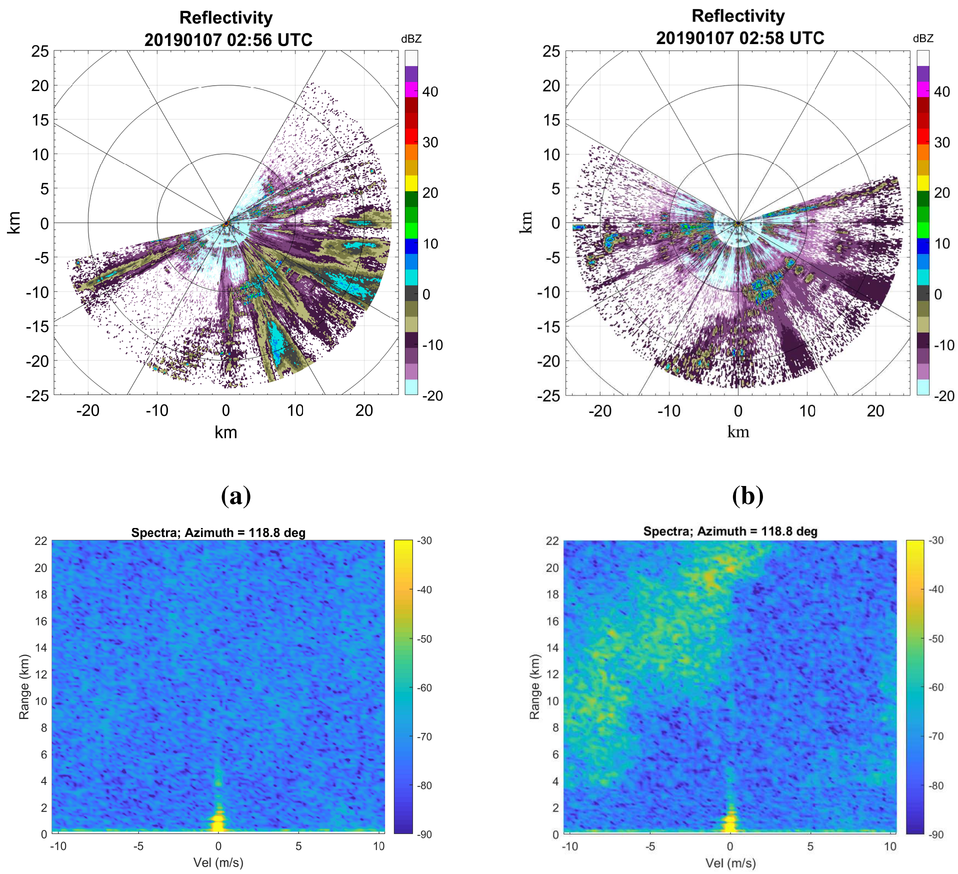

(a) (b)

(c) (d)

Figure 5.16: This case was recorded with D3R when only second trips are present in the unambiguous range. (a) and (b) shows the reflectivity with normal transmission and with polyphase codes respectively. Reduction in second trip power are easily evident from these images. (c) and (d) are doppler spectra along a radial, for polyphase coded and normal transmission respectively.

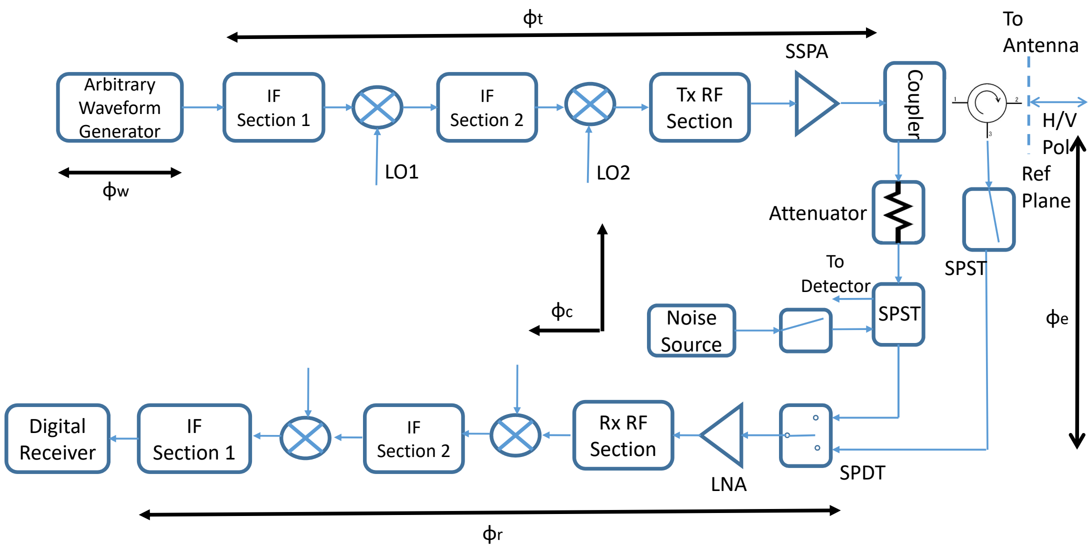

Figure 5.17: The various constant system phase terms due to transmit components (ϕ_t), receive components (ϕ_r), the coupling elements in the calibration loop (ϕ_c) and the extra path (different from calibration loop path) in the receive (ϕ_e). For more details on D3R architecture, refer to [1].

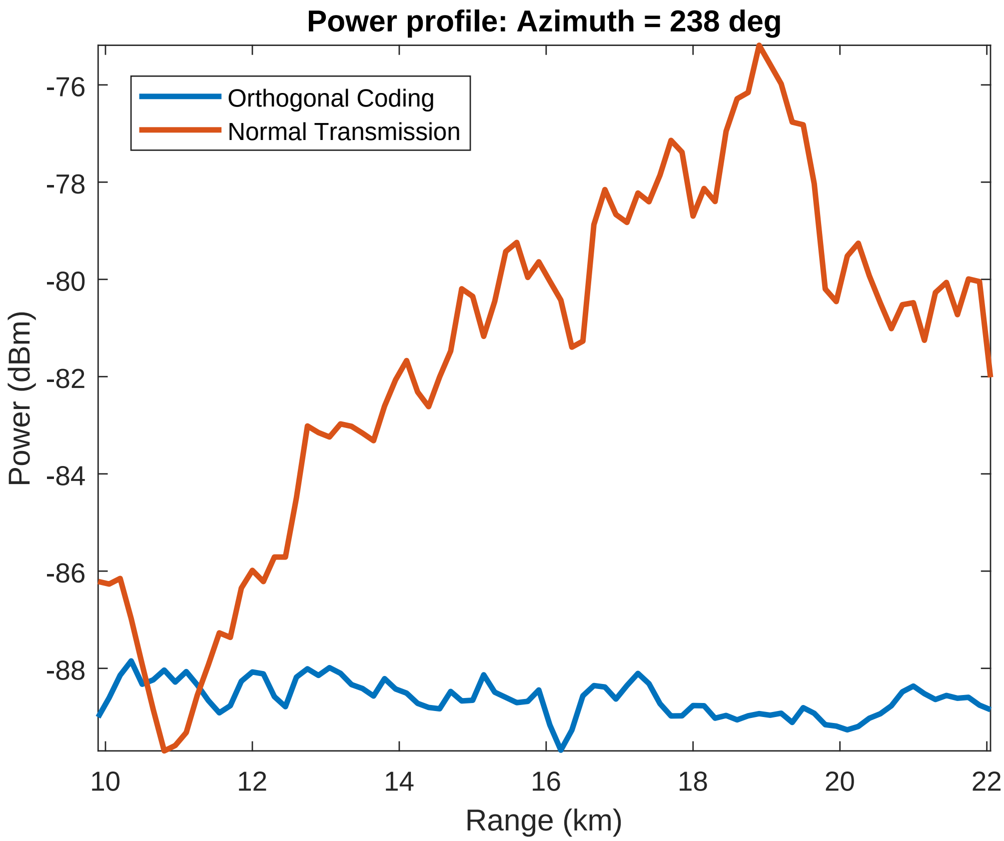

Figure 5.18: Power profile along ray at radial 238° azimuth, clearly depicts the second trip suppression capability of the orthogonal polyphase codes.

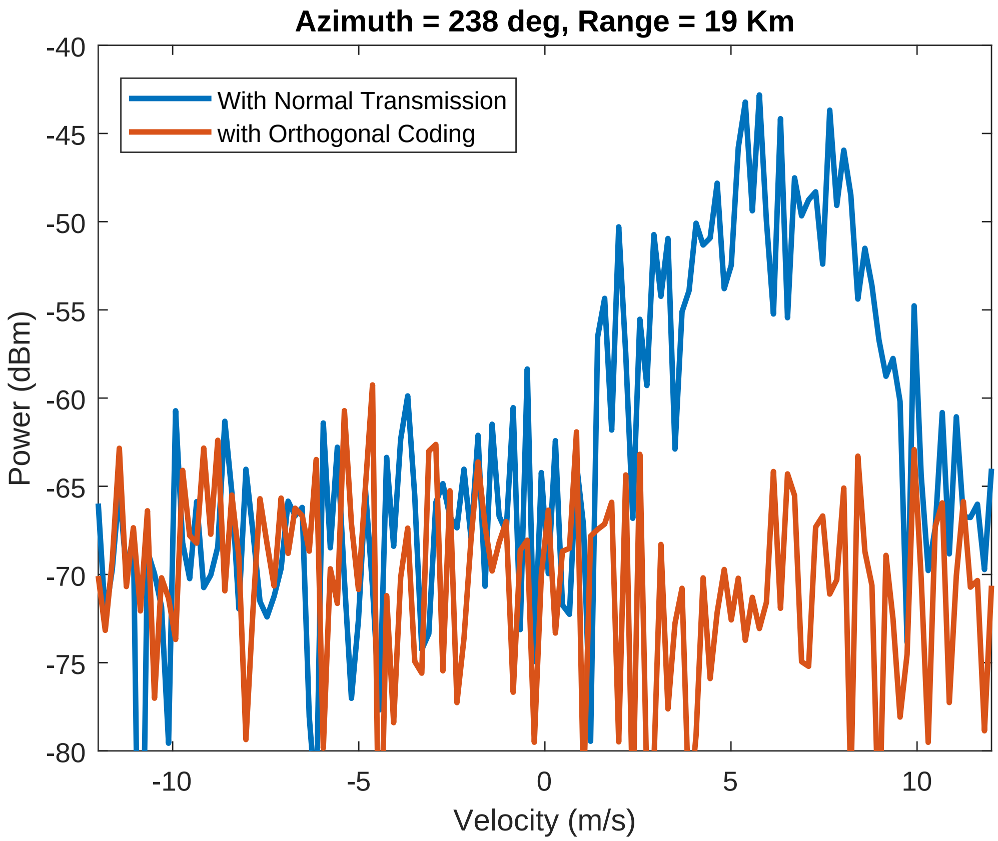

Figure 5.19: Velocity profile of second trip, observed for normal and polyphase coded transmission. These profiles are for cases shown in (b) and (d) of figure 6.13.

Chapter 6

Inter Pulse Frequency Diversity Scheme for Second Trip Suppression and Retrieval in Weather Radar

6.1 Introduction

The phase coding method tags the transmit waveform with a phase code and the same code is used in demodulation to retrieve the pulse parameters (a midst interference from different pulses like second trips or cross polar coupling) in a weather radar system. The phase code can be a single tag used for a pulse (inter-pulse coding) to separate out multiple trips. This can aid to suppress the superposition of other trips on the first trip, and for the recovery of these multiple trips under certain restrictions. The first trip, here, refers to the unambiguous range defined by the pulse repetition time (PRT). However, the echoes due to strong weather event after the unambiguous range defined by the PRT, can be classified as second, third and so on trips depending upon the multiple of PRT's range that they correspond to. The suppression effect of the phase code could be observed over the full cycle of coherent processing, which is the coherent interval to generate polarimetric moments from raw data.

In pulse Doppler weather radars, the pulses are transmitted at the pulse repetition interval of τ sec, the maximum unambiguous range is given by $r_{unb} = c\tau/2$ and the maximum unambiguous velocity is given by $v_{unb} = \lambda/4\tau$, where λ is the wavelength of operation. Hence, both r_{unb} and v_{unb} are inversely proportional to each other. Due to this, unambiguous range and velocity cannot be simultaneously optimized. If one is increased, the other one is inversely affected. This is termed as range-Doppler dilemma. A high Pulse Repetition Frequency (PRF = 1/PRT) radar system would be able to measure high Doppler velocity but the unambiguous range would suffer, whereas a low PRF system, would detect weather events going on at much farther range but the velocity would be folded in the Doppler domain. For a medium PRF system, it would be difficult to measure both range and velocity without ambiguity. This problem is more prominent for weather radar systems as the scatterers are continuously distributed throughout the beam illumination volume, with large dynamic range ([5]).

Different phase coding schemes exist in literature to overcome this basic limitation and retrieve polarimetric moments from the second, third and so on, trip echoes for a weather radar. These codes can be broadly classified into intra-pulse (phase changes on a sub-pulse basis, [56]) and inter-pulse (phase change on a pulse basis) codes. The random phase codes and systematic phase codes, are examples of inter-pulse phase codes, popular to retrieve first and overlaid second trip echoes ([30]).

Staggered and dual PRF techniques are other methods described in [11], [12], which are generally used to improve r_{unb} and v_{unb}. In particular, they are very effective in increasing the v_{unb}. This is typically accomplished through the use of PRF diversity by playing two PRF's one after the other or in batches. However, it takes more scan time and uses N times the time required for the constant PRF, N being the number of stagger pulses. Additionally, it requires more processing to perform range or Doppler unfolding compared to a uniform PRF radar.

Inter-pulse codes have been explored extensively in the weather radar community for second trip echo suppression ([30]) and for orthogonal channel coding as in [32] for dual-polarization weather radars. The retrieval of moments for the first and second trips, is based on spectral processing of weather echoes in batches of coherent intervals (depending upon the antenna rotation rate and the de-correlation time of weather echoes). The orthogonality of the code, for first and second trips, is achieved over the coherent interval as the second trips get modulated by cyclic shift of the phase code. The separation between first and second trips is achieved by having these cyclic shifts orthogonal to each other. The systematic codes use the derivatives of Chu codes which present deep nulls in the cross-correlation function for time delayed versions of themselves. However, the rejection of echoes from the unwanted trips, is a function of spectral width of the weather echoes and would degrade in case of multi-modal distribution, wider spectral width of the weather echoes and in the presence of phase noise.

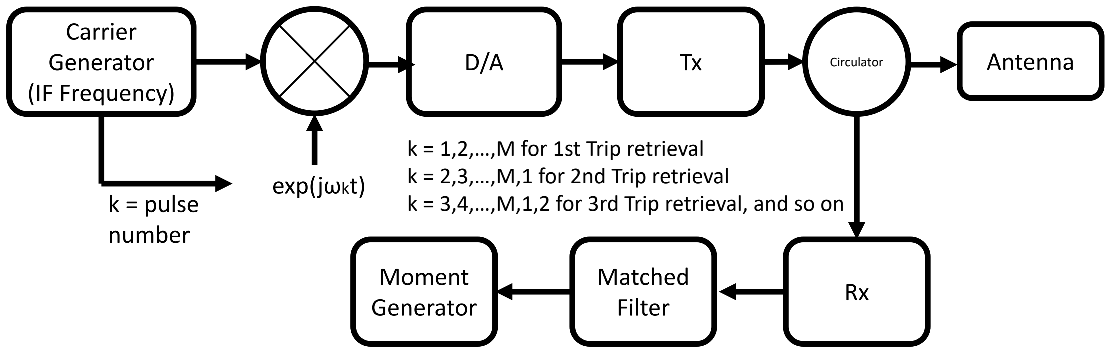

Figure 6.1: A system architecture for multi-trip retrieval.

In this thesis, we introduce a novel frequency diversity inter-pulse scheme and discuss its implementation on the NASA D3R weather radar. In the proposed scheme, we change the IF frequency from pulse to pulse. For example, for second trip suppression, we use two frequencies, f_1 and f_2 for alternate pulses and beat them separately with two digital down-converters to recover both first and second trips. If the frequencies are properly selected, it gives first and second trip retrieval abilities. However, if these frequencies are far apart by more than the transmit waveform bandwidth, then power returns from hydrometeors become uncorrelated between these two set of pulses. Then we discuss a novel method to retrieve velocity and spectrum width, for the first and second trips under these constraints of pulsing scheme with f_1 and f_2 for alternate pulses. This method can recover velocity and spectral width, from a batch of coherent processing time (128 pulses, in case of D3R), without compromising the unambiguous velocity range. The improvement in the second trip recovery region, based on the ratio of $|P_1/P_2|$, where P_1 is first trip power and P_2 is second trip power, is observed. A block diagram of this scheme is shown in Fig. 6.1. The carrier generator outputs two different oscillations at frequencies, f_1 and f_2, for odd and even pulses, respectively. If the sequence at the down-converter is f_1 and f_2 for odd and even pulses, we would be able to recover first trip. However, if the sequence is f_2 and f_1, then we would be recovering second trip parameters.

Many orthogonal polyphase coded systems have been proposed in literature, as in [28], [27], [26] and [34]. They are part of a broad category of phase coding schemes called intra-pulse coding elaborated by [56]. But it is very difficult to obtain a peak cross-correlation function between different polyphase codes lesser than $-40dBc$ (with respect to the peak auto-correlation function of these polyphase codes). The frequency diversity scheme proposed in this thesis is meant to give a higher level of isolation that is possible with polyphase or intra-pulse coding. The limits on the peak auto-correlation and cross-correlation sidelobes of the sequences (which limits th turn the orthogonality between these sequences in case of intra-pulse codes) have been discussed in [36] and [37]. These lower bounds on the cross-correlation of polyphase codes tell us that there is a need to explore other techniques. In his correspondence in [36], the author points out that if a set of sequences has good auto-correlation properties, then the cross-correlation properties are not very good and vice versa. He has also brought out a result which shows the trade-offs between the maximum magnitudes of the correlation functions. And further derived an inequality which provides a lower bound on one of the maxima if the value of the other correlation function is specified. However, for weather based radar application, there is a need for lower peak sidelobe levels for both auto- and cross-correlation functions. Hence our proposed scheme which works with alternating frequencies (apart by more than the transmit bandwidth) seeks to overcome this limitation. This can also address the ever growing need for orthogonality in MIMO systems ([18]). In MIMO radars, all transmit elements can radiate at the same time without interfering with each other using frequency diversity. And the same approach may work for CDMA based communications too ([40]).

Having said this, we also want to point out that frequency diversity has been existent and used in the past for weather radars in various extents and combinations. For example, in [57], frequency diversity is used for range extension and by estimating unknown phase due to frequency change pulse to pulse for velocity retrievals. However, estimation of spectral width for weather echoes is not mentioned in this. Moreover, there is no quantification of results, for example, how does this technique compare against the inter-pulse Chu based phase codes or any other scheme. And also no mention of practical phase noise conditions. Similar is the case with [58], where the inventors have used frequency diversity pulse pair methods by alternating the order of the pulse pair transmitted or of multiple pulses on different center frequencies. But the performance quantification for practical radar systems is also lacking in this case.

6.2 Inter-Pulse Waveforms

6.2.1 Generalized Chu codes for second trip suppression and retrieval:

The most popular inter-pulse codes, are the systematic phase codes (SZ), detailed in [30] for the retrieval of parameters of overlaid echoes. In this thesis, the performance of SZ codes are based on the Chu phase codes that are analyzed for the second trip suppression and retrieval. We use this as the reference performance and compare it with the proposed frequency diversity scheme. A point to be noted here is that under a large spectral width of weather assumption, the SZ codes, which rely on replicating the other trip spectra multiple times (while cohering to one trip, which is being recovered), become "white" due to a large overlap between the replicas. Another inter-pulse code which introduces uniformly distributed random phase on pulses (known as random phase code), attempts to whiten the weaker trip, while it coheres the stronger trip signal, whereas the SZ code produces replicas of the weaker signal spectrum. If a notch filter is used in a random phase code, it also removes some part of the second trip spectrum, which cannot be recovered later on, thus producing a self-noise ([13]). Also, while notching out, the Gaussian spectrum of precipitation broadens due to ground clutter and phase noise etc. Hence, to completely notch out the stronger trip, a much wider notch filter is essential (apart from the notch width required for the Gaussian spectrum width). The proposed frequency diversity scheme is immune to overlaid spectrum between the first and second trip echoes, which is also, one of the biggest advantages of this scheme. Since the second trip echo is filtered out in the fast time domain by the FIR baseband down-converter filter, the slow time spectral domain will not have any contamination when we are processing first trip echoes for velocity and spectral width. This is also true when we are estimating second trip velocity and spectral width by notching out the first trip power in the fast range time domain.

Coming back to self-noise, one more reason for its generation is the excessive overlap of the spectral replicas (these replicas were discussed in last paragraph in context of SZ codes). A deeper analysis of an SZ code indicates that these can be characterized by variables N and M to form an SZ(N/M) code. The SZ code (simulated here) is designed in accordance with equation (6.1) with $N = 8$ and $M = 64$. Details on the formulation of SZ code and the parameters N and M can be found in [30].

$$c_k = exp(-j\Sigma_{m=0}^{k}(N\pi m^2/M))$$
$$k = 0, 1, 2, ..., M-1 \tag{6.1}$$

If the spectrum of the precipitation echoes lies within $M/8$ spectral coefficients in the spectral domain (for SZ(N/M) where $N = 8$ and $M = 64$), then there would be less overlap between successive replicas and better estimation can be performed. But in case of wider spectral width, the overlap region can pose a constraint for the recovery region of velocity and spectral width. In such a case, the SZ(4/64) code with $N = 4$, will most likely provide a better separation in exchange for allowing a much lesser notch width, in order to retain a minimum of two spectral replicas. Additionally, the phase noise leads to broadening of the spectrum, which can be linked to phase noise of the coherent oscillator used to synchronize various sub-systems of the radar.

The cyclic version of SZ(8/64) code (known as modulation code) has eight replicas of the second trip in the Nyquist interval along with the original spectrum of the first trip echo. Once the higher power echo of first trip has been notch filtered, the remaining replicas aid in estimation of second trip parameters. A minimum of two replicas are required for velocity computation and later magnitude de-convolution for spectral width computation ([30]). We simulated weather echoes, with a moderate rainfall scenario for a radial (method described in [59]). In this simulation, the first trip has the following parameters: velocity $(v_1) = 10m/s$, spectral width $(w_1) = 1m/s$ and co-polar correlation coefficient $(\rho_{hv}) = 0.995$ and the second trip has the same parameters, except

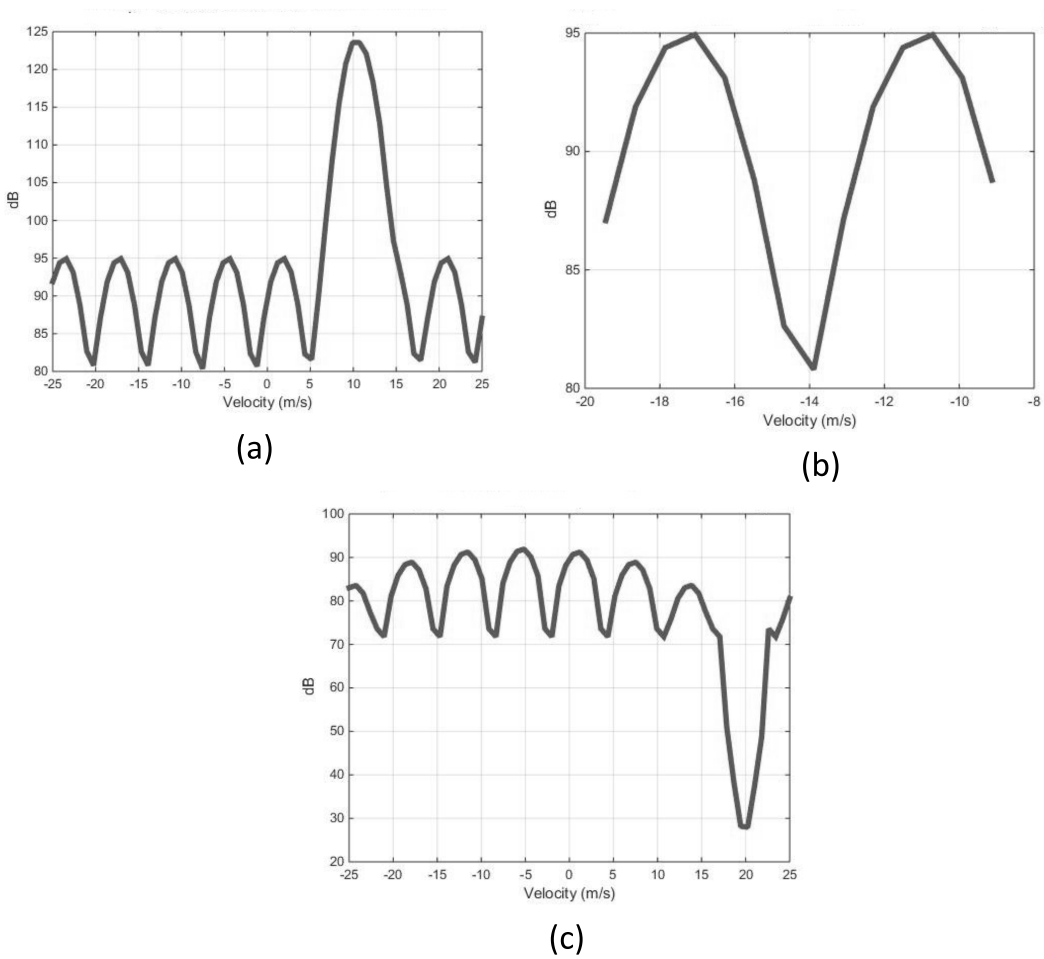

Figure 6.2: (a) The combined first and second trip echoes velocity spectrum while retrieving the first trip echoes. The modulation code spreads out the power of second trip to 8 replicas, (b) The combined first and second trip echoes velocity spectrum while the first trip echoes have been notched out with normalized notch width of 0.75, (c) The combined first and second trip echoes velocity spectrum while retrieving the second trip echoes. The spectrum is re-cohered for the second trip with its six sidebands present in the spectrum.

for velocity, which is taken as $v_2 = -5m/s$. This was done to see the effectiveness of the SZ codes and later use it to compare with the proposed frequency diversity method of this thesis. The simulation was carried out at S-band with $PRF = 1.2KHz$. In reception, the spectrum of the total received echo consists of the spectrum of the first trip and the second trip's spectrum getting replicated 8 times (with SZ(8/64)), shown in Fig. 6.2 (a).

After estimation of the first trip parameters, the total spectrum is notch filtered, to remove the power of the first trip, and the second trip parameters can be estimated. If a rectangular window is used for truncating the signal, then the stronger trip will be contaminating the weaker trip spectrum through its spectral sidelobes, and the dynamic range, $|P_1/P_2|$, where the second trip could be retrieved, will get smaller. However, to reduce spectral leakage, if we use other window functions, that would lead to loss of signal to noise ratio (SNR) meaning a reduction of the number of independent samples. To get an effective compromise between these two factors, a Hann window is used, which has a higher SNR loss (compared to a rectangular one), but the spectral dynamic range gets substantially increased. The loss is incurred due to an aggressive amplitude taper to contain the energy in sidelobes which also leads to mainlobe broadening. After the notching process, at least two replicas need to be retained for velocity and spectral width estimate. The spectrum after the notching process is shown in Fig. 6.2 (b).

The remaining signal (after filtering out first trip) has six symmetrical sidebands centered at the mean velocity of the second trip, as shown in Fig. 6.2 (c).

6.2.2 Effect of Phase Noise on SZ/Chu Codes:

The phase noise (also referred to as jitter), is a major limiting factor for the dynamic range of $|P_1/P_2|$ using a inter-pulse SZ/Chu codes. Phase noise leads to overall broadening of the spectrum of both first and second trips. The overall phase noise is dominated by the phase noise of the oscillator ([60]), which is a reference for the entire system. Single-side band phase noise is usually measured in a 1 Hz bandwidth and it can be defined as the ratio of noise in a 1 Hz Bandwidth to the signal power at the center frequency.

The equivalent jitter can be obtained by integrating the spectral phase noise curve over the receiver bandwidth. It is equivalent to ([60]):

$$\text{RMS Phase Jitter (in radians)} = \sqrt{2 \times 10^{A/10}} \tag{6.2}$$

where A is the area under the phase noise curve.

It has been shown in [30] that, if there is no phase noise and the Hann window function is used, the limit on retrieval of second trip velocity spans around 90dB of $|P_1/P_2|$ power ratio, for spectral width smaller than 4 m/s. But it drastically reduces to 60 dB, if the rms jitter is of the order of

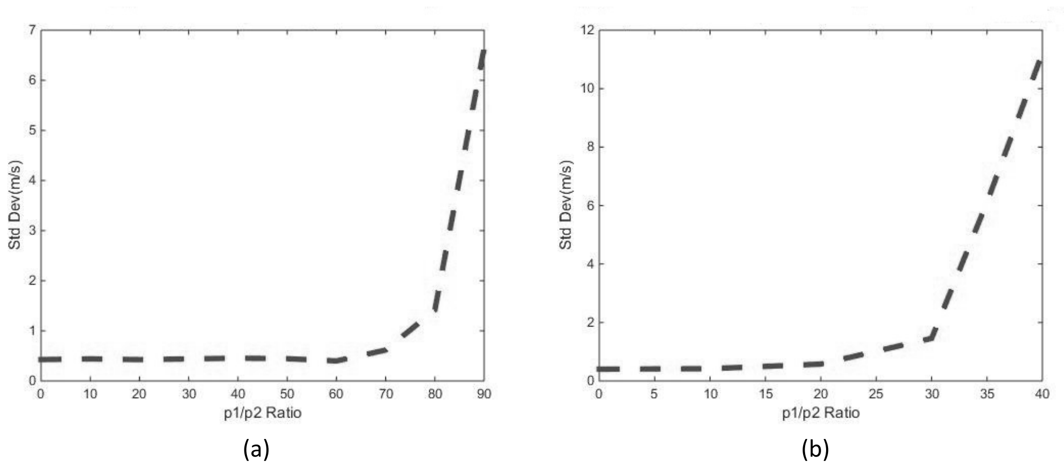

Figure 6.3: (a) The dynamic range of $|P_1/P_2|$, in which the second trip velocity can be recovered (with acceptable standard deviation limits), without phase noise, (b) The dynamic range of $|P_1/P_2|$, in which the second trip velocity can be recovered (with acceptable standard deviation limits), with phase noise.

0.2 deg rms, and further reduces to 40 dB in case of 0.5 deg rms jitter. This is also shown by the simulations of weather echoes presented in section 26.2.1 that the phase noise reduces the accuracy of the second trip velocity retrieval. The range of $|P_1/P_2|$ power ratios, in which the second trip velocity can be recovered, with and without phase noise, is depicted in Fig. 6.3 (a) and 6.3 (b) respectively.

6.2.3 Frequency Diverse Chirp Waveforms:

Modern day systems with higher computation power and embedded with FPGAs (Field Programmable Gate Arrays) are capable of high speed signal processing architectures. The digital receiver system in D3R, which now has such an architecture, is capable of switching IF (Intermediate Frequency) on a pulse by pulse basis ([51]). This feature has been utilized to obtain frequency diversity at IF. The main factor limiting the amount of second trip suppression is the IF filter, which is implemented digitally in the FPGA (based on its stop band suppression and roll off in the frequency domain). That also can decide which frequencies to select while transmitting the pulses.

Typically, when the transition of the filter frequency response from passband to stopband is steep, it requires a high number of digital multiply-accumulate (MAC) units. However, with the advent of high processing power and FPGA nodes, optimized for DSP application, we can easily obtain very sharp roll-off filters working in real time. The analog filter before the A/D converter have a wide enough passband to accommodate both f_1 and f_2. Finally, it is difficult to have large bandwidth stages, because of spurious and inter-modulation products in the mixing process, which may show up in the passband. This can also lead to reduction of the spurious-free dynamic range (SFDR).

The basic modulation on the pulses is a Chirp signal. A pulse width of 20μs and a bandwidth of 1 MHz (pulse repetition frequency of 0.5 KHz) is selected to maximize sensitivity, minimize blind range and have a reasonable data rate to the signal processor. The f_1 and f_2 will be selected based on the digital filter characteristics and will be dealt with in more detail in sub-section 26.2.3. If A_1 and A_2 denote the amplitude of first and second trip echoes respectively, then the output at mixer out port would be:

$$O_1(t) \;=\; A_1 + A_1exp(-j(2\omega_1)t) + A_2exp(-j(\omega_2 - \omega_1)t) + A_2exp(-j(\omega_2 + \omega_1)t) \quad (6.3)$$

For recovering first trip, the frequency component to be filtered out is $A_2exp(-j(\omega_2 - \omega_1)t)$. Similarly, for the next pulse, we will retain A_1 and filter out the second trip frequency component, $A_2exp(-j(\omega_1 - \omega_2)t)$. Later, we average out similar pulse sets to retrieve the first trip and the process for second trip retrieval would be very similar as well.

To gain a better understanding of the proposed frequency diversity system, we go back to our time series simulation of moderate rainfall case with the following parameters: $v_1 = 10m/s$,$w_1 = 1m/s$ and $\rho_{hv} = 0.995$. The second trip has the same spectral width and co-polar correlation coefficients, except velocity which is $v_2 = -5m/s$.

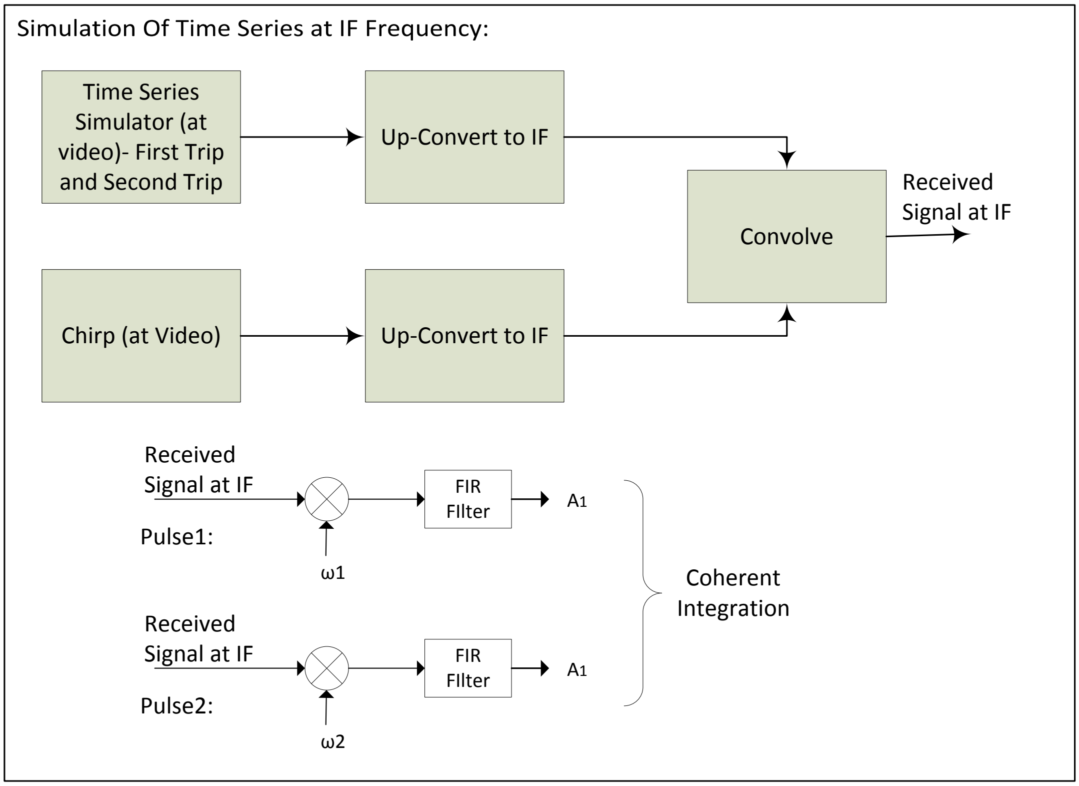

Figure 6.4: The time series simulation of weather echoes at IF frequency.

The simulated time series spectrum is centered on f_1 for the first pulse and f_2 for the next pulse in a frame. The frame is a basic unit of two pulse echoes, which repeats in time. The pulse returns are then filtered by a digital filter at baseband and then after the pulse compression process, the power of the echo signal is calculated. In the simulation, we can vary the first trip power over the second trip one, and obtain the dynamic range of values, $|P_1/P_2|$, where the parameter retrievals of the second trip are within acceptable range (based on measured bias and standard deviation). This concept of weather time series simulation is elaborated in Fig. 6.4.

Fig. 6.5 depicts both the first and second trips, with equal power, such that $|P_1/P_2| = 0$ dB, and both have rms phase jitter of 0.5 deg. The waveforms are upconverted to IF frequency. The odd numbered pulse first trip echoes are upconverted to f_1 and then combined with the even numbered second trip echoes (upconverted to f_2). The spectrum after this process, where, f_1 = 60 MHz and f_2 = 70 MHz, is shown in Fig. 6.6. This simulated first and second trip echoes are down converted

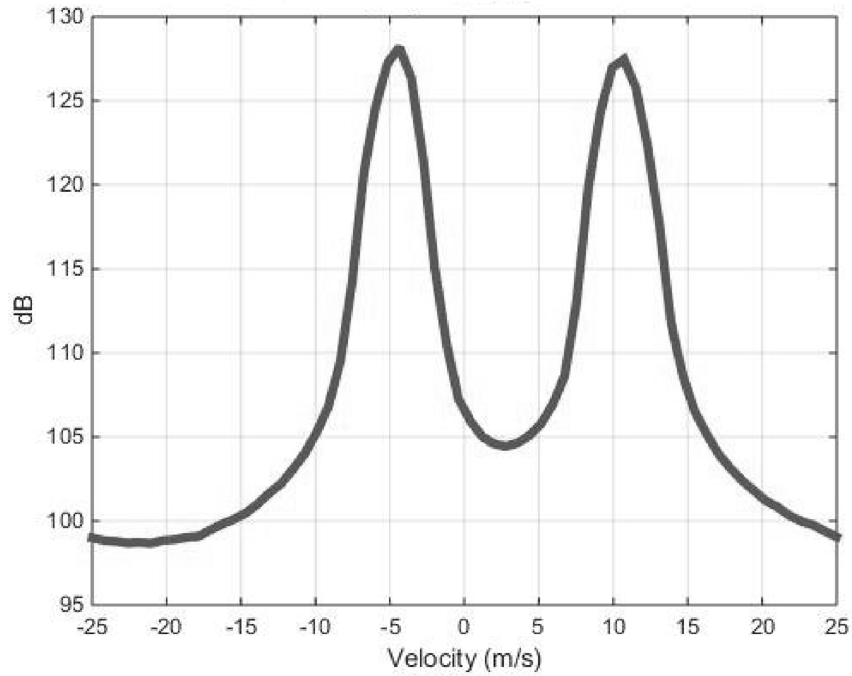

Figure 6.5: Both the first and the second trip echoes are generated with equal power such that $|P_1/P_2| = 0$ dB and with parameters: $v_1 = 10m/s$,$w_1 = 1m/s$ and $\rho_{hv} = 0.995$ while the second trip has the same parameters, except velocity of $v_2 = -5m/s$.

with appropriate IF frequency for even and odd numbered pulses. Under this setting, we have various options available to work with:

a) If we have one down converter and pulse compression system available, then we can either retrieve first trip echoes by switching the frequency to a sequence 1: f_1, f_2 for a frame of two pulse echoes, based on odd or even pulse numbers. For the retrieval of the second trip echoes, we would need to switch to a frequency sequence 2: f_2, f_1 for a two-pulse echo frame. This will require less resources but would also take twice the amount of time for retrieval of first and second trips as compared to the parallel scheme described next.

b) If we have enough resources to perform two parallel down converters and pulse compression systems, then by programming frequencies to a sequence 1 or 2, we should be able to retrieve both trips simultaneously.

c) Another approach could be, to use alternate pulse-pair echo frames for first trip, and in-between frame for second trip retrievals. In this scenario, the sequence of the IF frequency would

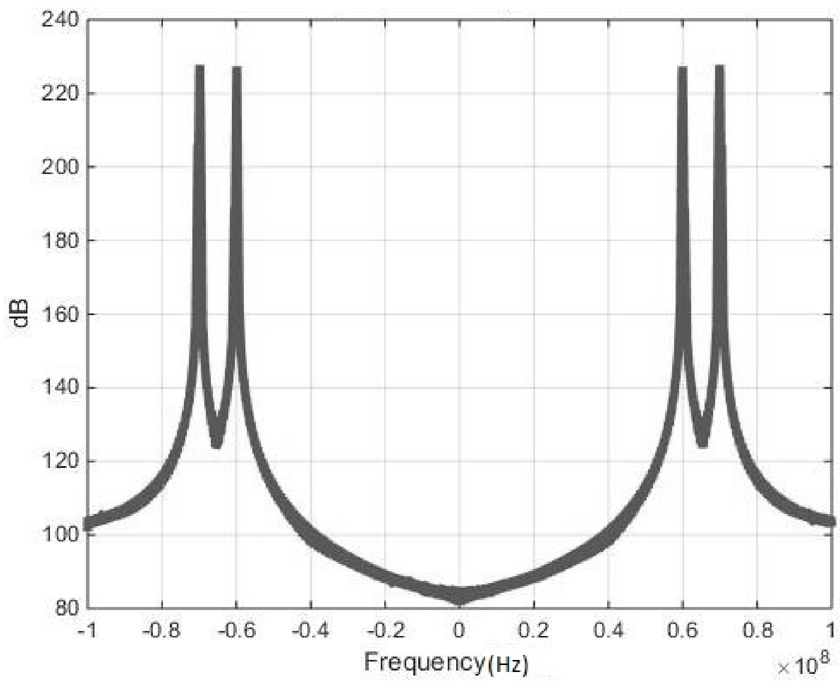

Figure 6.6: The Spectrum of Up-Converted First and Second trip echoes with f_1 =60 MHz and f_2 =70 MHz.

be: f_1, f_2, f_2 and f_1 for a frame of four pulse echoes. This scheme would have an advantage of saving resources and computational complexity is decreased.

The overall frequency response of the down-converter stage is set to allow a passband ripple of 0.2dB and provide stop-band attenuation of nearly 60 dB. The amplitude and phase response of such a filtering stage is shown in Fig. 6.7.

The spectrum after down-conversion and filtering, for the frequency sequence set for the second trip retrieval is shown in Fig. 6.8. The bandwidth of the chirp used for modulation is 0.5 MHz. Finally, we try to compute the velocity of second trip echoes, with a power ratio $P_1/P_2 = 0$ dB over a set of coherent processing pulses (64 here) and PRF of 1.2 KHz at S-band. This is shown in Fig. 6.9.

The spectral noise floor is dominated by phase noise of the echoes received, which negatively impacts the dynamic range of $|P_1/P_2|$. This fact has been demonstrated before using Chu (SZ) inter-pulse codes. Recall that the second trip could be recovered for the power ratio ($|P_1/P_2|$)

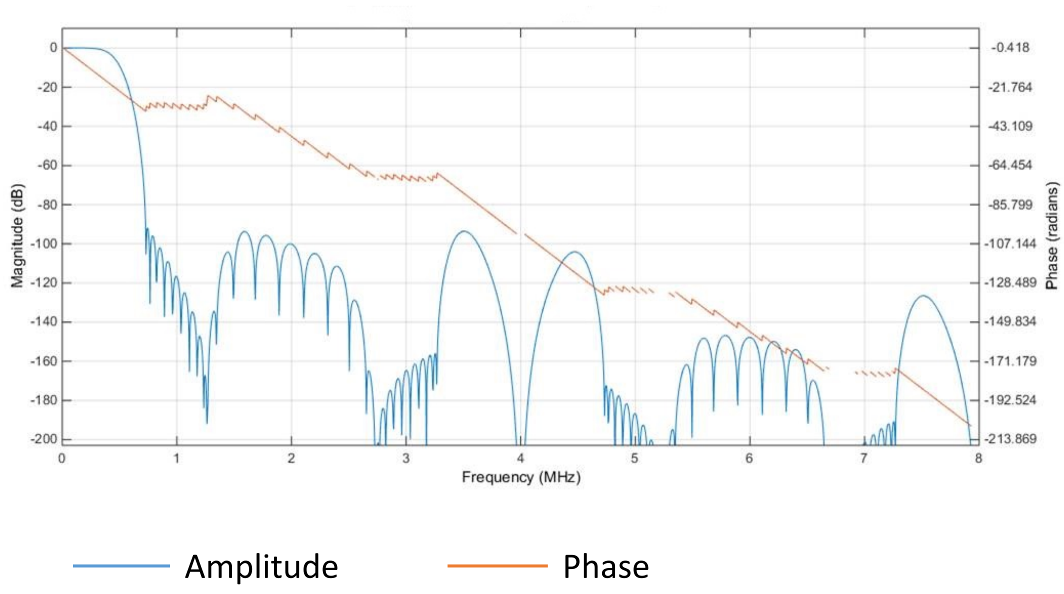

Figure 6.7: The filter response (amplitude and phase) of the down-converter stages.

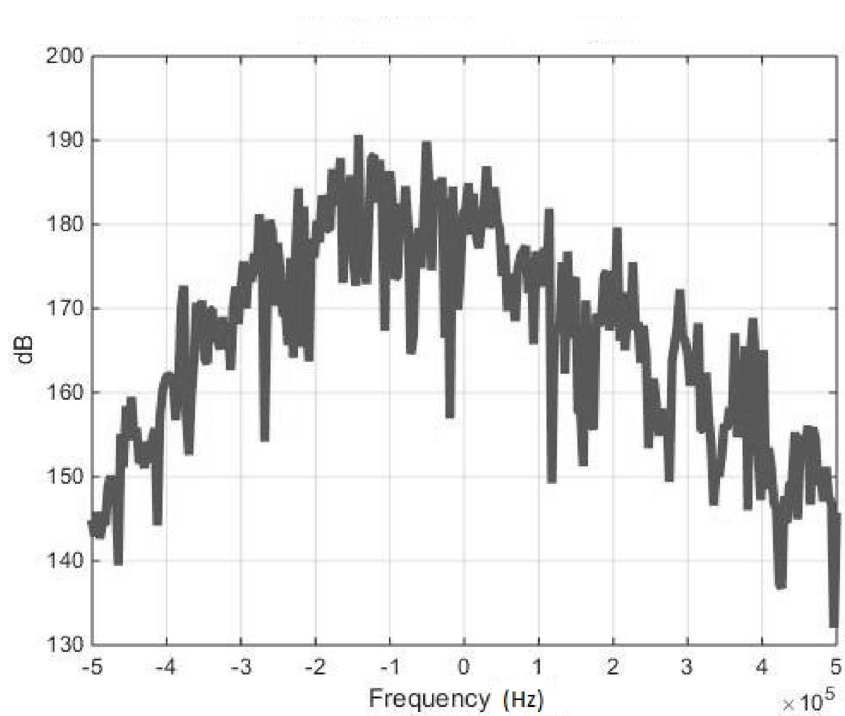

Figure 6.8: The Spectrum after the down-convertion stages (retrieving second trip).

spanning up to 40 dB, under 0.5 deg rms phase jitter. However, under similar conditions of phase noise (jitter), the frequency diversity scheme, proposed and developed in this thesis, can recover

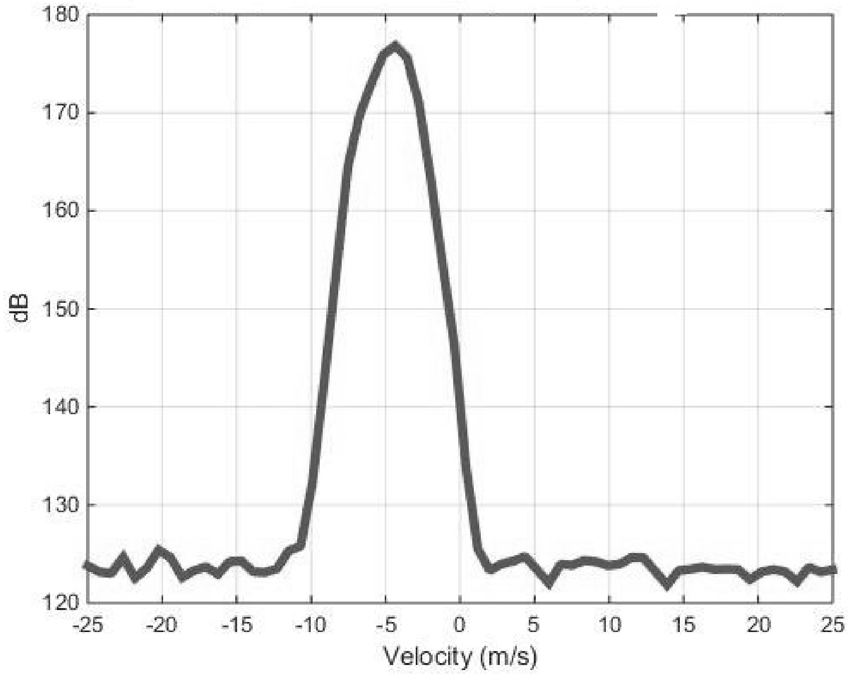

Figure 6.9: The velocity spectrum of the second trip, recovered after frequency switching between f_1 and f_2.

second trip for the power ratios spanning 60 dB, an improvement of about 20 dB over the Chu inter-pulse code. This is one of the achievements of this research and this has been substantiated here with time series simulation of weather echoes. With this simulation, the mean bias and standard deviation of second trip velocity as a function of power ratios for frequency diversity scheme is shown in Fig. 6.10 (a) and 6.10 (b). The simulation steps given before have been repeated for various power ratios of $|P_1/P_2|$, and these values have been given in the figures. It can be easily observed that the the standard deviation of the error increases significantly as the ratio exceeds 60 dB. These two figures imply that the proposed frequency diversity scheme can successfully reconstruct the second trip even if it is submerged in the stronger first trip power (by 60 dBs). This is a substantial improvement over any of the other inter-pulse schemes (random or SP Chu phase codes) published in literature.

We would also like to point out that the oscillator technology has been rapidly advancing and better phase jitter reference sources for radars are rapidly becoming available. For example, in

[61], the authors relate phase noise and coherency to clutter rejection ability of the radar and it is mentioned that WSR-88D radar is capable of 0.18 deg rms jitter and D3R radar is within 0.1 deg rms jitter. Thus it looks like the interpulse SZ codes would approach frequency diversity performance at lower phase noise conditions. As the systems become less noisy, the two techniques are comparable and frequency diversity will have major benefit at jitter greater than 0.2 deg rms. But we would like to highlight that the performance of frequency diversity can be directly linked to the stopband attenuation of the baseband digital filter in the downconverter and the frequencies f_1 and f_2. The farther these frequencies, the better the performance which can be expected thanks to an increase of stopband attenuation. Also, we have also observed from simulations that our proposed scheme gives 10 dB advantage at jitter conditions lesser than 0.1 deg rms if a better stop-band attenuation of 80dB's is utilized in down-converter.

But the biggest advantage is in the velocity recovery region at higher spectral widths. This is basically because of the fact that the SZ code replicates the spectrum of the second trip eight times (for SZ(8/64)) as compared to our scheme where sideband appears at π radians away from the main velocity spectrum, for both first and second trip recovery. Thus there is only one replica of the original spectrum at π radians apart instead of eight replicas of the second trip as in case of SZ codes. Now it is easy to observe that the recovery region of our scheme at higher spectral width for second trip velocity will be higher than SZ codes. To quantify, the recovery region (defined with respect to spectral width) will be at least twice of what is offered by SZ Codes in velocity retrievals. Hence our scheme will be able to tolerate twice as wider spectral width and correct estimate of velocity compared to SZ codes.

6.2.4 Velocity and Spectral Width Retrieval:

The proposed pulse-to-pulse alternate IF frequency scheme gives great benefit in terms of suppression/retrieval of the second trip echoes but it would require spectral processing to retrieve the velocity and spectral width information. This is because differing frequencies in alternate pulses make the data samples uncorrelated from one pulse to the other. However, the echoes are corre-

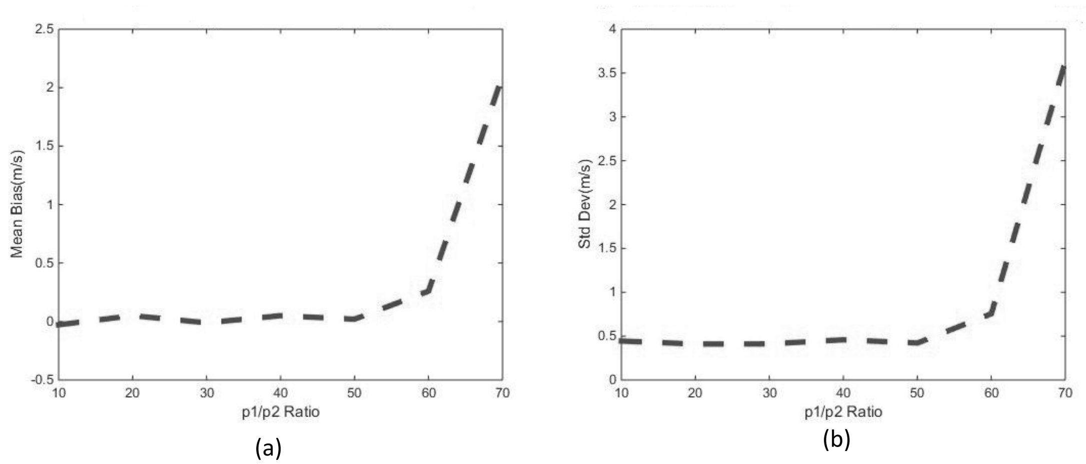

Figure 6.10: (a) The Mean Bias in the measurement of the second trip velocity, after frequency switching between f_1 and f_2, (b) The standard deviation in the measurement of the second trip velocity, after frequency switching between f_1 and f_2.

lated in alternate pulses. If we try to retrieve the velocity and spectral width information using the alternate pulse echoes, then the velocity range which could be resolved would become half. In this section, we describe a new process using which we can still recover the original range of velocities, with some constraints.

Basically, the uncorrelated data from these two frequencies manifests with a different amplitude and phase in adjacent pulse echoes. This phase term is in addition to the Doppler associated with the motion of the weather echoes. Thus, even for a stationary target, the amplitude and phase would keep cycling between two states. Because of this, there would be a fixed amplitude and phase modulation with a periodic repetition rate of the PRI, and the overall spectrum would have another sideband at $V_{1or2} - \pi$. This spectrum looks like as in Fig. 6.11. Moreover, you can observe that both the original and sideband looks identical and there is a necessity for some other means to figure out the original velocity. For correct spectral width retrieval, the sideband would need to be filtered, otherwise there is going to be an over-estimation of spectral width. We propose a mechanism here to correctly estimate velocity and spectral width with this type of fixed gain and phase state variation over multiple pulses. This would work under narrow spectral width constraint and we define a narrow spectral width echo to be around one-tenth of the unambiguous velocity

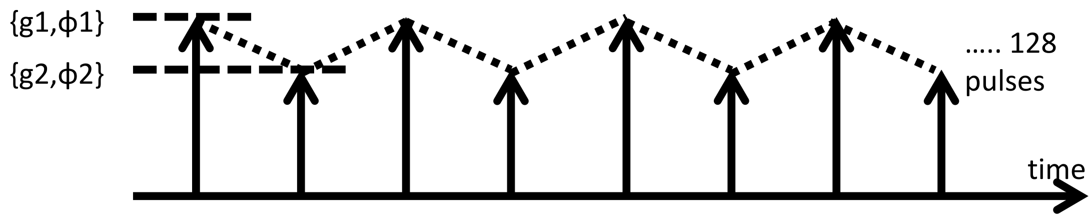

Figure 6.11: Fixed gain and phase modulation due to uncorrelated frequencies in alternate pulses.

range. For S-band, it would be approximately 5 m/s and for Ku band, this turns out to be close to 2 m/s.

The proposed mechanism is spectral based to retrieve velocity and spectral width in conjunction with running pulse-pair algorithm. Under the premise that phase and gain terms cycling through the two states periodically, the odd lags auto-correlation function will be zero (if we see the ensamble average of odd lags autocorrelation across all pulses) and at even lags this would be one with respect to one IF frequency, let's say f_1. Hence, we can write the auto-correlation function for f_1 at various lags as:

$$R_n^{com} = R_n[1 \;\; 0 \;\; 1 \;\; 0 \;\; ...] \tag{6.4}$$

where R_n is a single-lag autocorrelation function at f_1. R_n^{com} is the combined autocorrelation function from all lags. If we take the fourier transform of R_n^{com}, we get:

$$\begin{aligned} FT\{R_n^{com}\} &= FT\{R_n[1 \;\; 0 \;\; 1 \;\; 0 \;\; ...]\} \\ &= FT\{R_n\} * FT\{[1 \;\; 0 \;\; 1 \;\; 0 \;\; ...]\} \end{aligned} \tag{6.5}$$

where $*$ is the convolution operator. The term to the right of the operator is the fourier transform of a periodic pulse train which is also periodic and the impulses are spaced at $2pi/N$ ([62]) having a periodicity of $N = 2$. Thus the fourier transform of the overall auto-correlation function is the power spectral density of the weather echoes convolved with an impulse train spaced apart by pi radians. Now it becomes easy to understand that the spectrum of weather echoes with odd and even pulses modulated at different frequencies will have a sideband at $V_{1/2} - pi$ within the nyquist interval. Now let us look at how we can get rid of this additional sideband in the spectral domain.

Method

To start with, we process the upper-half of the spectrum at a particular radial and range, having $SNR > 10dB$, with a weather echo present. Assumption is that, either the original or side-band velocity would fall in this region of the spectrum. This is a fair assumption, because the original and sideband velocity spectrum is separated by π radians. We run pulse-pair autocorrelation algorithm for estimation of velocity on this half of the spectrum (making the other half zero), to get an initial crude estimate of velocity. As a next step, we use a notch filter with normalized notch width equal to 0.5, on the original spectrum with its passband centered around the estimate of velocity from pulse-pair algorithm. This would notch out the assumed sideband velocity component. We then run pulse-pair auto-correlation algorithm, once again, to get an accurate estimate of velocity and spectral width. An example velocity spectrum from D3R radar at a radial with two frequencies used in alternate pulses is shown in Fig. 6.12.

After the estimate of velocity has been obtained in one range cell of a radial, this can be propagated to other neighboring range cells below and above it, and to the one left and right of it, as an initial crude estimate of velocities for that range and radial. Assumption is that of spatial continuity of weather signals, which is good enough for most weather events. With the crude estimate, the notch filter passband would be centered around the crude velocity estimates in the adjoining range bins and their sideband velocities could be notched out. The estimate of velocities obtained from these range and radials are passed to the neighboring cells and thus we continue to get a better estimate of velocity and spectral width progressively in the same and adjoining radials. However, we need to verify our original assumption of retaining the upper-half of the spectrum in the very first range cell that we started from. With this assumption, the velocity profile was obtained at other ranges and radials. The verification process can be done by comparison with other radars or with different bands in the same radar. If we observe that the velocities are not matching for the same radials and elevations, then we need to subtract out v_{unb} from our computed

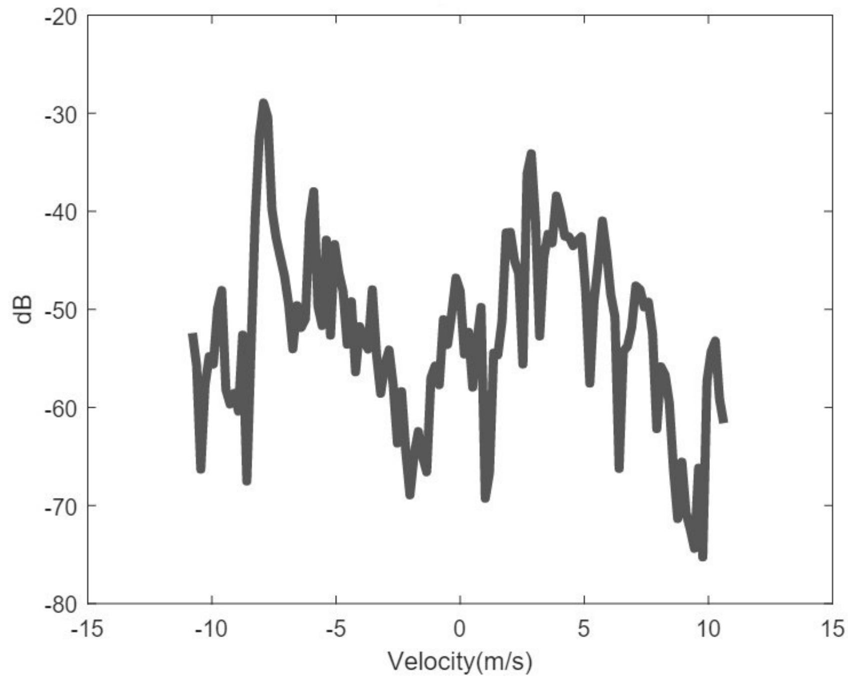

Figure 6.12: The Velocity Spectrum of one range cell at a certain radial (azimuth), from D3R weather radar, after frequency switching between f_1 and f_2 in adjacent pulses. The number of pulses considered is 128.

velocities. This would construct a velocity profile in a way if we had started with the other sideband in the first place. This whole method is summarized in Algorithm 2 for better clarity.

Algorithm 2 Retrieval of velocity and spectral width for frequency diversity scheme

1: **Initialization** Start with upper half of the spectrum for the range cell under consideration.
2: Run pulse-pair to get a crude estimation of velocity.
3: With this estimate, notch out the other sideband in the original spectrum.
4: Propagate this estimate of velocity to neighboring range cells.
5: Use notch filter to get rid of other sideband in neighbouring cells as well.
6: Likewise, reconstruct the velocity profile of the event by using velocity beliefs from neighboring cells.
7: Cross-compare with NEXRAD or interleaved normal scans.
8: If velocity looks to be of opposite sign, subtract pi radians from the whole reconstructed profile.

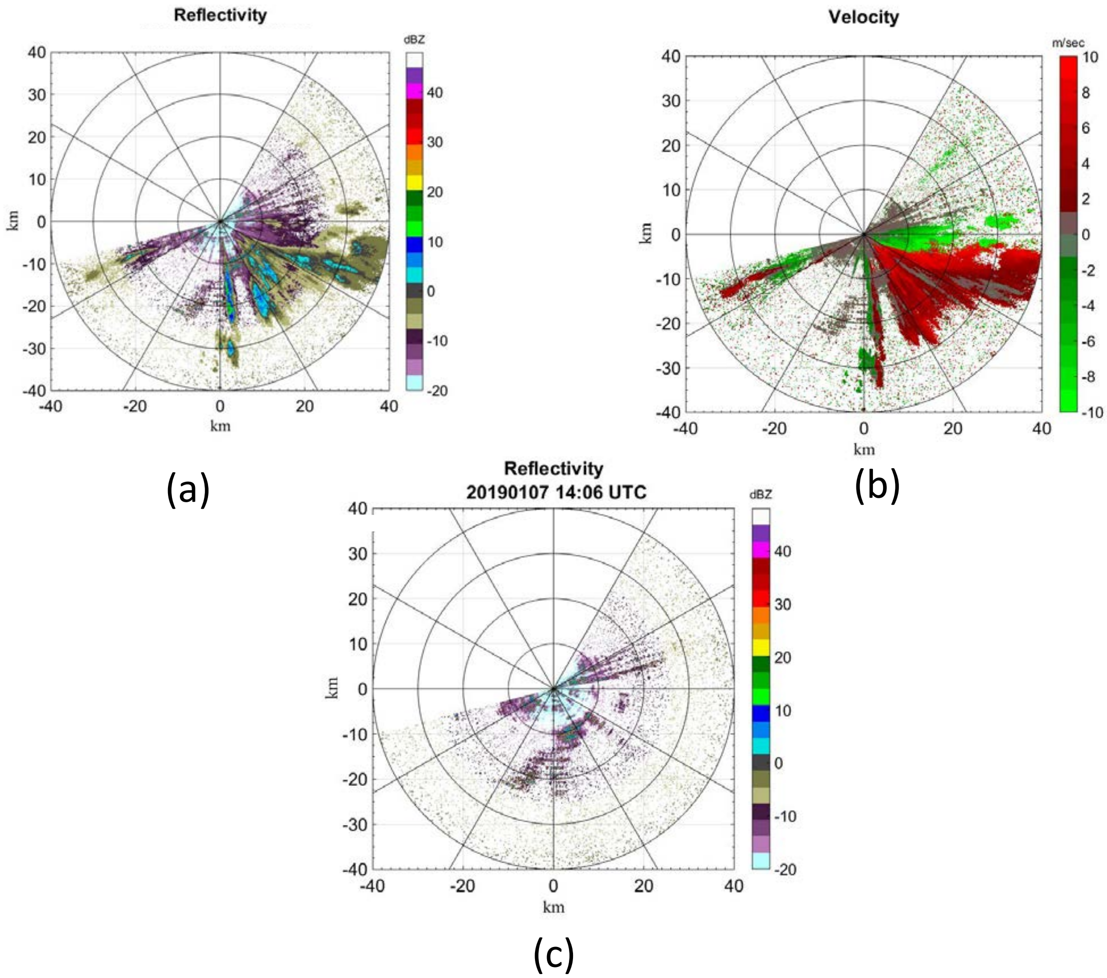

Figure 6.13: (a) and (b) depict the reflectivity and velocity with normal transmission. (c) depicts the reflectivity with frequency change pulse to pulse.

6.2.5 Limitations of the proposed scheme

It can be observed from the discussions in prior sections that due to the un-correlated data samples in adjacent pulses, velocity and spectral width need to be reconstructed with a new spectral based method. But it works under assumption of narrow spectral width. Such assumptions also hold for SZ code based retrievals, which under wider spectral width tend to behave more like random phase codes. We want to emphasize that although both schemes work under narrowband assumption but our proposed scheme is able to tolerate twice as wide spectral width for reconstruction of second trip velocity as compared to SZ codes.

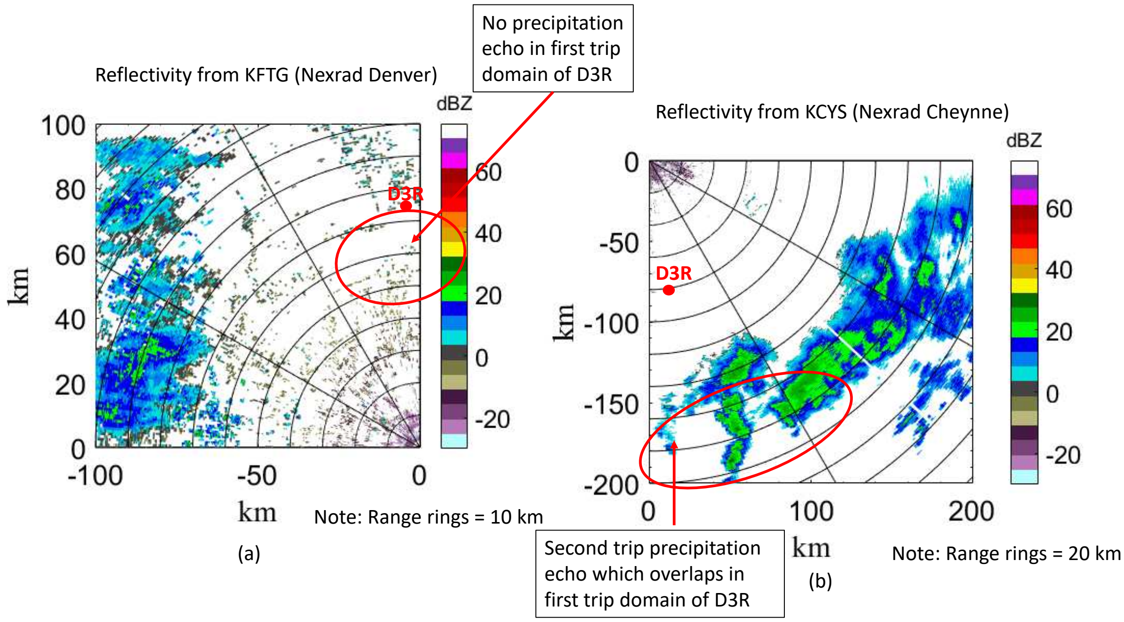

Figure 6.14: (a) depicts the cross-comparison of D3R first trip data with the nearby Denver Nexrad (2019/01/07 14:05:48 UTC), (b) is the validation of second trip echoes present in the Cheyyane Nexrad radar, which forms as second trip for D3R. In both cases, the location of D3R is also highlighted.

Another aspect which we have not dealt here is the multi-PRI situation like dual PRF techniques and staggered PRI modes. All of the illustrations carried out in this work have been tested with constant PRI mode. We feel that the extension for dual PRF based radar might be straightforward with IF frequency switching happening within the constant PRI blocks, where dual PRF system may have two blocks of different PRI's. However, we need to do further research on the staggered mode of operation, considering the way in which the velocities are unfolded in staggered system and embedding our framework of different IFs. Clutter suppression is also easier to deal with in constant PRI mode but might need additional processing for multi-PRI schemes. For constant PRI mode, the original clutter spectrum and its sideband would lie around the zero Doppler space and would be removed by the notch filter, in our proposed frequency diversity system.

Another area which requires attention and is a limitation is to find out a way to differentiate between original and sideband spectra in the retrieval of velocity and spectral width. This is currently accomplished by comparing few range cells velocities with other radar velocities. This step would require an offline processing step of comparison of few range cells in a PPI (plan position

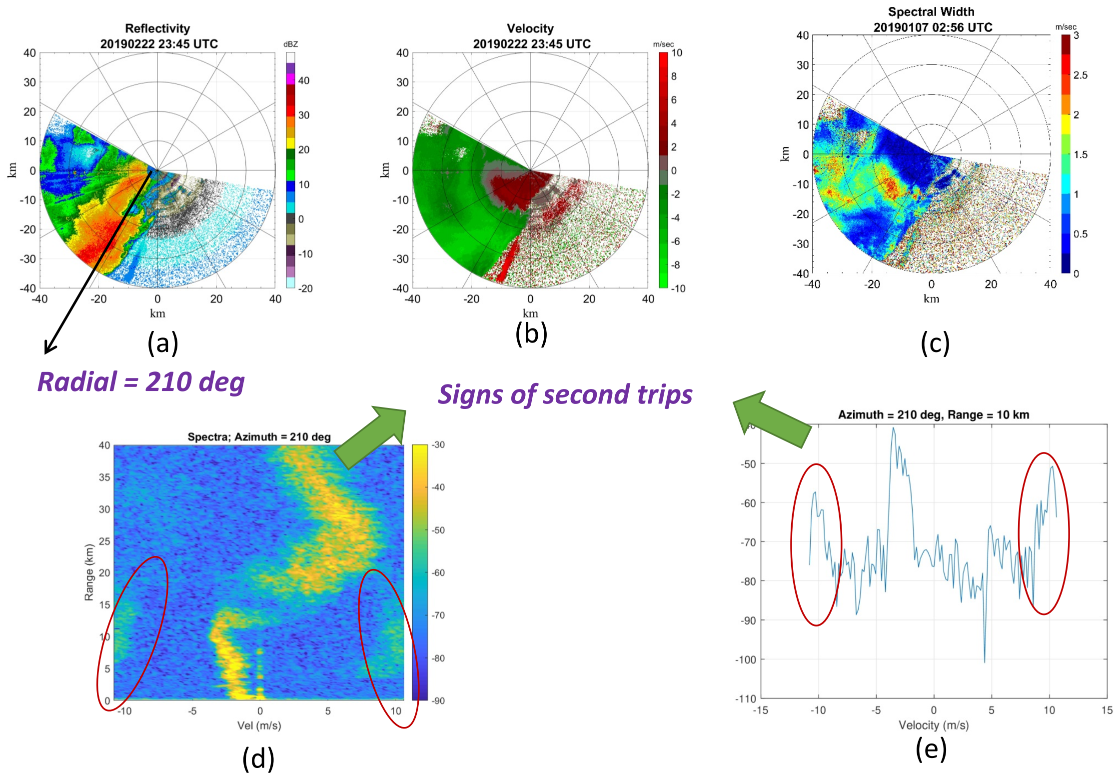

Figure 6.15: (a), (b) and (c) are the reflectivity, velocity and spectral width for an event observed by D3R with normal transmission. The velocity spectrum v/s range plot along a certain ray is shown in (d) with traces of second trip in the 5 to 15 km of range. Thus, bimodal Gaussian distribution is observed at a range bin at 10 km of range which is plotted in (e).

indicator) with other radar velocities, so that we know if we got latched to the wrong sideband. If we find that is the case, we need to subtract out π radians from all radials and range cells in that PPI. This can also be managed by interleaving normal operation mode in between (without frequency change pulse to pulse) for verifying the velocities in the same radar. For applications where more trips need to be recovered, we need more IF frequencies with adequate isolation (for the digital filters cutoff and roll-off requirements.)

6.3 Performance test on D3R

With D3R weather radar, we can make co-aligned Ku and Ka band echo observations for a precipitation event. It is a very useful ground validation tool for the Global Precipitation Measurement mission (GPM) satellite with dual-frequency radar. D3R uses a combination of short and

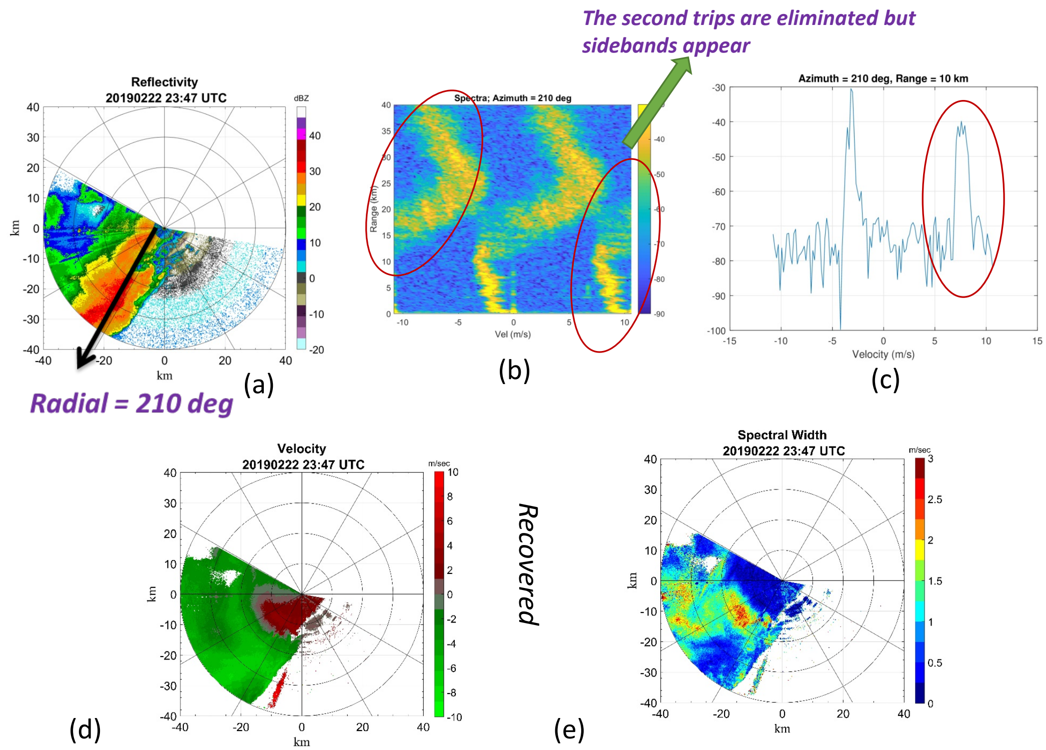

Figure 6.16: (a), (b) and (c) shows reflectivity, velocity spectrum v/s range plot (frequency diversity scheme) and velocity spectrum at a range of 10 km showing the sideband. (d) and (e) shows recovered velocity and spectral width after removal of the sideband with a narrow spectral width assumption.

medium pulses with pulse duration of $1\mu s$ and $20\mu s$ respectively. The short pulse is used to provide adequate sensitivity for the duration of medium pulse and mitigate blind range of the medium pulse. The radar has been in numerous field campaigns (see [63], [64] and [65]). Recently, the D3R radar was upgraded with a new version of digital receiver hardware and firmware which supports larger filter length and multiple phase coded waveforms, change of frequencies pulse to pulse and newer IF sub-systems ([51] and [50], [66] and [67]). With these new sub-systems, D3R was deployed for observing snow at the winter Olympics in Pheongchang region of South Korea, 2018 ([68], [69]). With a $500\mu s$ PRI, D3R's unambiguous range is 60 km. Beyond 60 km, it is the second trip range. In this section, we demonstrate the effectiveness of the pulse-to-pulse change of IF frequency on D3R Ku band and also, the retrieval of second trip after 60 km of range. The first case that is demonstrated in Fig. 6.13, has all of second trip echoes and no weather echoes in the first trip range. The normal transmission is using a chirp waveform for medium pulse centered

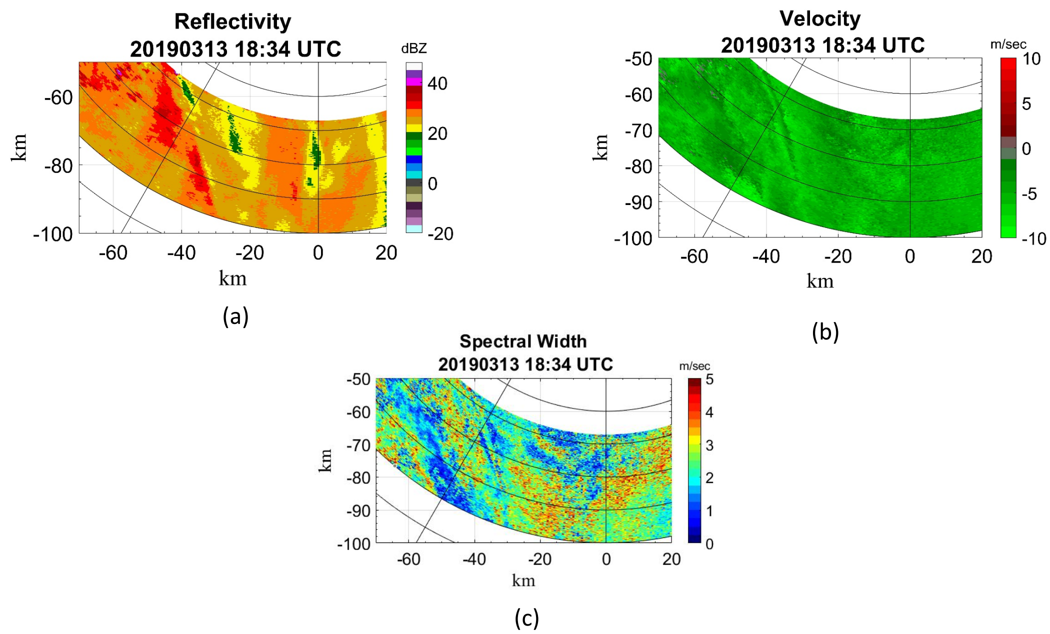

Figure 6.17: The recovered second trips are depicted on the PPI which is taken at an elevation of 1 degree.

at 65 MHz and a short pulse at 55 MHz. Whereas, for frequency diversity case, the frequencies used are 55 and 65 MHz for short and medium (odd numbered pulses). For the even numbered pulses, the frequencies used are 60 and 70 MHz for short and medium pulse respectively. The suppression of second trip can be observed in the south-east sector. All of the second trip has been removed and the remaining echoes are the clutter echoes. The D3R was installed at the CHILL radar site in Greeley, CO when this experiment for IF change pulse to pulse was accomplished. We did a cross-comparison with the nearby KFTG (Nexrad at Denver, CO) and KCYS (Nexrad at Cheyenne, CO) for confirming that there was indeed no first trip present for D3R unambiguous range, and all of the echoes do correspond to second trip for D3R. For the KTFG radar, we found the common volume for the scans of D3R operating at 2 deg elevation and the Nexrad at 0.48 deg. We can see this cross-comparison in Fig. 6.14 (a) and (b). In these plots, it can be easily verified that second trip was present for the D3R range (above 60 km) which got folded into the first trip range. The D3R was not collocated with these Nexrad radars used for verification but we used the location, geometry and scan information to find a common volume between the two radars (D3R and Nexrad) and these common volumes are depicted with red circles in these figures. Another case is depicted in Fig. 6.15. Initially, we show normal chirp transmission as reference with plots on reflectivity, velocity and spectral width. This case has first trip in the south-west sector, with second trip power overlaid. Fig. 6.15(e) shows the velocity profile along 210 deg radial and the second trip contamination can be clearly observed in 5 to 15 km of range. Also, Fig. 6.15(f) plots the velocity spectrum at a range of 10 km and at radial 210 deg, showing the second trip velocity. The frequency diversity case is shown in Fig. 6.16, which is taken a couple of minutes later, than the normal transmission. There were no second trip signatures from 5 to 15 km of range at the same radial but instead there is a replica of the original velocity spectrum as sideband, appearing at an offset of π radians from the original. The procedure to remove this undesired sideband is described in section 26.2.4. After we go through the steps listed in that section, we can reconstruct velocity and spectral width by filtering out sideband power. The velocity and spectral width recovered after this process is shown in Fig. 6.16(d) and (e) respectively.

Also, for this case, we recovered the second trip, which is shown after 60 km range in Fig. 6.17. For doing first trip retrieval, we programmed the sequence, f_1, f_2, in a frame of two pulse echoes, while for second trip recovery, the sequence used would be f_2, f_1.

6.4 Effect of Frequency Diversity scheme on other dual polarization moments

It is to be noted here that the proposed frequency diversity scheme would reduce the bias induced by second trip on single polarization and dual polarization moment estimates through its suppression below noise floor. But practically it is observed that the accuracy of dual-polarization moments also depend upon the co-polar correlation coefficient between the horizontal and vertical polarization echoes. [5] describe in detail, the effect of co-polar correlation coefficient on these moments under alternate and hybrid modes of operation. In this section, we try to analyze the effect of pulse to pulse frequency diversity on the estimation of co-polar correlation coefficient. In this analysis, we would also try to see the effect of non-ideal conditions and mismatched channels. Assume the first trip, for all pulses, be denoted by H_1 and the second trip by H_2 and the baseband filter matrix by $\mathbf{F}_{bb}$, then the equivalent signal model for H-pol and V-pol, for the first trip retrieval, can be written as:

$$\begin{aligned}\mathbf{H}^1 &= \mathbf{H}_1 + \mathbf{F}_{bbh}.\mathbf{H}_2 \\ \mathbf{V}^1 &= \mathbf{V}_1 + \mathbf{F}_{bbv}.\mathbf{V}_2\end{aligned} \tag{6.6}$$

The autocorrelation function for the first trip, for the hybrid mode of operation, can be written as:

$$\begin{aligned}R^1_{vh}(0) &= \frac{1}{N}Tr\{\mathbf{V}^1\mathbf{H}^{1H}\} \\ &= \frac{1}{N}Tr\{(\mathbf{V}_1 + \mathbf{F}_{bbv}.\mathbf{V}_2)(\mathbf{H}_1 + \mathbf{F}_{bbh}.\mathbf{H}_2)^H\} \\ &= \frac{1}{N}Tr\{\mathbf{V}_1\mathbf{H}_1^H + \mathbf{V}_2\mathbf{H}_2^H\mathbf{F}_{bbh}^H\mathbf{F}_{bbv}\}\end{aligned} \tag{6.7}$$

If the characteristics of both H and V pol filters are the same, then $\mathbf{F}_{bbh} = \mathbf{F}_{bbv} = \mathbf{F}$ and the above equation could be simplified to:

$$R^1_{vh}(0) = \frac{1}{N}Tr\{\mathbf{V}_1\mathbf{H}_1^H\} + Tr\{\mathbf{V}_2\mathbf{H}_2^H\mathbf{F}^H\mathbf{F}\} \tag{6.8}$$

Similarly, for the second trip, we can model it as:

$$\begin{aligned}\mathbf{H}^2 &= \mathbf{F}_{bbh}.\mathbf{H}_1 + \mathbf{H}_2 \\ \mathbf{V}^2 &= \mathbf{F}_{bbv}.\mathbf{V}_1 + \mathbf{V}_2\end{aligned} \tag{6.9}$$

with the auto-correlation function as:

$$R^2_{vh}(0) = \frac{1}{N}Tr\{\mathbf{V}_2\mathbf{H}_2^H\} + Tr\{\mathbf{V}_1\mathbf{H}_1^H\mathbf{F}^H\mathbf{F}\} \tag{6.10}$$

The corresponding correlation coefficients could be written as (see [**?**]):

$$\begin{aligned}
\rho_{vh}^{1}(0) &= \frac{R_{vh}^{1}(0)}{\sqrt{P_{co}^{1h}P_{co}^{1v}}} \\
\rho_{vh}^{2}(0) &= \frac{R_{vh}^{2}(0)}{\sqrt{P_{co}^{2h}P_{co}^{2v}}}
\end{aligned} \tag{6.11}$$

where $P_{co}^{1,2,h,v}$ is the co-polar power for first or second trip echoes, and for horizontal or vertical polarized echoes respectively. The degree of dissimilarity between the auto-correlations of the horizontal or vertical polarized echoes will be a factor which would impact the $\rho_{vh}(0)$ for the first and second trip echoes. This dissimilarity could arise due to slight difference in filter characteristics, on the receive (cumulative effects of anti-aliasing or baseband cascade integrate comb (CIC)/finite impulse response (FIR) based filtering). Now, we would try to analyze the effect of this scheme, on differential reflectivity (Z_{dr}), when first trip is being retrieved:

$$\begin{aligned}
Z_{dr}^{1} = \frac{P_{co}^{1h}}{P_{co}^{1v}} &= \frac{R_{vv}^{1}(0)}{R_{hh}^{1}(0)} \\
&= \frac{Tr\{(\mathbf{V}_1 + \mathbf{F}_{bbv}\mathbf{V}_2)(\mathbf{V}_1 + \mathbf{F}_{bbv}\mathbf{V}_2)^H\}}{Tr\{(\mathbf{H}_1 + \mathbf{F}_{bbh}\mathbf{H}_2)(\mathbf{H}_1 + \mathbf{F}_{bbh}\mathbf{H}_2)^H\}} \\
&= \frac{Tr\{\mathbf{V}_1\mathbf{V}_1^H + \mathbf{V}_1(\mathbf{F}\mathbf{V}_2)^H + (\mathbf{F}\mathbf{V}_2)\mathbf{V}_1^H + \mathbf{F}\mathbf{V}_2(\mathbf{F}\mathbf{V}_2)^H\}}{Tr\{\mathbf{H}_1\mathbf{H}_1^H + \mathbf{H}_1(\mathbf{F}\mathbf{H}_2)^H + (\mathbf{F}\mathbf{H}_2)\mathbf{H}_1^H + \mathbf{F}\mathbf{H}_2(\mathbf{F}\mathbf{H}_2)^H\}}
\end{aligned} \tag{6.12}$$

assuming $\mathbf{F}_{bbh} = \mathbf{F}_{bbv} = \mathbf{F}$. It can be easily observed from the equation above, that major contribution towards bias of Z_{dr}, is through the middle two terms in numerator and denominator (getting multiplied by the first trip voltage). The second trip voltage, however, is always preceded by the filter matrix and is going to be low. Additionally, the degree of dissimilarity between the filter response on the horizontal or vertical polarized echoes, is also going to contribute towards bias in Z_{dr}.

6.5 Conclusion

We have proposed a scheme using inter-pulse frequency diversity techniques for weather radar systems and utilized the orthogonality between two frequencies in IF band to reject the second trip echoes. This technique shows improvement in performance of second trip suppression and retrieval under higher phase noise condition as compared with Chu phase codes (SZ Codes). Extensive time-series simulations were carried out to ascertain the performance of this technique. A comparison with Chu phase code based inter-pulse system was presented and shows promising results with recovery of the weather echoes under wider dynamic range of overlaid power contamination and wider spectral width.

Chapter 7

Summary

This thesis has achieved three main goals. Firstly, the utility of intra-pulse polyphase coding techniques for weather radar systems was demonstrated and the recent research in developing codes with good correlation properties was utilized for weather radar application. This technique was applied for second trip suppression. Simulations were carried out to ascertain the performance of these new polyphase codes. The real-time implementation was carried out in NASA D3R weather radar, to see the suppression abilities of the developed code-filter pairs. During this research, it was realized that perfect orthogonality was impossible to be realized and instead we aim for the best possible pseudo-orthogonality. Additionally, the pair of codes used in this work, does not have suppression for odd trip echoes. However, using the same framework, more code-filter pairs can be synthesized, and third, fourth and so on pulses can be coded to achieve odd trip suppression as well.

Secondly, we propose a scheme using inter-pulse frequency diversity techniques for weather radar systems and utilized the orthogonality between two frequencies in IF domain to reject out the second trip echoes. This scheme shows improvement in performance of second trip suppression and retrieval under phase noise condition as compared with Chu phase codes (SZ Codes). Extensive time-series simulations were carried out to ascertain the performance of this new scheme. It shows promising results with recovery of the weather echoes under wider dynamic range of overlaid power contamination. However, it should be emphasized that due to the un-correlated data samples in adjacent pulses, velocity and spectral width needs to be reconstructed with a new spectral based method which is described.

Thirdly, a MIMO configuration from a phased array radar is developed which gains tremendously from the orthogonality feature achieved through intra pulse polyphase coding technique and inter-pulse frequency diversity coding. This MIMO configuration is beneficial as it improves the spatial resolution of the array without physical addition of more elements through the creation of virtual array. There we simulate the antenna geometry and antenna patterns to gain insight into the MIMO capabilities of a phased array antenna. Simulations of MIMO systems for feature detection in weather scenarios was carried out. With this we could demonstrate the importance of enhanced spatial resolution in these feature detection process through the MIMO techniques. It becomes clear from the antenna pattern simulations that this configuration forms a virtual array which is one and a half times bigger in dimension as compared to the physical array but a major requirement for this to happen is through orthogonal transmission through each quadrant of the array. This benefit is however available at a potential loss in SNR due to quadrant wise beamforming.

Finally, the upgrade of NASA D3R weather radar was also discussed, which made its architecture more flexible so that these enhancements could be incorporated. The D3R radar is based on parabolic reflector antenna, so the orthogonal features of the developed techniques were demonstrated for second trip suppression and retrieval capability for mitigating range and velocity ambiguities. Later, after the upgrade process, the recent deployment to S.Korea for winter Olympics 2018, was also presented.

Bibliography

[1] Vega, M., V. Chandrasekar, J. Carswell, R. M. Beauchamp, M. R. Schwaller, and C. M. Nguyen, “Salient features of the dual-frequency, dual-polarized, Doppler radar for remote sensing of precipitation”, Radio Sci., vol. 49, pp. 1087-1105, 2014.

[2] Tyynelä, J. and Chandrasekar, V., “Characterizing falling snow using multi-frequency dual-polarization measurements”, Journal of Geophysical Research: Atmospheres, vol. 119, pp. 8268-8283, 2014.

[3] Bechini, R. and V. Chandrasekar, “A Semisupervised Robust Hydrometeor Classification Method for Dual-Polarization Radar Applications”, J. Atmos. Oceanic Technol., vol. 32, pp. 22–47, 2015.

[4] Bharadwaj, N. and V. Chandrasekar, “Wideband Waveform Design Principles for Solid-State Weather Radars”, J. Atmos. Oceanic Technol.,vol. 29, no. 1, pp. 14-31, 2012.

[5] Bringi, V., and V. Chandrasekar, “Polarimetric Doppler Weather Radar: Principles and Applications”, Cambridge University Press, 2001.

[6] D. Chu, “Polyphase codes with good periodic correlation properties (Corresp.)”, in IEEE Transactions on Information Theory, vol. 18, no. 4, pp. 531-532, July 1972.

[7] Doviak, J., and Zrnic. S., “Doppler Radar and Weather Observations”, Academic Press.

[8] Development Project and Forecast Demonstration, “ICEPOP2018 Science Plan,” 2018.

[9] S. D. Howard, A. R. Calderbank and W. Moran, “A Simple Signal Processing Architecture for Instantaneous Radar Polarimetry”, in IEEE Transactions on Information Theory, vol. 53, no. 4, pp. 1282-1289, April 2007.

[10] S. Mertens, “Exhaustive search for low-autocorrelation binary sequences”, J. Phys. A, vol. 29, pp. 473-481, 1996.

[11] Torres, S.M. and D.A. Warde, “Staggered-PRT Sequences for Doppler Weather Radars. Part I: Spectral Analysis Using the Autocorrelation Spectral Density”, J. Atmos. Oceanic Technol., vol. 34, pp. 51-63, 2017.

[12] Cho, J.Y. and E.S. Chornoboy, “Multi-PRI Signal Processing for the Terminal Doppler Weather Radar. Part I: Clutter Filtering”, J. Atmos. Oceanic Technol., vol. 22, pp. 575-582, 2005.

[13] Frush, C., R.J. Doviak, M. Sachidananda, and D.S. Zrnic, “Application of the SZ Phase Code to Mitigate Range-Velocity Ambiguities in Weather Radars”, J. Atmos. Oceanic Technol., vol. 19, pp. 413-430, 2002.

[14] W. Roberts, J. Li, P. Stoica, T. Yardibi and F. A. Sadjadi, "MIMO radar angle-range-Doppler imaging," 2009 IEEE Radar Conference, Pasadena, CA, 2009, pp. 1-6.

[15] Huaijun Wang and Yi Su, "Narrowband MIMO radar imaging with two orthogonal linear T/R arrays," 2008 9th International Conference on Signal Processing, Beijing, 2008, pp. 2513-2516.

[16] C. Ma, T. S. Yeo, C. S. Tan and Z. Liu, "Three-Dimensional Imaging of Targets Using Colocated MIMO Radar," in IEEE Transactions on Geoscience and Remote Sensing, vol. 49, no. 8, pp. 3009-3021, Aug. 2011.

[17] P. F. Sammartino, C. J. Baker and H. D. Griffiths, "Frequency Diverse MIMO Techniques for Radar," in IEEE Transactions on Aerospace and Electronic Systems, vol. 49, no. 1, pp. 201-222, Jan. 2013.

[18] Li, J., Stoica, P., and Zheng, X., "Signal synthesis and receiver design for MIMO radar imaging", IEEE Transactions on Signal Processing, vol. 56, no. 8, pp. 3959–3968, 2008.

[19] Bliss, D. W. and Forsythe, K. W., "MIMO radar and imaging: Degrees of freedom and resolution", In Conference Record of the Thirty-Seventh Asilomar Conference on Signals, Systems, and Computers, Pacific Grove, CA, pp. 54–59, 2003.

[20] R. Feger, C. Wagner, S. Schuster, S. Scheiblhofer, H. Jager and A. Stelzer, "A 77-GHz FMCW MIMO Radar Based on an SiGe Single-Chip Transceiver," in IEEE Transactions on Microwave Theory and Techniques, vol. 57, no. 5, pp. 1020-1035, May 2009.

[21] F. C. Robey, S. Coutts, D. Weikle, J. C. McHarg and K. Cuomo, "MIMO radar theory and experimental results," Conference Record of the Thirty-Eighth Asilomar Conference on Signals, Systems and Computers, 2004., Pacific Grove, CA, USA, 2004, pp. 300-304 Vol.1.

[22] G. San Antonio, D. R. Fuhrmann and F. C. Robey, "MIMO Radar Ambiguity Functions," in IEEE Journal of Selected Topics in Signal Processing, vol. 1, no. 1, pp. 167-177, June 2007.

[23] Li, Jianfeng, Xiaofei Zhang and Weiyang Chen. “Root-MUSIC Based Angle Estimation for MIMO Radar with Unknown Mutual Coupling”, 2014.

[24] Jingping Liu, Song Liu, Huichang Zhao and Kairui Huo, "Improvement to the traditional MUSIC algorithm for MIMO radar angle estimation," 2015 IEEE Radar Conference (RadarCon), Arlington, VA, 2015, pp. 0511-0514.

[25] Wang Nan, Wang Wenguang, Zhang Fan, Yuan Yunneng, "The PARAFAC-MUSIC algorithm for DOA estimation with doppler frequency in a MIMO radar system.", International Journal of Antennas and Propagation. 2014. 1-5. 10.1155/2014/684591, 2014

[26] Hai Deng, “Polyphase code design for Orthogonal Netted Radar systems”, in IEEE Transactions on Signal Processing, vol. 52, no. 11, pp. 3126-3135, Nov. 2004.

[27] J. Song, P. Babu and D. P. Palomar, “Sequence Set Design With Good Correlation Properties Via Majorization-Minimization”, in IEEE Transactions on Signal Processing, vol. 64, no. 11, pp. 2866-2879, June1, 2016.

[28] H. He, P. Stoica and J. Li, “Designing Unimodular Sequence Sets With Good Correlations Including an Application to MIMO Radar”, in IEEE Transactions on Signal Processing, vol. 57, no. 11, pp. 4391-4405, Nov. 2009.

[29] Bharadwaj, N. and V. Chandrasekar, “Phase Coding for Range Ambiguity Mitigation in Dual-Polarized Doppler Weather Radars”, J. Atmos. Oceanic Technol., vol. 24, no. 8, pp. 1351-1363, 2007.

[30] Sachidananda, M. and D.S. Zrnic, “Systematic Phase Codes for Resolving Range Overlaid Signals in a Doppler Weather Radar”, J. Atmos. Oceanic Technol., vol. 16, no. 10, pp. 1351-1363, 1999.

[31] D. Chu, “Polyphase codes with good periodic correlation properties (Corresp.)”, in IEEE Transactions on Information Theory, vol. 18, no. 4, pp. 531-532, July 1972.

[32] Chandrasekar, V. and N. Bharadwaj, “Orthogonal Channel Coding for Simultaneous Co- and Cross-Polarization Measurements”, J. Atmos. Oceanic Technol., vol. 26, no. 1, pp. 45-56, 2009.

[33] S. D. Howard, A. R. Calderbank and W. Moran, “A Simple Signal Processing Architecture for Instantaneous Radar Polarimetry”, in IEEE Transactions on Information Theory, vol. 53, no. 4, pp. 1282-1289, April 2007.

[34] K. R. Griep, J. A. Ritcey and J. J. Burlingame, “Poly-phase codes and optimal filters for multiple user ranging”, in IEEE Transactions on Aerospace and Electronic Systems, vol. 31, no. 2, pp. 752-767, April 1995.

[35] S. Mertens, “Exhaustive search for low-autocorrelation binary sequences”, J. Phys. A, vol. 29, pp. 473-481, 1996.

[36] D. Sarwate, “Bounds on crosscorrelation and autocorrelation of sequences (Corresp.)”, in IEEE Transactions on Information Theory, vol. 25, no. 6, pp. 720-724, November 1979.

[37] L. Welch, “Lower bounds on the maximum cross correlation of signals (Corresp.)”, in IEEE Transactions on Information Theory, vol. 20, no. 3, pp. 397-399, May 1974.

[38] J. Li, P. Stoica and X. Zheng, “Signal Synthesis and Receiver Design for MIMO Radar Imaging”, in IEEE Transactions on Signal Processing, vol. 56, no. 8, pp. 3959-3968, Aug. 2008.

[39] Y. Liu, Y. Li and X. Wang, “Instantaneous measurement for radar target polarization scattering matrix”, in Journal of Systems Engineering and Electronics, vol. 21, no. 6, pp. 968-974, Dec. 2010.

[40] Hui Liu and Guanghan Xu, “A subspace method for signature waveform estimation in synchronous CDMA systems”, Conference Record of The Twenty-Ninth Asilomar Conference on Signals, Systems and Computers, Pacific Grove, CA, USA, pp. 157-161 vol.1, 1995.

[41] J. Tang, N. Zhang, Z. Ma and B. Tang, “Construction of Doppler Resilient Complete Complementary Code in MIMO Radar”, in IEEE Transactions on Signal Processing, vol. 62, no. 18, pp. 4704-4712, Sept.15, 2014.

[42] A. Pezeshki, A. R. Calderbank, W. Moran and S. D. Howard, “Doppler Resilient Golay Complementary Waveforms”, in IEEE Transactions on Information Theory, vol. 54, no. 9, pp. 4254-4266, Sept. 2008.

[43] H. D. Nguyen and G. E. Coxson, “Doppler tolerance, complementary code sets, and generalised Thue–Morse sequences”, in IET Radar, Sonar and Navigation, vol. 10, no. 9, pp. 1603-1610, 2016.

[44] X. Yang, Y. Mo, D. Li and M. Bian, “New Complete Complementary Codes and Their Analysis”, IEEE GLOBECOM 2007 - IEEE Global Telecommunications Conference, Washington, DC, pp. 3899-3904, 2007.

[45] C. Han, N. Suehiro and T. Hashimoto, “A Systematic Framework for the Construction of Optimal Complete Complementary Codes”, in IEEE Transactions on Information Theory, vol. 57, no. 9, pp. 6033-6042, Sept. 2011.

[46] Choudhury, S. and Bharadwaj, N., “Computer Simulation of Weather Radar Signals”, Dept. of Electrical and Computer Engg., Colorado State University, 2001.

[47] J. M. Baden, M. S. Davis and L. Schmieder, “Efficient energy gradient calculations for binary and polyphase sequences”, 2015 IEEE Radar Conference (RadarCon), Arlington, VA, pp. 0304-0309, 2015.

[48] U. Tan, O. Rabaste, C. Adnet, F. Arlery and J. Ovarlez, “Optimization methods for solving the low autocorrelation sidelobes problem”, 17th International Radar Symposium (IRS), Krakow, pp. 1-5, 2016.

[49] F. Glover, “A template for scatter search and path relinking”, Lecture Notes on Computer Science, 1363, pp. 13-54, 1997.

[50] M. Kumar, S. S. Joshil, V. Chandrasekar, R. M. Beauchamp, M. Vega, and J. W. Zebley, “Performance trade-offs and upgrade of NASA D3R weather radar”, IEEE International Geoscience and Remote Sensing Symposium (IGARSS), pp. 5260–5263, July 2017.

[51] M. Kumar, S. Joshil, M. Vega, V. Chandrasekar, and J. W. Zebley, “NASA D3R: 2.0, Enhanced radar with new data and control features”, IEEE International Geoscience and Remote Sensing Symposium, pp. 7978-7981, July 2018.

[52] Rafael Marti, Manuel Laguna, Fred Glover, “Principles of scatter search”, European Journal of Operational Research, Volume 169, Issue 2, Pages 359-372, 2006.

[53] Torres, S. M., Y. F. Dubel, and D. Zrnic, “Design, implementation, and demonstration of a staggered PRT algorithm for the WSR-88D”, J. Atmos. Oceanic Technol., vol. 21, no. 9, pp. 1389-1399, 2004.

[54] R. Fletcher, “A new approach to variable metric algorithms”, The Computer Journal, Vol. 13, Issue 3, pp. 317–322, 1970.

[55] H. W. Kuhn and A. W. Tucker, “Non-linear Programming”, Proc. Second Berkeley Symp. on Math. Statist. and Prob., pp. 481–492, 1951.

[56] M. Kumar and V. Chandrasekar, “Intrapulse Polyphase Coding System for Second Trip Suppression in a Weather Radar”, in IEEE Transactions on Geoscience and Remote Sensing, vol. 58, no. 6, pp. 3841-3853, June 2020.

[57] Karhunen Pentti, Sebastian Torres and Alan Passarelli, “Method for extension of unambiguous range and velocity of a weather radar”, US Patent number 7605744, Oct 2009.

[58] Li Lihua, Mclinden Matthew, Coon Michael, Heymsfield Gerald and Subbaraman Vijay, “Frequency diversity pulse pair determination for mitigation of radar range-doppler ambiguity”, US Patent number 10317521, June 2019.

[59] Gaspare Galati, Gabriele Pavan, “Computer simulation of weather radar signals”, Simulation Practice and Theory, vol. 3, Issue 1, pp. 17-44, 1995.

[60] M. J. Underhill, “Fundamentals of oscillator performance”, in Electronics and Communication Engineering Journal, vol. 4, no. 4, pp. 185-193, Aug. 1992.

[61] J. J. Stagliano, J. Helvin, J. L. Alford, and D. Nelson, “Phase noise, coherency, and clutter suppression”, AMS Radar Conference, 2005.

[62] A. V. Oppenheim, and R. W. Schafer, “Discrete-Time Signal Processing”, 3rd ed., Prentice Hall Press, Upper Saddle River, NJ, USA, 2009.

[63] V. Chandrasekar et al., “Meteorological observations and system performance from the nasa D3R’s first 5 years”, IEEE International Geoscience and Remote Sensing Symposium (IGARSS), Fort Worth, TX, 2017, pp. 2734-2736, 2017.

[64] V. Chandrasekar et al., “Observations and performance of the NASA dual-frequency dual-polarization Doppler radar (D3R) from five years of operation”, 2017 XXXIInd General Assembly and Scientific Symposium of the International Union of Radio Science (URSI GASS), Montreal, QC, pp. 1-2, 2017.

[65] V. Chandrasekar et al., “Deployment and performance of the NASA D3R during the GPM OLYMPEx field campaign”, 2016 IEEE International Geoscience and Remote Sensing Symposium (IGARSS), Beijing, pp. 2142-2145,2016.

[66] M. Kumar, and V. Chandrasekar, “Use of adaptive filtering techniques and deconvolution to obtain low sidelobe range samples in nasa d3r radar”, 38th Conference on Radar Meteorology, Chicago, 2017.

[67] M. Kumar, Dileep, K. Sreenivasulu, D. Seshagiri, D. Srinivas, and S. Narasimhan, “Receive signal path design for active phased array radars”, 2019.

[68] V. Chandrasekar, S. S. Joshil, M. Kumar, M. A. Vega, D. Wolff and W. Petersen, “Snowfall Observations During the Winter Olympics of 2018 Campaign Using the D3r Radar”, IGARSS 2019 - 2019 IEEE International Geoscience and Remote Sensing Symposium, Yokohama, Japan, pp. 4561-4564, 2019.

[69] V. Chandrasekar, M. A. Vega, S. Joshil, M. Kumar, D. Wolff and W. Petersen, “Deployment and Performance of the Nasa D3R During the Ice-Pop 2018 Field Campaign in South Korea”, IGARSS 2018 - 2018 IEEE International Geoscience and Remote Sensing Symposium, Valencia, pp. 8349-8351, 2018.